Università degli Studi di Padova

DIPARTIMENTO DI INGEGNERIA INDUSTRIALE
Corso di Laurea Magistrale in Ingegneria Chimica e dei Processi Industriali

TESI DI LAUREA MAGISTRALE IN
INGEGNERIA CHIMICA E DEI PROCESSI INDUSTRIALI

Investigation of isothermal unsteady-state CO_2 Capture and Reduction over K-promoted supported Cu-catalysts

Laureando:
Stefano Minorello
Matricola 1207219

Relatore:
Prof. Paolo Canu

Supervisore Istituto Ospitante:
Prof. Atsushi Urakawa

Anno Accademico 2019/2020

“Today is only one day in all the days that will ever be.
But what will happen in all the other days that ever come
can depend on what you do today.”
- *E. Hemingway*

Abstract

In order to substitute the current fossil fuel-based chemistry, research is actively focused on the development of sustainable technologies with alternative sources. Among the different strategies, carbon dioxide Capture and Utilisation techniques are gaining industrial interest. The motivation relies in the attractive possibility of reducing CO_2 emissions by utilising it as a source for added-value chemicals.

In this thesis, the novel CO_2 Capture and Reduction approach has been investigated. In this catalytic process, CO_2 from diluted streams (i.e. post-combustion flue gases) can be efficiently captured by a solid catalyst. By switching to a H_2 stream, the captured CO_2 is selectively converted to CO, in a typical unsteady-state isothermal operation. This particular work focuses on the catalytic behaviour of supported copper catalysts promoted with potassium.

The catalytic activity of a series of supported copper catalysts synthesised through the incipient wetness impregnation method has been evaluated. Operando FTIR allowed for the detection of the outlet gas composition with high time resolution. A combination of characterisation techniques (XRD, BET, TPR, SEM, TEM, ex-situ and in-situ Raman) has been employed to individuate the active phase and the mechanism of CO_2 capture and reduction processes. An optimum loading of K and Cu exists, with the former species controlling the CO_2 capture properties and the latter the formation of active sites for reduction with H_2. Insights in the capture mechanism have been reported, with a particular interest in the formation of the active phase for CO_2 capture. CO has been found to participate in the adsorption process, while the first operation cycle contributes to the generation of the CCR active phase, which is strongly dependent on the presence of potassium and copper.

By comparing similar catalysts supported on different metal oxides, the dispersion of the active species has been observed to be beneficial for catalytic activity. Indications about the enhancement of active species dispersion through the modification of the synthesis method have also been reported.

From the optimisation of process parameters as temperature, flow rates and synthesis conditions almost 100 s of CO_x full capture has been reached. During an equivalent time interval, the 65% of the adsorbed CO_2 is converted to CO, highlighting the great potential of the CCR process as a strategy for CO_2 utilisation.

Riassunto

Negli ultimi decenni, per sostituire l'utilizzo di combustibili fossili a livello industriale, la ricerca si è focalizzata sullo sviluppo di tecnologie sostenibili basate su fonti alternative. Tra le diverse strategie, le tecniche di Cattura e Utilizzazione di anidride carbonica hanno attirato grande interesse. La principale motivazione risiede nella possibilità di ridurre le emissioni di CO_2 attraverso il suo impiego come elemento di partenza per la produzione di prodotti a valore aggiunto.

Nella tesi viene studiato un nuovo processo, denominato CO_2 Capture and Reduction. In questo processo catalitico, la CO_2 contenuta in correnti diluite, come ad esempio i gas di scarico da post-combustione, può essere catturata grazie ad un catalizzatore solido. Successivamente, esponendo il catalizzatore ad un'atmosfera di H_2, la CO_2 adsorbita viene convertita a CO in maniera selettiva. Tale operazione in stato non stazionario è realizzata in modo isotermo. In particolare, ci si è rivolti allo studio del comportamento catalitico di catalizzatori supportati, in cui rame e potassio sono le specie attive.

É stata esaminata l'attività catalitica di una serie di catalizzatori supportati a base di rame sintetizzati con il metodo di impregnazione a secco. I prodotti di reazione sono stati analizzati mediante spettroscopia FTIR, mentre la fase attiva per i processi di cattura e riduzione è stata studiata attraverso molteplici tecniche di caratterizzazione (XRD, BET, TPR, SEM, TEM, Raman ex-situ e in-situ). Il potassio risulta fondamentale nel processo di cattura, mentre la presenza del rame determina la reversibilità del processo e la rigenerazione del catalizzatore. La capacità di cattura del catalizzatore aumenta con l'aumentare della quantità di potassio fino al raggiungimento di un massimo. In modo simile, anche il rame può essere aggiunto in quantità ottimale, data dal compromesso tra creazione di siti interfacciali per l'adsorbimento della CO_2

e dispersione omogenea. In questo lavoro vengono riportate osservazioni riguardo il meccanismo di cattura, ponendo particolare interesse alla formazione della fase attiva per la cattura della CO_2. Il CO risulta coinvolto nell'adsorbimento, mentre il primo ciclo redox contribuisce alla creazione della fase attiva per il processo CCR, fortemente influenzato dalla presenza di rame e potassio.

Dal confronto tra catalizzatori simili supportati da materiali differenti, è stato indicato come la dispersione delle specie attive promuova l'attività catalitica. Anche la modifica dei parametri di sintesi ha condotto al miglioramento della dispersione.

L'ottimizzazione dei parametri di processo, quali temperatura di reazione e portate dei reagenti, e di sintesi, ha permesso di raggiungere un periodo di cattura completa dei CO_x di circa 100 s. Nello stesso intervallo, è stato possibile convertire a CO il 65% della CO_2 adsorbita, evidenziando la potenzialità del processo di CO_2 Capture and Reduction come strategia per l'utilizzazione della CO_2.

Contents

Introduction

Greenhouse gases are characterised by molecules whose links can vibrate when subjected to IR heat radiations coming from the soil, absorbing and trapping part of them close to the planet surface. This phenomenon keeps the stratosphere warm enough for life. However, the Intergovernmental Panel on Climate Change (IPCC) has reported that the excessive emissions of greenhouse gases (GHGs) to the atmosphere are the primary source of modern climate change and the consequent warming of the Earth. The Paris Agreement on climate change promoted by UNFCCC, entered into force on 4_{th} November 2016, binds all Nations to strive for climate-neutrality before the end of the century. The main target imposed is keeping the increase in average global temperature below 2 °C above the pre-industrial levels, aiming to limit it to 1.5 °C. To pursue such ambitious goals, the global peak of greenhouse gases emissions must be reached as soon as possible. Long-term policies to tackle this emergency are based on the transition to decarbonisation of energy supply, but strategies in the short/mid-term are focused on the development of effective methods for the removal of these threatening chemicals from flue gases. Carbon dioxide is the most important of such gases, as it represents the major anthropogenic contributor to the greenhouse effect. CO_2 concentration in the atmosphere increases every year, and according to most recent data it has risen massively from the pre-industrial value of 280 ppm to 400 ppm in 2015. The most promising pathways to address the abatement of the carbon footprint in the last decades are the Carbon Capture, Utilisation and Storage (CCS) and the Carbon Capture and Utilisation (CCU) methods.

CCU technologies not only aim to reduce the amount of CO_2 released in the atmosphere, but also to convert them in added-value products through different processes in a short-term period. Several processes able to covert CO_2 into alternative raw materials for chemicals, polymers and fuels exist. The main issue of such systems is the requirement of CO_2 feedstocks richer than flue gases coming from fossil-fuel power plants, in which generally CO_2 concentration varies between 3 and 15% on volumetric bases. For this reason, this thesis is focused on a new type of catalytic process under unsteady-state condition which converts efficiently CO_2 to syngas. The basic idea of this technology, called CO_2 Capture and Reduction (CCR), is to operate the reaction in a chemical looping mode, performing the process into two different phases. CO_2 contained in the flue gas stream is firstly chemically adsorbed on the catalyst to form carbonate species during the capture phase, and it's then converted to CO in the reduction phase using H_2 as a reducing agent, involving at same time the catalyst regeneration. The sustainability of the process is even furtherly enhanced if the H_2 production is linked to renewable energy sources. The most interesting benchmarks to assess CCR for syngas production are the CO_2 capture efficiency, the CO selectivity, and the H_2/CO ratio in the effluent stream.

The purpose of this work is to optimise the CCR process parameters so as to propose a specific application of this technology, matching it both with upstream and downstream production plants. This would have a huge impact on the closure of the carbon cycle, since it allows to obtain the building blocks for the majority of products normally derived from fossil feedstocks, simultaneously reducing significantly CO_2 emissions without any energy-intensive separation process. Moreover, the thesis tries to give an insight on the reaction mechanism, which is very effective, unique and still not completely clear. This work is organised as follows:

Chapter 1: Current CO_2 emissions and CCR process concept
This chapter gives an overview on the global current situation regarding greenhouse gases emissions and their effect on Earth surface temperature. During the first period several scientific articles were read. A general review on CCU techniques is proposed as a background of the innovative CO_2 Capture and Reduction process, and details on its different stages and possible applications are discussed. Here the catalyst materials are presented and the main factors affecting the process performance are introduced.
Chapter 2: Materials and experimental methods

This chapter describes the experimental setup, the catalyst synthesis and catalyst characterisation methods, the experimental tests operated and the catalytic testing analysis techniques.

Chapter 3: Catalysts characterisation

This chapter collects the results obtained from catalysts characterisation analyses. In particular, XRD, TPR, BET, SEM and TEM techniques were used.

Chapter 4: Catalytic activity and insights in the CO_2 capture mechanism

This is the core chapter of this work. Experimental results are presented here. Catalytic tests results are discussed, focusing the attention on the relations between catalyst composition, surface species and catalyst activity in order to propose some insights regarding the reaction mechanism and the efficient activation of the catalyst for CO_2 capture and reduction.

Chapter 5: Process parameters optimisation

In the last chapter, reaction temperature, reactants flow rates and catalyst synthesis conditions are addressed to maximise CCR potential.

The entire thesis project was carried out at the Faculty of Applied Sciences at the Delft University of Technology, within the Catalyst Engineering group. Experimental activities were supervised by professor Atsushi Urakawa and the PhD candidate Donato Pinto.

Chapter 1

Current CO_2 emissions and CCR process concept

In the last two decades, global warming and environmental sustainability have gained a main role in societal, industrial and academic stages. The Kyoto Protocol in 1997 first, the Paris Agreement in 2015 then, pushed the world to face actively the menace of climate change. The goal fixed by the Paris Agreement is the limitation of the global temperature increase to 1.5 °C above the pre-industrial level. To pursue such an ambitious aim, both advanced Economies and developing Countries must cooperate to promote green policies and finance sustainable technologies. Three key aspects need to be addressed: the mitigation of greenhouse gases (GHGs) emissions, particularly focusing of CO_2, the transition towards low-carbon renewable energy, with the replacement of fossil fuels, and the increase of the energy efficiency. The first chapter gives an overview of the present scenario of CO_2 emissions and global warming. General Carbon Capture and Utilisation (CCU) concepts and technologies are presented, along with the impact of exploiting CO_2 as the feedstock in the production of the so called C1-chemicals with a view to sustainable chemical industry. Later, the novel CO_2 Capture and Reduction (CCR) process concept is explained in depth and the aim of this thesis is discussed.

1.1 Global warming and CO_2 emissions

Greenhouse effect has been recognised as the main cause of global warming, since the Earth's surface temperature is rising along with the increasing atmospheric GHGs concentrations. The adverse consequences are the melting of glaciers, the rise of the sea level and the acidification of oceans. According to an ongoing temperature analysis conducted by scientists at NASA's Goddard Institute for Space Studies (GISS),[1] the average global temperature on Earth has increased by a little more than 1 °C since 1880. Two-thirds of the warming has occurred since 1975, at a rate of roughly 0.15-0.20 °C per decade. In the past, a 1 to 2 °C drop was all it took to plunge the Earth into the Little Ice Age. The global temperature depends on the balance between the energy received by the sun and the energy radiated back to the space, in the form of infrared radiation. The latter is significantly related to the atmospheric concentration of GHGs. In the Paris Agreement, IPCC set 450 ppm of CO_2 as the threshold value not to breach the 2 °C increase. The demographic and economic growth are the major responsible of the continuously higher global energy demand, causing a parallel increase of the GHGs emissions. The major concerns regard CO_2, as it constitutes the 81% of GHGs[2] (Figure 1.1).

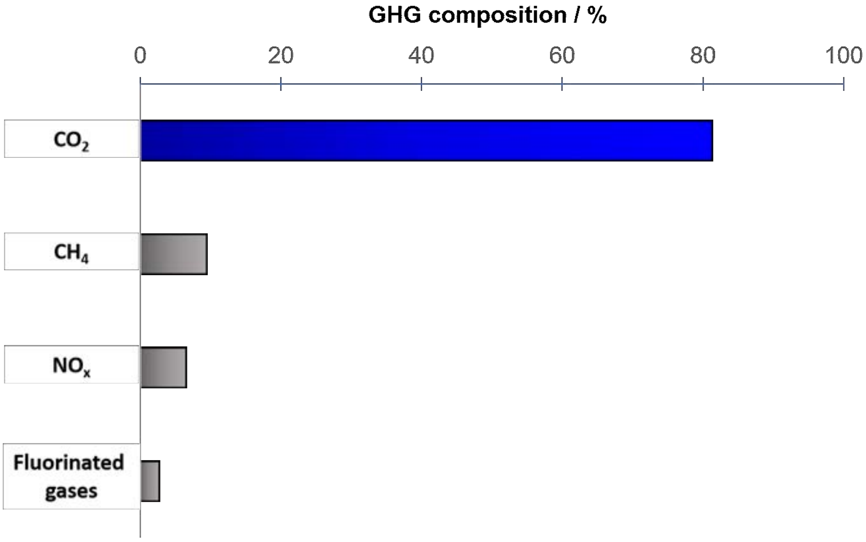

Figure 1.1: *Contribution of different species to the total amount of greenhouse gases. Adapted from EPA*[2].

According to BP statistics,[3] in 2018 CO_2 emissions coming from oil, coal and gas combustion reached the maximum peak of 33.8 Gt, with a growth rate of 2%, while the average growth rate in the period 2007-2017 was 1%. The electricity and heat sectors are by far the firsts contributors to CO_2 emissions, followed by transportation and industry[4] (Figure 1.2).

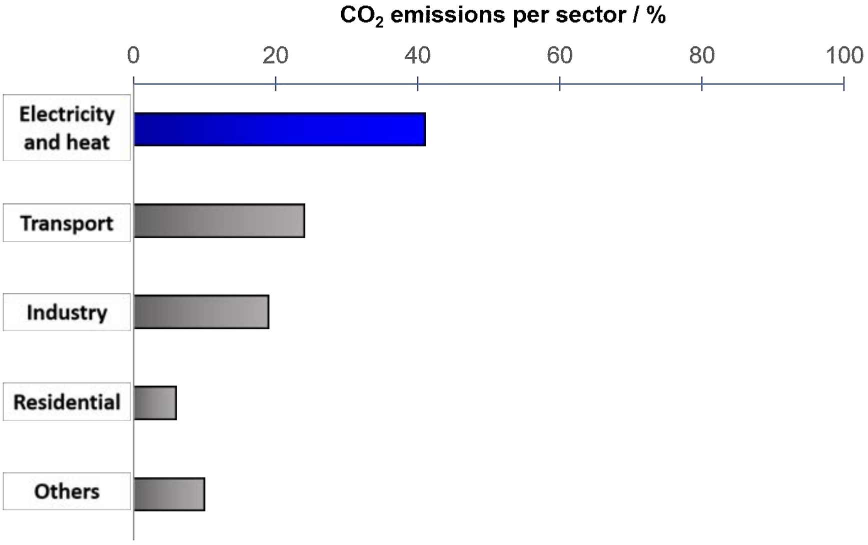

Figure 1.2: *Global CO_2 emissions by sector in 2017. Adapted from IEA[4].*

According to IEA,[5] in 2017 fossil fuels accounted for more than 81% of the world primary energy supply, therefore processes related to the combustion of fossil fuels emerge as a priority to tackle in order to mitigate CO_2 emissions. Oil constitutes the major energy source worldwide, but since 2000s coal-derived energy is increasing rapidly, mostly due to largely populated countries as China and India and their developing economies. Asia is the leader in CO_2 emissions, since coal in its various forms contains the higher amount of carbon per unity of energy generated. Although the great increase in GHGs concentration in the atmosphere in the last 150 years was provoked by well-developed Countries, nowadays these Economies promote emission mitigation policies such as carbon taxes and collaborations between governments and industries for sustainable technology research. On the other hand, emerging Economies are currently producing enormous amount of CO_2 due to social, economical and technological reasons. This reflects on the despair trend of the energy-related CO_2 emissions[6] shown in Figure 1.3.

Although a zero-carbon economy can be attained only after a fundamental change in primary energy sources, moving to renewable energies and sustainable fuels, this switch will be possible only in the long-term future. In the mid-term scenario, fossil resources will still have a central position in the energy generation and transportation sectors,

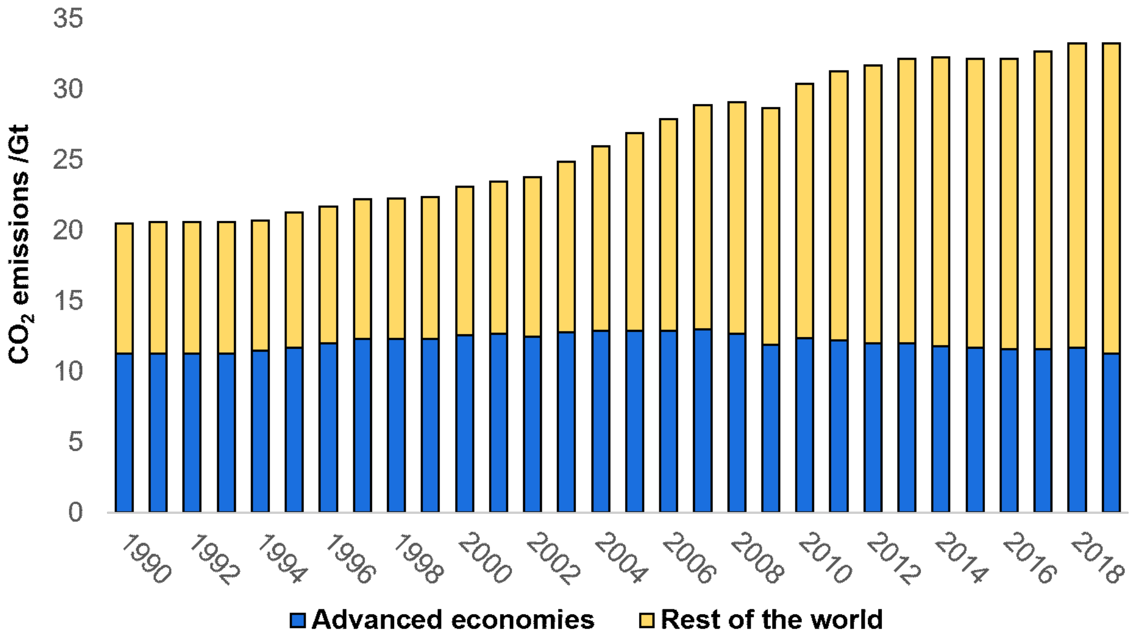

Figure 1.3: *Energy-related CO_2 emissions in advanced economies and other Countries in the period 1990-2019. Adapted from IEA*[6].

implying the reduction of anthropogenic CO_2 emissions on a global level as the only possibility to limit climate change.

1.2 Techniques for the reduction of CO_2 emissions

According to the Intergovernmental Panel on Climate Change, the most promising solutions for the reduction of CO_2 emissions are the Carbon Capture and Storage (CCS) and the Carbon Capture and Utilisation (CCU). These technologies are meant to be complementary: the former is related to the management of CO_2 as a waste, while the latter targets the cyclic reutilisation of CO_2 as a source. CCS techniques consist in the absorption of the CO_2 contained in different gaseous streams and in its subsequent permanent sequestration in geological reservoirs and saline aquifers. Despite the quite mature technology, in 2018 only 37 large scale plants existed at different development stages.[7] The main reasons of its stiff commercial deployment involves technical and economic aspects, such as the necessity of enormous gas storage capacity, the great energy penalty due to the regeneration of the solvents used for CO_2 absorption and CO_2 compression, the lack of an adequate transportation grid and the related infrastructures.[8,7,9,10] Moreover, it must be considered also the role of the public acceptance:

little information and suspicion about risks and trustworthiness of CCS led to social opposition and protests.[11] For this reason, CCU technology emerges as the ideal solution. CCU routes aim to create a circular carbon economy, exploiting CO_2 as a suitable source to move towards low-carbon energy and chemical industries. CO_2 utilisation techniques, besides reducing the volume of emissions in the atmosphere, allow also to reassess what is generally considered a waste by converting it into a technological fluid, minerals and added-value products. For long time CO_2 has been a feedstock of some industrialised chemical processes, as in the production of urea (1922), salicylic acid (1969) and methanol (1970). However, in recent years the interest in CO_2 exploitation has risen rapidly motivated by the determination to mitigate the climate change, and many efforts have been put in the development of new viable processes[12] (Figure 1.4).

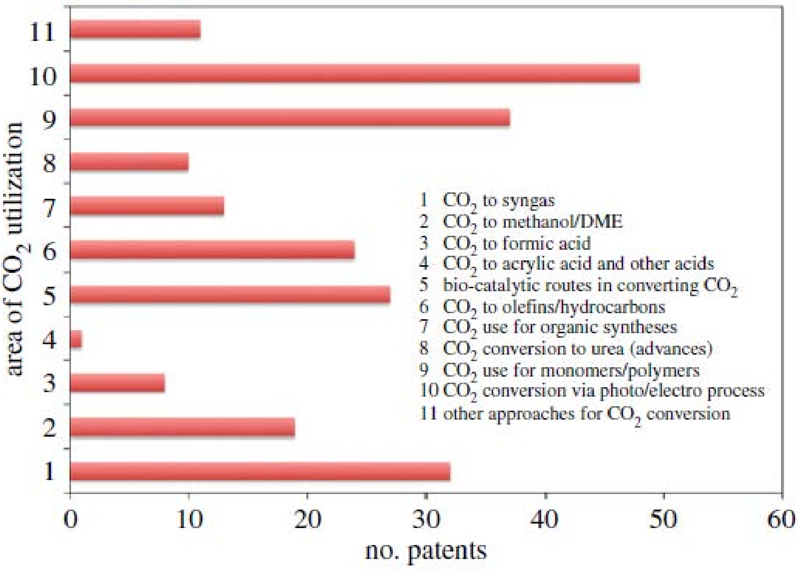

Figure 1.4: *Number of patents identified in the period 2008–2013 for the catalytic processes of CO_2 conversion to chemicals, classified according to 11 main classes of reactions. Reproduced from Ampelli et al.*[12].

For instance, in 2011 Bayers opened a pilot plant to produces polyurethanes based on CO_2 and CRI opened a plant for the production of methanol in Iceland which utilises H_2 derived from geothermal electricity.[12] This new scenario in which CO_2 is at the core of chemicals and energy production is supported by continuous breakthroughs in heterogeneous catalytic systems for its activation.

Many controversies arise on the effective potential of CCU to contrast global warming, mainly targeting two aspects: the duration of CO_2 immobilisation and the capacity to contribute to CO_2 emission reduction. The key point in the first case is to consider the amount of avoided CO_2 instead of the used CO_2 when comparing a CCU system with respect to a process on stream. Indeed, we can find several examples of CO_2-based processes that minimise emissions while obtaining the same product with respect to the common industrialised process.[13,14,15] In this perspective, a short-time-cycle chemical or commodity obtained substituting CO_2 to fossil fuels implies a cumulative emission reduction effect in the long-term. In addition, these processes are usually safer and both energy and material more efficient, providing a further economic incentive for the introduction of CO_2 as the alternative carbon feedstock in the supply chain. According to Aresta et al.[16], to face the second problem a preliminary classification of CO_2-based reactions should be done, separating those in which CO_2 is incorporated in the final product from the ones in which CO_2 is converted to a reduced form. In the first class we found most of compounds belonging to the chemicals market, in the other we have fuels. In the best of the cases, it is foreseen that CO_2 utilisation for chemicals production will increase to about 330 Mt per year in 2030. In a near future perspective this contribution to the total CO_2 emission reduction would be irrelevant. The fuel market instead is estimated to be 12-14 times that of chemicals, therefore CO_2 conversion into fuels must be the target to profitably exploit large amounts of it, and the impact on the emission reduction would be substantial.[16,17] In their work focused on the impact on GHG emissions arising from the 20 large-volume chemicals projected in 2030, Kätelhön et al.[18] estimated a substantial climate change mitigation potential considering a scenario characterised by the production of these chemicals from CO_2-based methanol, methane, olefins, BTX, carbon monoxide, ethylene oxide and styrene. More precisely, the annual emission would decrease from 4.2 to $0.7\,\mathrm{Gt}_{CO_2-eq}$.

CO_2-based synthetic fuels can provide the solution to manage the intrinsically fluctuating supply of renewable energy until new efficient energy storage techniques will be developed, and they can face the dependency on external suppliers of Countries without internal sources of fossil fuels. Besides, all methods based on renewable energy sources (hydropower, geothermal energy, wind and solar energy) produce electrical energy as output. However, electrical energy does not integrate well into chemical production, except as utility: most of the industrial chemical processes are based on the use of heat as the source of energy for the chemical reaction and considering the oil refining sector, only about 5% of the input energy is used as electrical energy.[19] As last, energy-dense liquid hydrocarbon fuels overperform electricity and H_2 potential in the automotive sector, since the lower storage energy densities of batteries and H_2 severely limit the driving distance.[20] Therefore, considering the already established worldwide delivery infrastructure, the exploitation of liquid hydrocarbon fuels would avoid also the technical and economical challenges of an efficient H_2 distribution grid, which is one of the major issues of the H_2 economy.[17]

There are two crucial aspects towards the deployment of CO_2 as a synthon for fuels at commercial scale. Firstly, from a chemical point of view, the high stability of the molecule. Secondly, regarding the catalytic processes involved for its conversion, the required purity of the feedstock. CO_2 valorisation chemistry requires high energy reducing reaction partners, such as H_2. In addition, given the enormous potential usage of CO_2, these reactions must be catalytic in order to operate in as mild conditions as possible, and the catalyst must involve low cost and earth-abundance. It is broadly accepted that H_2 supply is the most relevant factor to determine the environmental benefit of CO_2-based products with respect to the fossil-based ones. In their LCA study, Sternberg et al.[21] showed how all CO_2-based C1-commodities would be favorable for the global warming impact only if H_2 were produced through water electrolysis using renewable electricity. In fact, nowadays H_2 production is mainly produced by fossil resources via reforming technologies, affecting positively the anthropogenic carbon balance. To this purpose, advanced processes with milder carbon footprint will positively reduce the impact of H_2 production. An example is the development of reforming technologies that directly consume CO_2 to assist CH_4 conversion (dry reforming, bi-, tri-reforming). Different sources of renewable energy would also have a different effect on climate change mitigation, with wind-derived electricity being the cleanest. CO_2 sources instead can be generally divided into 3 classes, namely precombustion, oxy-fuel combustion and post-combustion stream gases. These lasts have drawn great attention both because of the ready expertise of their treatment and for the possibility of retrofitting existing fossil-fuel power plants to bridge them to CO_2 reuse. Numerous paths have been proposed to convert efficiently CO_2, although in most of these technologies a relatively high-purity feedstock is required. CO_2 emitted from power and industrial plants is in the range 3-15%vol, and it is generally diluted with many different compounds, such as O_2, N_2, H_2O, NO_x and SO_x. Nowadays large-scale post-combustion CO_2 separations are mainly based on wet scrubbing around 40 °C with amine sorbents such as MEA, DEA and MDEA; despite their proven efficiency, they imply several setbacks, first and foremost the high operation costs. In fact, in addition to the corrosive nature of the amines, their fouling tendency and the treatments required for their disposal, these processes are penalised by the high regeneration energy of the liquid sorbent, associated with the carbamate hydrolysis. For instance, a typical MEA regeneration stripping tower must operate at relatively elevated temperatures (100-140 °C) with respect to the CO_2 absorption unit.[22] According to the IPCC 2005 special report[23], CO_2 capture costs for a post-combustion electric power plant increase the energy requirement by 24-42%, and it is estimated that the cost for CO_2 capture in a fossil power plant is 15-75 $ per ton of CO_2 processed, while for example its transportation and storage account for 1-8 $ and 0.5-8 $ respectively.[24] To overcome such problems, in recent years many researches have focused on solid sorbents as an alternative, given their potentially less-energy-intensive separation technology. In fact, differently from liquid sorbents, solid sorbents can be applied over a wider temperature range, entailing less waste during cycling and a less environmentally hazardous disposal.[25] Among others, zeolites, activated carbons, hydrotalcites, metal-organic frameworks and metal oxides have risen great interest. However, for most of these materials the desorption is induced by a temperature or pressure swing, although ideal CO_2 capture and adsorbent regeneration should be performed at low temperature and isothermally, so as to minimise energy requirement and parasitic energy loss.[26] In this context, a new catalytic unsteady-state process for CO_2 utilisation is proposed, which shows to have a strong potential in reducing global emissions and versatility of applications.

1.3 CCR process for synthesis gas production

The CO_2 Capture and Reduction process is a catalytic process that allows to convert efficiently CO_2 directly from the emitting source. It is performed in unsteady-state operation by the alternation of two phases: the capture, in which CO_2 is captured by the catalytic material and a CO_2-free stream is released, and the reduction, in which an H_2 flow converts the captured CO_2 to valuable products. The ability of dealing with diluted CO_2 streams gives the process the advantage of bypassing some energy-intensive separation and purification steps. Depending on the active metal, CCR can be suitable to produce different C1 commodities, with methane[27] and syngas[28,29] being the most promising targets. In this work, the attention is focused on the production of syngas.

Syngas is a mixture of mostly CO and H_2 in variable ratios, that constitute the main building block to produce a great variety of products through the Fischer-Tropsh process, such as gaseous and liquid fuels. Relevant industrial processes benefit from syngas utilisation. According to Joo et al.[30], the route involving conversion of CO_2 to CO and its subsequent hydrogenation to methanol, better known as CAMERE process, leads to 20% higher methanol yields than the direct hydrogenation of CO_2 to CH_3OH. Syngas has its relevance also in the field of chemical energy storage: in fact, the Power-to-Syngas pathway results in bigger environmental advantages opposed to Power-to-SNG (synthetic natural gas).[31] At present, large-scale syngas production is realised by steam reforming of methane (SRM) combined with the water-gas shift reaction (WGS), and in minor part by autothermal reforming and the catalytic partial oxidation of methane. All these processes are based on fossil resources. In recent years, low-carbon alternatives for syngas production have drawn great attention. The most promising and investigated are dry reforming of methane, the biomass gasification and pyrolysis and the reverse water gas shift (rWGS). In particular, rWGS implies the catalytic reduction of CO_2 to CO by means of H_2, where H_2O is obtained as a side product according to the reaction:

$$\mathrm{CO_2 + H_2 \rightleftarrows CO + H_2O} \qquad \Delta H^\circ_{298} = 41 kJ/mol \tag{1.1}$$

Excess H_2 is required to obtain a syngas mixture as reactor effluent. rWGS has attracted many attentions because it involves the conversion of CO_2 into the much more reactive CO. Due to its endothermic nature, rWGS is thermodynamically favored at high temperature and the CO_2 conversion is maximised by the increase of the H_2/CO_2 ratio. The thermodynamic equilibrium of reaction products was analysed by Kaiser et al.[32] using a H_2/CO_2 feed ratio of 3:1 and it is shown in Figure 1.5. Below 600 °C methane is the main product, while CO is dominant above 700 °C. However, at such high temperature conditions CO_2 conversion is below 70%.[33] Reducing the reaction temperature would be essential to reduce energy consumption. However, at low temperature undesired side reactions compromise rWGS efficiency, in particular the water-gas shift and the Sabatier reactions. In this sense, developing catalyst selectivity towards CO becomes crucial to avoid downstream product separation while limiting operation costs.

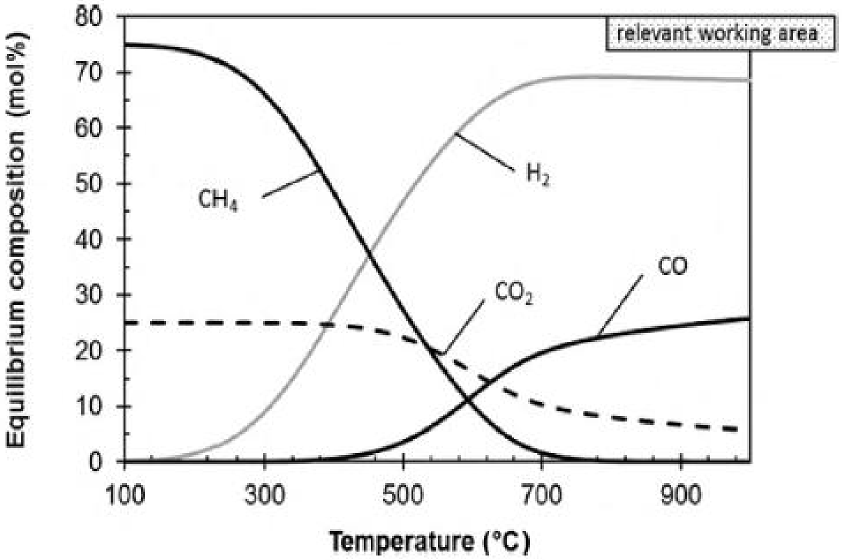

Figure 1.5: *Influence of temperature on the thermodynamic equilibrium of the rWGS reaction at* 1 bar *and* H_2/CO_2 *molar ratio of 3/1. Reproduced from Kaiser et al.*[32].

When dealing with heterogeneous catalytic systems, optimal operating conditions under steady-state regime not necessarily correspond to the absolute performance limit of the process. In fact, forcing the change of reaction parameters in a dynamic or cyclic way proved to increase process performance in several cases.[34] In the CCR process, the forced unsteady-state operation regime is generated by periodically switching the gas atmosphere inside the reactor. The catalyst is subjected to continuous changes, mainly in composition and structure, and the average catalyst activity and selectivity can be enhanced compared to the steady state regime.

The possibility to achieve CO_2 capture and its conversion to CO into an isothermal unsteady-state operation is related to the exploitation of a bifunctional catalyst. The CCR process is characterised by two distinct phases, cyclically carried out in a packed bed reactor. In the first one, denoted as capture phase, a gas stream containing CO_2 is fed to the packed bed reactor. CO_2 is then chemically adsorbed on the storage sites of the catalyst. By switching the gas atmosphere in the reactor, we enter the second phase of the process, called reduction phase. Here, pure H_2 is fed to the reactor and accounts for the reduction of the adsorbed CO_2 to CO. With this, the simultaneous regeneration of the catalyst active sites for capture is achieved. The product gas stream contains the formed CO and excess H_2, thus constituting a syngas mixture. A graphical representation of the process is illustrated in Figure 1.6. A challenge for the optimisation of this stage would be the achievement of a H_2/CO ratio suitable for downstream processes. As an example, Fisher-Tropsh process and methanol synthesis would benefit from a syngas with H_2/CO ratio around 2:1. The H_2O formed as by-product can be separated from the syngas by condensation.

As previously proposed, the CCR process effluent could be suitable for the production of liquid hydrocarbons and transportable synthetic fuels through the Fischer-Tropsch process. Main reactions involved in this process are the synthesis of paraffines and olefines, according to Equation 1.2 and Equation 1.3 respectively.

$$(2\,n+1)\,\mathrm{H_2} + n\,\mathrm{CO} \longrightarrow \mathrm{C}_n\mathrm{H}_{2n+2} + n\,\mathrm{H_2O} \qquad \Delta H^{\circ}_{298} < 0 \tag{1.2}$$

$$2\,n\,\mathrm{H_2} + n\,\mathrm{CO} \longrightarrow \mathrm{C}_n\mathrm{H}_{2n} + n\,\mathrm{H_2O} \qquad \Delta H^{\circ}_{298} < 0 \tag{1.3}$$

About 75 to 80% of the useful product is olefinic, with the remainder being paraffinic. FT process is generally carried out in a temperature and pressure range of 220-350 °C and 25-40 bar. Aromatic and cyclic compounds are formed only at temperatures appreciably greater than 300 °C, thus by a complete thermal decomposition process followed

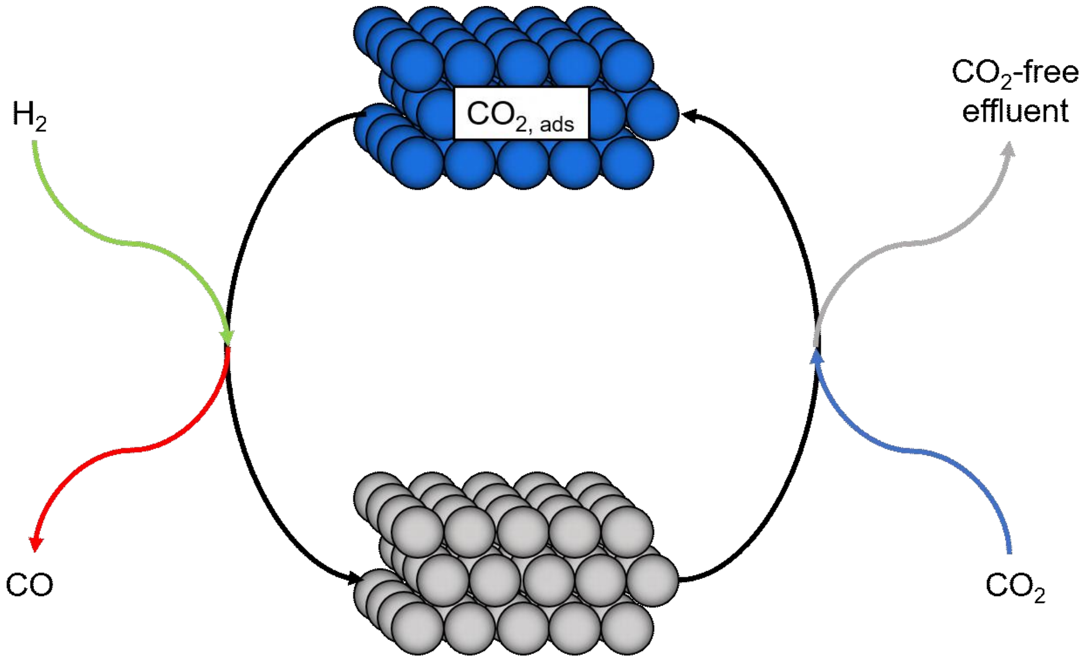

Figure 1.6: *Illustration of the CCR process for syngas production.*

by a reconstruction process. Most suitable catalysts are Co- or Fe-based catalysts, depending on the feedstock: the former is suitable for high hydrogen-to-carbon ratio, the latter for low H_2 content syngas, since it promotes the water-gas shift reaction (inverse of Equation 1.1). Fisher-Tropsch products can be furtherly upgraded through different operations: fractionation, hydrotreating, catalytic reforming, alkylation and isomerisation allow to obtain a variety of energy-dense liquid fuels, such as LPG, gasoline, naphtha, kerosene and diesel.

Chemical looping for CO_2 capture can be applied considering a cyclic process conducted in two different reactors, the carbonator and the calciner.[24] In the carbonator, catalyst particles are the carrier for carbon dioxide. Usually, metal oxides act as good sorbents forming their correspondent metal carbonates. By a temperature swing, they can subsequently be regenerated releasing a pure CO_2 stream. The calcium oxide-calcium carbonate looping is a well-known system, as it was found to be suitable both for post-combustion gas treatment and for the enhancement of the WGS reaction, shifting the thermodynamic equilibrium of the reaction towards H_2 production. This operation simplifies the subsequent CO_2 compression, transportation, and sequestration steps. However, catalyst regeneration is an energy-intensive step, since high temperatures are required.

The great advantage of CCR is its application in a chemical looping concept, as described by Bobadilla et al.[28] and presented in Figure 1.7. This system consists of two parallel CCR reactors, one capturing CO_2 from the source flow (i.e. flue gas) and the other one reducing the adsorbed CO_2 with H_2 flow. At catalyst saturation, the gases fed to the reactors are switched: in this way the first reactor will now operate the reduction phase, while the second will capture CO_2. This kind of system can be operated isothermally, and trough a correct synchronisation of the feed gas streams it is possible to obtain a CO_2-free effluent and syngas as an added-value product. Alternative configurations for the reactor have been proposed, for example including a moving catalyst in a fluidised bed configuration, where the reactors are fixed and the catalysts is carried through them by the flow, overcoming heat transfer limitations and heat management issues.[35,36] To match with the time required for CO_2 capture, the reduction of adsorbed CO_2 must be fast enough, and since the reduction stage is endothermic, higher temperatures favor its conversion. Bobadilla also demonstrated the ability of this process to deal with O_2 and H_2O impurities.[28] This kind of system can be a breakthrough for CCU, since it allows the in-situ CO_2 separation directly from flue gases and isothermal process conditions, which eliminates the need for an expensive gas separation and purification unit and lower energy requirements.

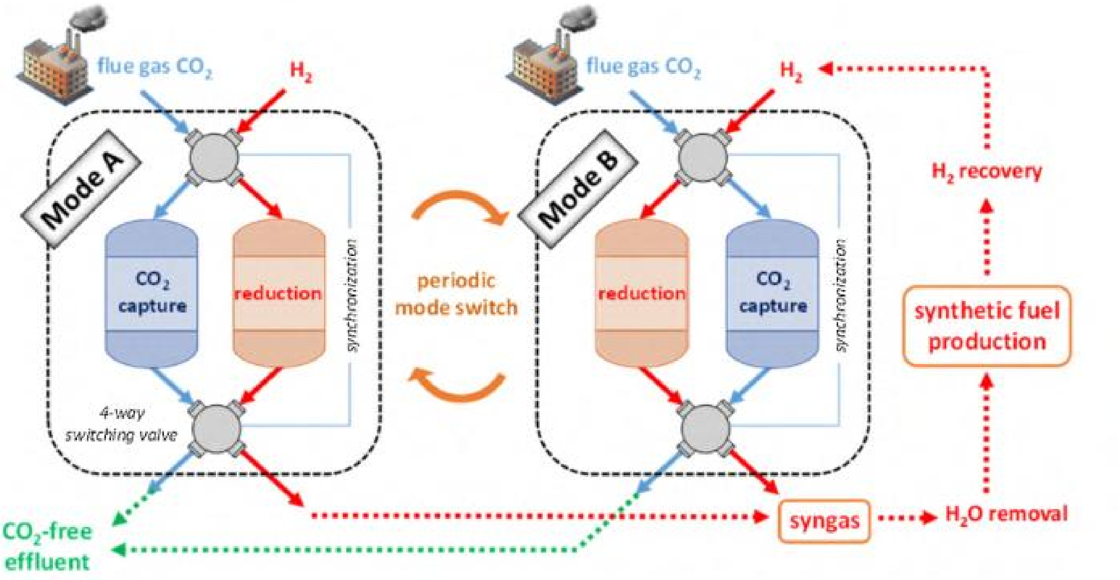

Figure 1.7: *Integrated two-reactor CCR process for continuous CO_2 capture and reduction. Reproduced from Bobadilla et al.*[28].

Therefore, a suitable catalytic material for CO2 capture and conversion must present different functionalities:

- Reversibility of the CO_2 adsorption step, i.e. regenerable catalyst, since the objective of the process is the conversion of CO_2 rather than its immobilisation;
- High CO_2 adsorption capacity at operation temperature;
- Fast reduction of stored CO_2 and parallel fast regeneration of the catalyst;
- High conversion of stored CO_2 and high selectivity to CO;
- Stability and durability of operation;
- Made of earth-abundant, nonhazardous materials.

1.4 Aim of the Thesis

Due to the process novelty, the state of art on CCR counts only few works in literature. Different catalytic systems were found to satisfy these requirements proving their efficiency for CCR. The most relevant are K-promoted mixed metals on hydrotalcite[28] and K-promoted Cu on alumina[29]. By using Ni as the active metal of the catalyst, Hu et al.[27] tailored this process approach to CO_2 methanation. The last mention goes to the research of Daza et al.[37,38], who interestingly developed a CCR process over doped cobalt and iron perovskites. In this work, the K-promoted Cu/Al_2O_3 system has been investigated. Proven its activity and selectivity to form CO, there is difficulty in determining the exact mechanism of reaction over this catalyst. This is crucial to rationally design a catalytic process with high efficiencies and maximum CO_2 uptake and conversion. Involved catalysts may undergo continuous reconstruction under realistic working conditions, which unfortunately causes controversial results concerning the active sites and reaction mechanism of CO_2 reduction. In our particular case, the potassium state is difficult to identify as well as its role in the active phase, since it eluded the common characterisation techniques. However, determining the active phase would be of relevant importance to further develop catalyst functionalisation. A promising solution may be the real-time monitoring of the dynamic evolution of the catalysts and reaction intermediates by in situ techniques.[39]

Al_2O_3 was chosen as the catalyst support for its good thermal stability and the high surface area, which should enhance catalyst durability and active sites dispersion. The material scope was extended through this work to determine the key features of the support, including TiO_2- and ZrO_2-based systems. Besides being earth-abundant, copper is extensively recognised as an active metal for rWGS thanks to its ability to perform rWGS at low temperatures[40] and its high selectivity towards CO, with little or no production of CH_4 as a side product.[41,42,43] Potassium was chosen as it showed promising performance for CO_2 capture among the alkali metals in different applications, both as a supported solid material and in aqueous solution.[44,45,46,47] Moreover, several studies reported its promotion effect in rWGS.[46,48,49,50] This project is oriented to the deeper investigation of the CCR process, particularly focusing on:

- Evaluation of the performance of catalysts with different loadings of active metal, promoter and support material, along with their characterisation;
- Unravelling fundamental steps and active sites involved in the reaction mechanism;
- Optimisation of the process performance using the better performing catalyst for potential inclusion in the treatment of post-combustion flue gases of a common fossil fuel power plant.

Chapter 2

Materials and experimental methods

In this chapter the instrumental equipment, experimental methodologies and analysis techniques utilised for the thesis work are presented. All experiments were performed within the Catalysis Engineering laboratory, belonging to the Faculty of Applied Sciences at Delft University of Technology.

2.1 Time-resolved FT-IR spectroscopy setup

Catalytic activity tests were performed in a fixed bed reactor. It is inserted in the setup schematically represented in Figure 2.1 and showed in Figure 2.2. Gas lines connected to this system are He, O_2, N_2, CO_2, CO and H_2. Gas flow rates are selected by means of mass flow controllers (Bronkhorst) to obtain the final composition of the reagent mixture. Reactants are sent to a quartz tube reactor of 6 mm diameter. A system of two automatic 4-way switching valves enables to perform cyclic unsteady-state regime by alternating three different gas atmosphere over the catalyst. A USB camera was mounted in order to observe the eventual emergence of surface or bulk phase modifications producing colour changes in the visible range during the reaction. To remove excessive water from the flow and prevent damage to the analytic instruments, the outlet gas is passed through a condenser attached to a chiller. The reaction product mixture is then analysed by a FT-IR spectrometer (Bruker Alpha), with a time resolution of 5 s per spectrum. Pressure indicators and metering valves are placed for keeping the pressure of the vent line and of the reactor line in balance and to prevent pressure drops. In the following, each part of the setup will be described in detail.

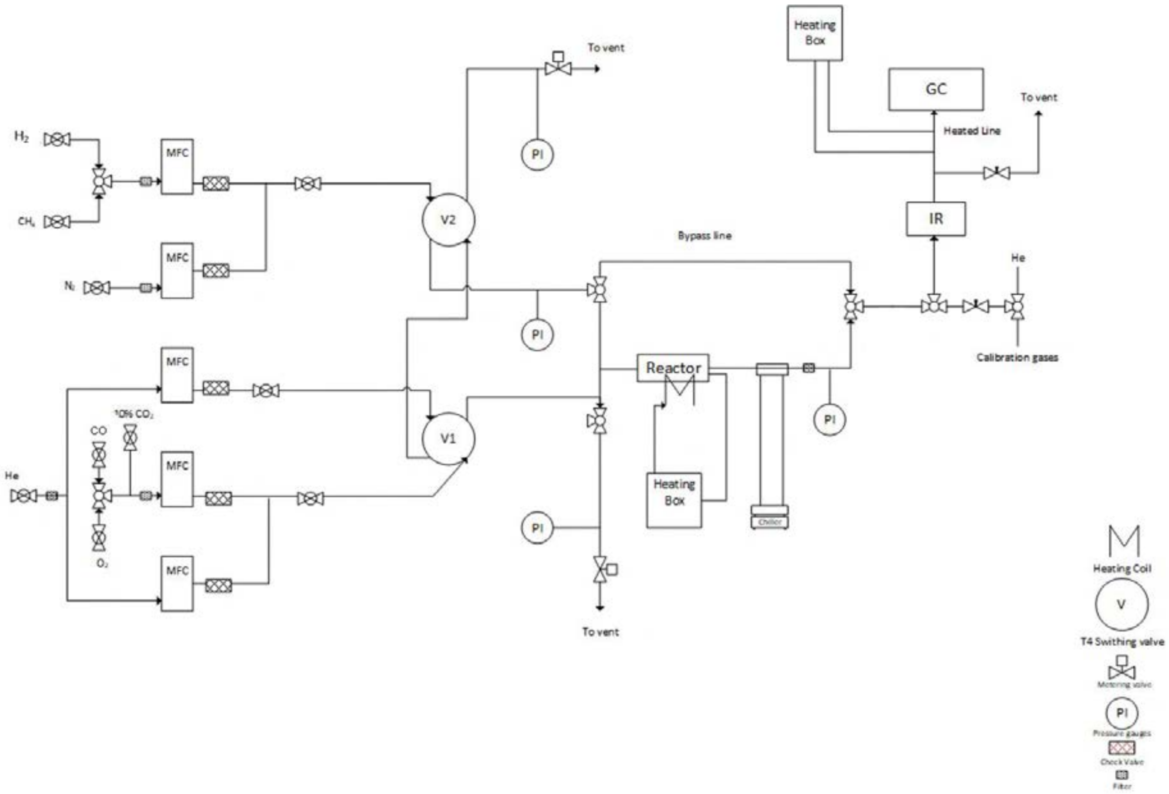

Figure 2.1: *Scheme of the laboratory experimental setup for catalytic activity tests.*

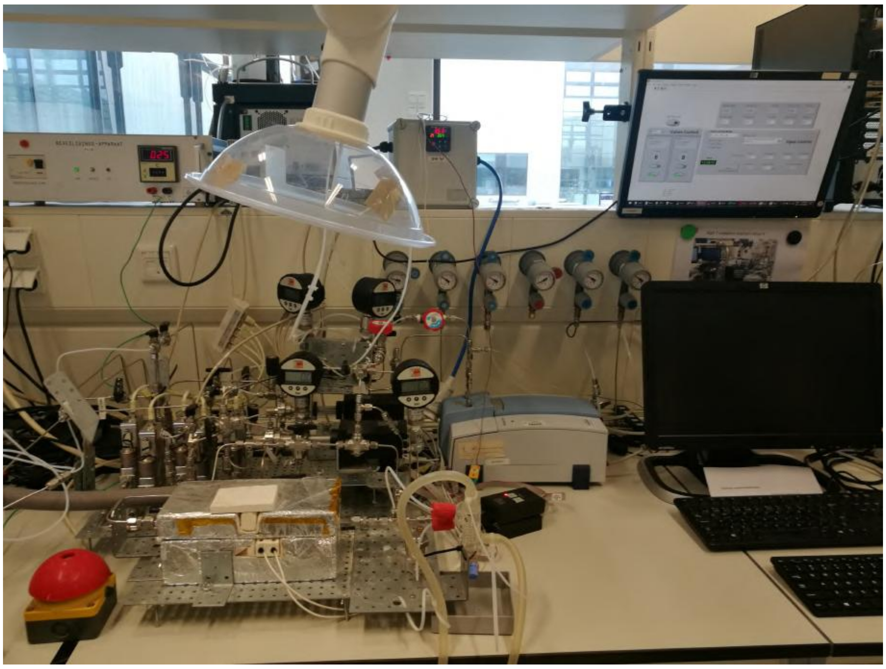

Figure 2.2: *View of the laboratory experimental setup for catalytic activity tests.*

2.1.1 Mass flow controllers: Bronkhorst EL-FLOW Select

Bronkhorst EL-FLOW Select mass flow controllers (0-150 bar, 0-120 $\mathrm{mL\,min^{-1}}$, the range is calibrated with He, Figure 2.3) were used to control reactant gas flow rates fed to the reactor. They are automatic MFCs, remotely controlled. The measuring part of this instrument consists of a laminar flow element and a bypassing thermal mass flow sensor, which are filled with gas once the MFC has been connected to the line. The sensor consists of a capillary tube fitted with a heater and two temperature recorders. The heater heats the tube: as long as there is no flow, the two temperature sensors heat up evenly. The measured value is zero, and this signal is forwarded to the microprocessor. The set point from the analog port is compared to the measured value: if the latter is lower than the required value, the PID controller will actuate the control valve. The control valve consists of an electromagnetic coil exerting a force on the magnetic plunger holder. This results in a flow through the instrument. The gas flows through the laminar element, which serves as a perfectly predictable flow resistance, necessary for the calibration of the instrument. The resistance offered by the laminar flow element also ensures that a small portion of the feed is sent to the thermal sensor. The cold gas temperature is registered by the first temperature sensor, while the second one detects a higher temperature due to the heating of the gas by means of the heater. The temperature difference is a direct measure of the mass flow, according to the energy conservation law. This signal is compared to the desired value in the microprocessor. The electric current of the coil is then adjusted in order to open or close the valve orifice, in this way controlling the quantity of gas. The control circuit performs these operations in few milliseconds, ensuring a constant and stable gas flow.

2.1.2 4-way switching valves

A combination of two electric 4-way switching valves (VICI Valco) is installed in the setup to automatically alternate the gas pulse fed to the catalyst bed. Each valve consists of a two-position (A, B) microelectric actuator, a gearbox assembly and the interconnecting cables. In order to select between different gas flows to the reactor, this

Figure 2.3: *Bronkhorst EL-FLOW Select mass flow controller.*

system permits four different configurations, referred to as AA, AB, BA (not used) and BB. A schematic representation of each case is presented in Figure 2.4. Three main gas phases are utilized in the system:

- An oxidant phase in which O_2 or CO_2 and He as diluting gas can be fed together;
- A flushing phase consisting of pure He;
- A reducing phase, in which H_2 and N_2 as diluting gas can be fed together.

Considering the first valve, the flushing He line and the oxidant line are connected at the two inlets (port 1 and 3, respectively). One of the outlet line (port 4) goes to vent, while the other outlet line (port 2) is connected to the inlet (port 3) of the second valve. The reducing phase is connected to the other inlet (port 1) of the second valve. For the second valve, one of the outlet line (port 4) goes to vent, while the other outlet line (port 2) goes to the reactor. By selecting position A, the port 1 and 2 are connected, and so are 3 and 4. By switching to B position, port 1 and 4 are connected, and so are 2 and 3. In this way, by selecting the AA configuration, for both valves the port connections are 1-2 and 3-4, resulting in the venting of the oxidant phase at the first valve, the venting of the inert phase at the second valve and the feeding of the reducing phase to the reactor. On the contrary, in BB position, the oxidant phase will access the reactor. Ultimately, AB position will send the He flushing line to the reactor. For all the experiments the process scheme applied is BB, AB, AA, AB, obtaining the alternation of the oxidising and reducing phases and the inert flushing between them.

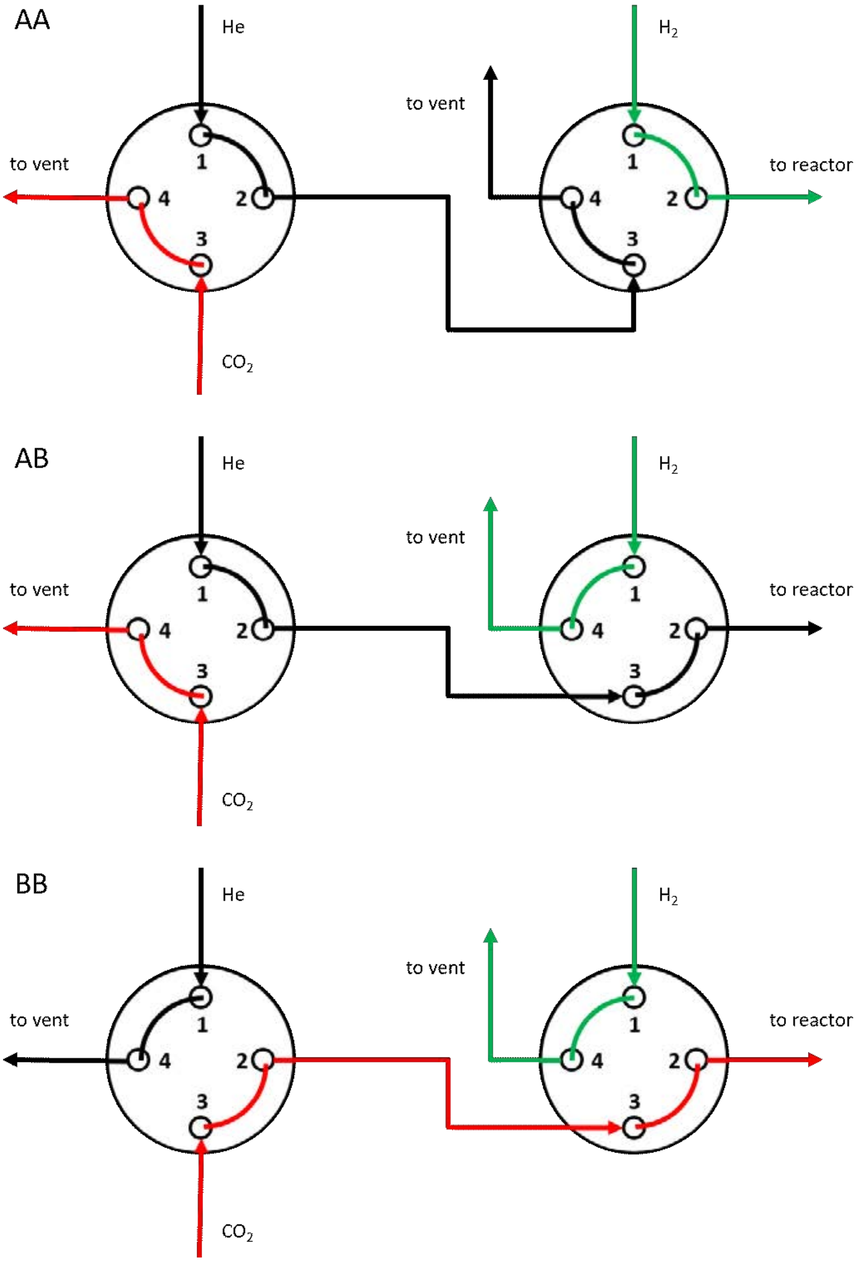

Figure 2.4: *Schematic of the three used configurations of the two electrically driven 4-way valves used for catalytic tests.*

2.1.3 Reactor tube

The reactor consists of a quartz tube with a 4 mm inner diameter and 1 mm wall thickness. Its length is 300 mm, while the catalyst bed length varies between 10 mm and 25 mm depending on the material (maximum length is obtained for alumina-supported ones). Quartz wool is used to pack the catalyst in position, avoiding possible particle drag. The reactor tube is wrapped into a metal jacket to ensure homogeneous distribution of the heat on the catalytic bed. In the reactor, the temperature is measured by a K-type thermocouple inserted from one end and kept at 1 mm distance from the catalyst. The heating system consists of a heating box containing a toroidal transformer and a PID system to control the amount of power released in order to reach the targeted temperature on the thermocouple. The current flows through a closed circuit in which an heating coil represents the resistive element dissipating the current in the form of heat. The heating coil is placed below the catalyst bed, to provide fast and confined heating. The reactor and the heating coil are insulated from the external environment by means of refractory bricks.

2.2 In situ Raman spectroscopy setup

CCR tests were performed in a fixed bed reactor, integrated in the setup schematically represented in Figure 2.5. The configuration is similar to the one of the previous experimental setup. Gas lines connected to this system are He, O_2, N_2, CO_2 and H_2. Gas flow rates are introduced in the reactor by means of mass flow controllers (Bronkhorst) to select the final composition of the reactant mixture. Reactant flows are sent to a quartz tube reactor. The alternating gas atmosphere between CO_2 and H_2 is made possible by means of a two-position pneumatic valve. The reaction product mixture is then analysed by a mass spectrometer (Omnistar GSD 320). Pressure indicators and metering valves are placed for keeping the pressure of the vent line and of the reactor line well balanced to avoid flow fluctuation in the reactor gas line. In addition, a remotely controlled moving support stage (Zaber console) for the Raman probe is present. Due to the proximity of the probe to the heating coil, the probe is cooled down by a glass jacket with water circulation to avoid its overheating. The whole setup is placed into a closed box for safety reason (3B class laser is used as radiation source).

Two fans enhance heat dispersion.

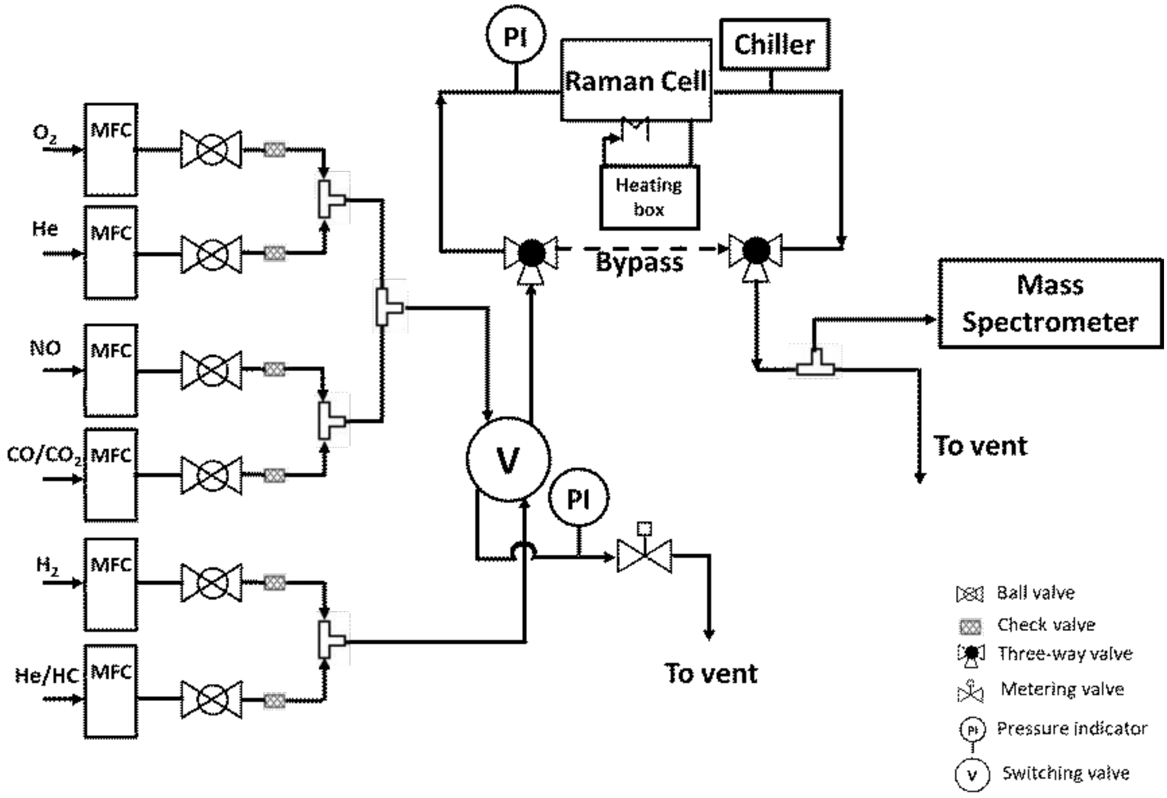

Figure 2.5: Scheme of the laboratory experimental setup for in-situ and operando Raman tests.

2.3 Analysis equipment

2.3.1 FT-IR specroscopy: Bruker Alpha FT-IR spectrometer

Fourier-transform infrared spectroscopy was used to analyse the gas mixture composition of the effluent. This technique is suitable for the analytic composition of solids, liquids or gases because it is able to simultaneously collect high-spectral-resolution data over a wide spectral wavenumber range. The FT-IR spectroscopy uses interferometry to record information about a material placed in the IR beam, since these spectrometers are all based on the Michelson interferometer. This element consists of a fixed mirror, a perpendicular moving mirror and a beam splitter. FT-IR technique shines a beam containing the full spectrum of wavelengths to be measured to a beam splitter, and a fraction of the light source is sent to each mirror. When reflected back by the mirrors, two beams of light recombine with each other at the beam splitter and they are focused on the sample. Since one mirror is movable, the path length between the two beams can be different, thus generating constructive or destructive interference. The intensity of the signal is amplified, and it can be represented as a function of time, and the resulting plot is called interferogram. The interferogram is digitally converted to the actual spectrum through the Fourier transform, obtaining the plot of the absorbance intensity as a function of the wavelength. Patterns in spectra help identify the sample, since molecules exhibit specific IR fingerprints. The instrument used in this work is an on-line Bruker Alpha FT-IR spectrometer, which allows for 5 s time-resolved measurements with a resolution of $4\,\mathrm{cm}^{-1}$. The wavenumber range is between 400 and $4000\,\mathrm{cm}^{-1}$.

The determination of the concentration of an IR-active compound is made possible by its correlation with the area of the absorbance signal, according to the Lambert-Beer theory. The instrument was calibrated for the quantitative estimation of CO_2, CO and CH_4 concentrations in flow. Different concentrations of these species were obtained from the nominal cylinder value or by dilution using He and N_2. For the diluted mixtures, the composition of the streams was determined from gas chromatography. Simultaneously, the IR absorbance area was calculated in a certain wavenumber range, specific for each compound. The selected spectral range are $2260\text{-}2280\,\mathrm{cm}^{-1}$, $2150\text{-}2170\,\mathrm{cm}^{-1}$ and $1220\text{-}1266\,\mathrm{cm}^{-1}$ for CO_2, CO and CH_4 respectively. A proportionality parameter ϵ was then determined as the ratio between the area and the concentration. In order to decrease the error in the measurement, three consecutive GC injection were performed for each concentration, along with three different IR spectra acquisition for each concentration point. To improve the signal-to-noise ratio and the accuracy of the calibration, each IR spectrum was the average of 100 successive scans. A plot of ϵ as a function of the absorbance area was then elaborated for each analyte and the equation of the fitting curve was used for determining the concentration during reaction. An example of the fitting curve is reported in Figure 2.6 for CO_2. This kind of procedure allows for concentration estimates with a relative error smaller than 1% (determined through the propagation of error principle). The experimental IR spectra coming from the analysis instruments were processed on MATLAB® to quantify species concentrations in the effluent stream.

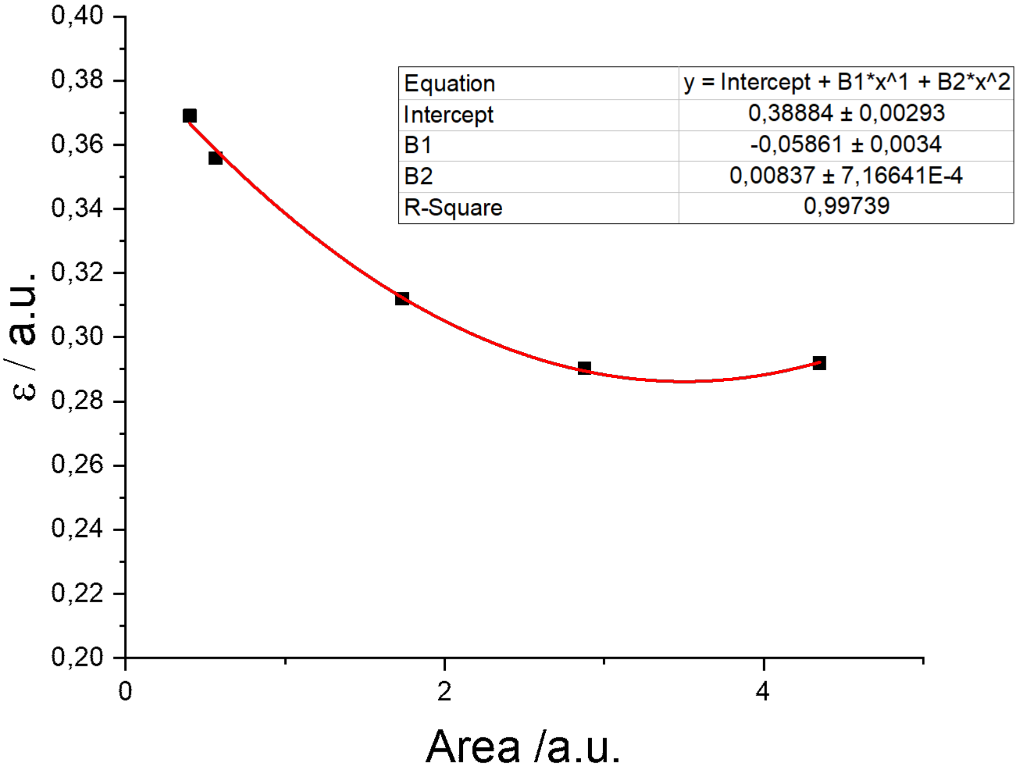

Figure 2.6: *Curve fitting of the experimental data points (black squares) for IR* CO_2 *quantification.*

2.3.2 Raman spectroscopy: PicoRaman spectrometer

Raman analysis of the catalyst were conducted ex situ, in situ and in operando by means of a PicoRaman spectrometer, a Class 3B laser product. A 532nm wavelength green laser is used as the excitation source. An optic-fiber connected probe is used both to carry the exciting radiation to the catalyst material and to collect the radiation induced on the catalyst species, which is then sent to a detector. Thanks to the TimeGate technology, PicoRaman has sub-nanosecond pulsed excitation and a time-resolved single-photon counting detector, enabling effective fluorescence rejection, which can be possibly generated by the sample. The SampleCube was used for ex situ measurements. It is an external sample compartment equipped with a light-tight sliding door. A quartz disk containing the sample can be placed inside this instrument, while the probe shaft can be inserted in a suitable probe port.

Raman spectroscopy is an analytic technique which provides information about the chemical structure, the crystallinity and the molecular interactions of the sample by detecting the chemical fingerprint from its low-frequency vibrational modes. It is based upon the interaction of light with the chemical bonds within the material. A laser is used as incident monochromatic radiation source in the infrared or in the visible, whose wavelength is very different from the absorption wavelength bands of the analyte. Raman spectroscopy working principle are presented in Figure 2.7. Most of the scattered light is characterised by the same wavelength as the incident radiation and it is not informative (Rayleigh scattering), but a small amount of radiation is scattered at different wavelengths, depending on the chemical bonds of the analyte. This phenomenon is called Raman effect. Two types of Raman scattering exist:

- Stokes scattering, characterised by higher wavelength (and lower energy) than the source wavelength;
- Anti-Stokes scattering, characterised by lower wavelength (and higher energy) than the source wavelength.

Vibrational or rotational modes are Raman active if the incident radiation implies a variation of the polarisability of the molecule. Each peak of a Raman spectrum corresponds to a specific molecular bond vibration, and this allows the sample identification.

2.4 Experimental procedures

In this section, catalysts preparation procedures are illustrated.

2.4.1 Catalyst preparation

All catalysts were prepared by the incipient wetness impregnation method.[51,52] According to this synthesis technique, the active metal precursor is first dissolved into milli-Q water (deionised water). It is then added to the catalyst support, previously crushed to obtain a fine powder. The volume of the aqueous solution of the metal

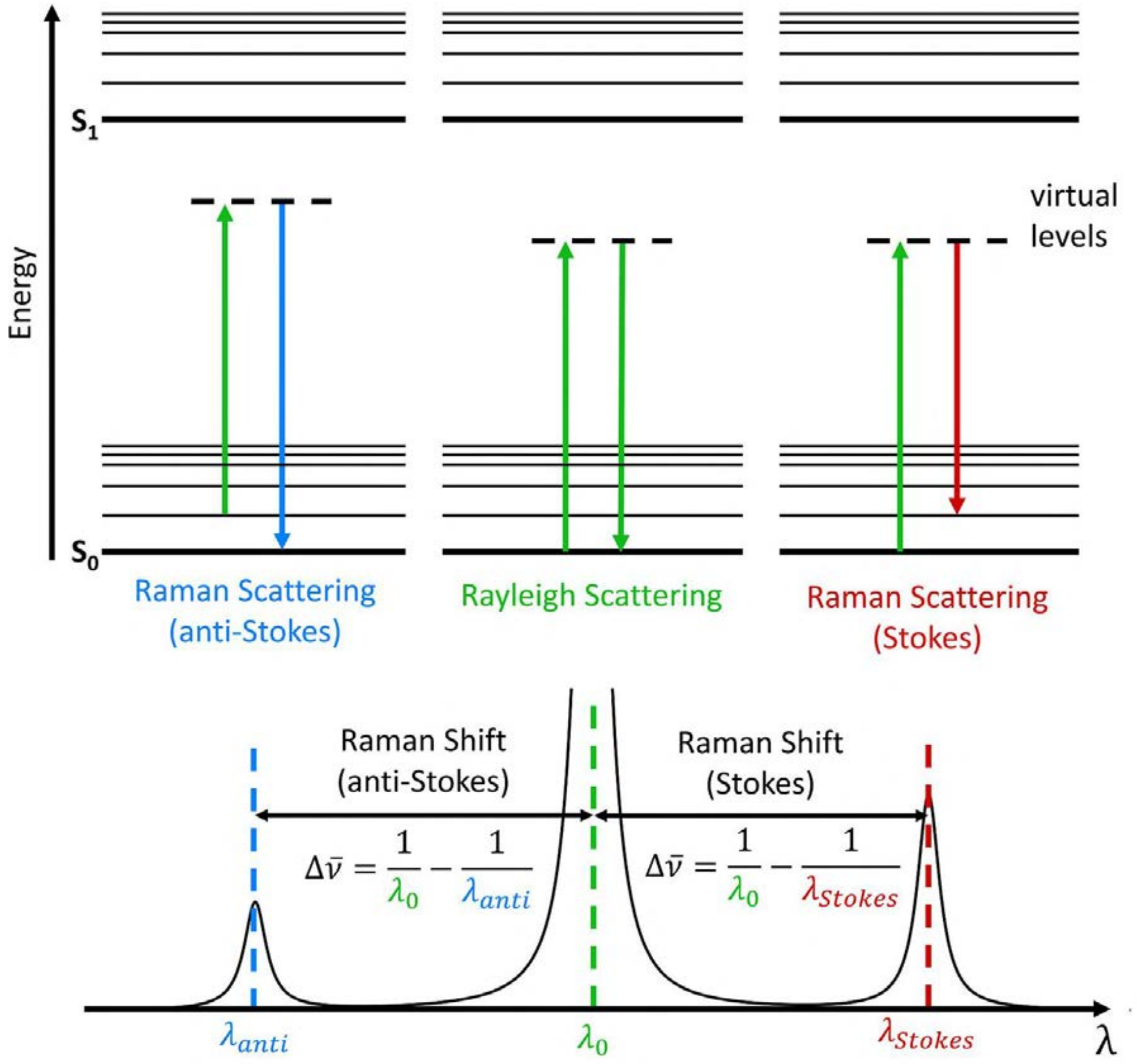

Figure 2.7: *Energy-level diagram showing the states involved in Raman spectra (top) and Raman shift definition (bottom).*

precursor is chosen as equal to the pore volume of the support. Capillary action draws the solution into the pores of the support. A mortar was used to enhance the penetration of the solution into the pores. The catalyst is then dried and calcined, resulting in the evaporation of volatile components and in the deposition of the active metal on the support material. The procedure is repeated for the deposition of the promoter: an aqueous solution containing the promoter precursor is added to the catalyst, which is then dried and calcined. Support materials used are gamma-phase aluminum oxide (Alfa-Aesar, catalyst support), rutile-phase titanium oxide (Alfa Aesar, >99.5%) and monoclinic-phase zirconium oxide (1/8" pellets, Alfa Aesar, catalyst support). Active metal and promoter precursors are respectively copper nitrate trihydrate (Merck, >99.5%) and potassium carbonate anhydrous (Sigma, >99.0%). After the impregnation, catalysts were dried at 80 °C for 16 h and calcined at 500 °C for 5 h. At the end of the preparation, the catalyst is in the form of a granular sand. Synthesised catalysts are reported in Table 2.1. Table 2.2 instead reports the nominal pore volume of the different catalyst supports, according to the documentation retrieved from the supplier. At this point, catalyst grains are ground into a fine powder and pressed under 2 t to obtain a circular pellet. The pellet is crashed into a powder, which is then sieved. The range selected for catalyst particle dimension is 200-300 µm, since it gives a satisfactory trade-off between gas diffusion phenomena and prevention of high pressure drops inside the reactor. Figure 2.8 shows the as-synthesised and the loaded catalyst.

Table 2.1: *Synthesised and tested catalysts.*

$12Cu/Al_2O_3$	$1Cu-20K/Al_2O_3$
$10K/Al_2O_3$	$10Cu-10K/TiO_2$
$11Cu-10K/Al_2O_3$	$10Cu-10K/ZrO_2$
$1Cu-1K/Al_2O_3$	$1Cu-10K/ZrO_2$
$1Cu-10K/Al_2O_3$	

Table 2.2: *Nominal pore volume of the different support materials.*

Catalyst support	**Nominal pore volume** ($mL\,g^{-1}$)
$\gamma-Al_2O_3$	1.0
ZrO_2	0.3
TiO_2	0.5

2.4.2 Modified incipient wetness impregnation catalysts

As it will be discussed in the next chapter, dispersion and distribution of Cu and K species on the support are considered to be crucial for CCR activity. According to this consideration, the synthesis method may play a role since it can influence the dispersion of the active metal and the promoter on the surface. In particular, due to the low amount of water utilised in the incipient wetness impregnation method, this dispersion can be hard to achieve. Especially in the case of K_2CO_3, the solubility in water can be an issue ($1120\,g\,L^{-1}$ at 20 °C). To target this effect, after the activity test of the $11Cu-10K/Al_2O_3$ catalyst synthesised by incipient wetness impregnation, a new batch of the same catalyst was synthesised adding 3 times the amount of water for the K impregnation. To distinguish them throughout the discussion, they will be referred

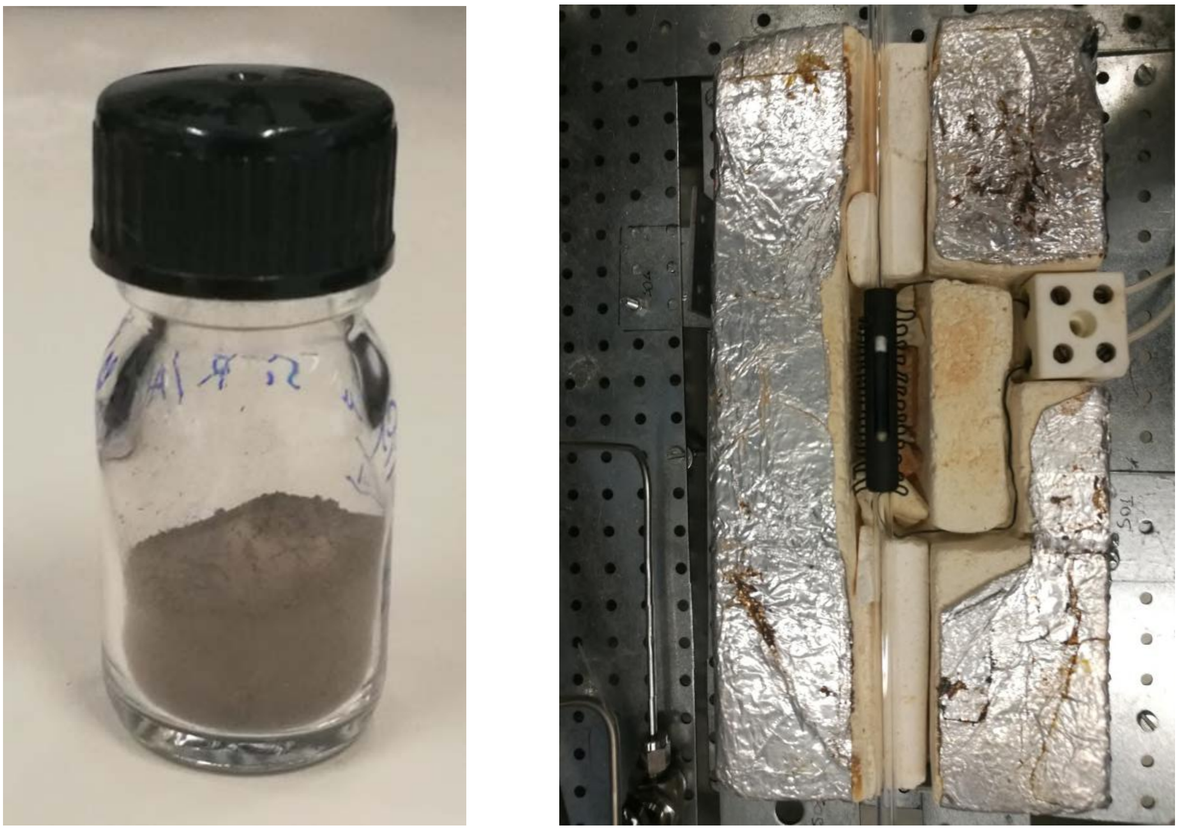

Figure 2.8: *Catalyst powder after calcination (left) and loaded in the reactor tube (right).*

to as $11Cu\text{-}10K/Al_2O_3$ IWI and $11Cu\text{-}10K/Al_2O_3$ IWI-mod. In the same way, a 2 wt% K-promoted $12Cu/Al_2O_3$ was synthesised from the same initial batch. Moreover, in process parameters optimisation presented in Chapter 5, the effect of the amount of water used in the K impregnation step is further addressed.

2.5 Characterisation techniques

2.5.1 X-ray diffraction: Bruker D8 Advance diffractometer

X-ray powder diffraction (XRD) is a analytical technique primarily used for phase identification of crystalline materials and can provide information on unit cell dimensions. The analysed material is finely ground, homogenised, and average bulk composition is determined. X-ray diffraction is based on constructive interference of monochromatic X-rays. X-ray diffractometers consist of three basic elements: a X-ray tube, a sample holder, and an X-ray detector. The X-ray generator and the detector are mounted in two opposite rotating arms. X-rays are generated by the cathode ray tube, filtered to produce monochromatic radiation, collimated to concentrate, and directed toward the sample. The interaction of the incident rays with the sample produces constructive interference when conditions satisfy Bragg's Law ($n\lambda = 2d\sin\theta$). This law relates the wavelength of electromagnetic radiation λ to the diffraction angle θ and the lattice spacing d in a crystalline sample (Figure 2.9). Diffracted X-rays are then detected, processed and counted. By scanning the sample through a range of 2θ angles, achieved by rotating the X-ray source and detector in a specular way, all possible diffraction directions of the lattice should be attained due to the random orientation of the powdered material. Conversion of the diffraction peaks to d-spacings allows identification of the mineral because each mineral has a set of unique d-spacings. Typically, this is achieved by comparison of d-spacings with standard reference patterns. Data were collected using a Bruker D8 Advance Diffractometer equipped with a Bragg-Brentano geometry, with monochromatic Co kα source ($\lambda = 1.7902\,\text{Å}$) in a 2θ range between 5° and 90° at room temperature. The sampling time chosen was 1 h, so as to maximise the signal-to-noise ratio.

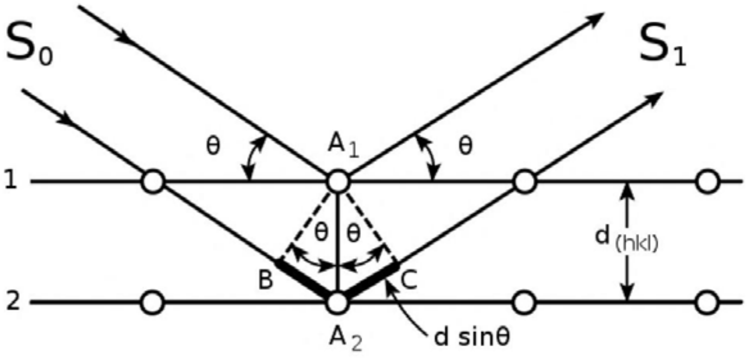

Figure 2.9: *Bragg's diffraction condition construction. The path difference between the two parallel waves is equal to $2dsin\theta$.*

2.5.2 H_2 temperature-programmed reduction

H_2 temperature-programmed reduction (H_2-TPR) is an analytical technique applied in the characterisation of solid materials, and therefore widely used in the field of heterogeneous catalysis. It provides accurate insights into catalyst reducibility and reaction rates in the presence of metal surfaces. In a typical TPR experiment, the catalyst is filled in a fixed bed tube reactor and it is positioned in a furnace. Temperature in the catalyst bed is measured by a thermocouple. A gaseous mixture containing reducing agents such as hydrogen or carbon monoxide is made to flow across the catalyst while gradually increasing temperature. Linear heating allows reduction rate to be correlated with temperature. When reduction is activated at a certain temperature, hydrogen is consumed from the flow. A thermal conductivity detector continuously analyses the difference in thermal conductivity between the gas mixture flowing out from the reactor and a reference flow. Depending on how quickly the flowing gas cools the filaments of the TCD, different amounts of power have to be supplied in order to keep their temperature constant. A gas with higher conductivity removes heat more rapidly, requiring more power to restore the temperature of the filament. In this way, any change in the composition of the gas flowing over the catalyst, strictly related to the interactions between the gas and the catalyst, is recorded as a change in its thermal conductivity. The amount of electricity required to restore the temperature is reported during the analysis. Such analysis was performed in a dedicated set-up, shown in Figure 2.10. It consists of a tubular furnace in which a 6 mm internal diameter quartz tube to hold the sample is inserted. TCD is used as H_2 consumption detector. To perform the experiments, 100 mg of catalyst were mixed with 100 mg of SiC before the tube loading. Temperature was increased from 25 °C to 800 °C with a ramp rate of $10\,°C\,min^{-1}$, whereas the reducing gas atmosphere was composed by 10% H_2 in Ar with a $30\,mL\,min^{-1}$ flow rate. Water produced during the reduction was trapped before reaching the detector. Calibration was made by reduction of a known amount of pure CuO under same experimental conditions.

2.5.3 Branauer-Emmett-Teller surface area: Micromeritics TriStar II 3020

Brunauer-Emmett-Teller analysis was performed to determine the specific surface area of the fresh catalysts. In heterogeneous catalysis, surface area is probably one of the most relevant properties since it has been widely correlated to catalyst activity.[53,54] In fact, usually reaction occurs only on the catalyst surface, while the solid bulk has minor contribution, not being in direct contact with reagents. The BET theory describes the physical adsorption of gas molecules on a solid surface. It is based on a pressure-dependent correlation between the volume of the adsorbed gas and the volume of the adsorbed monolayer. Probing gases used for this analysis are generally non-reactive

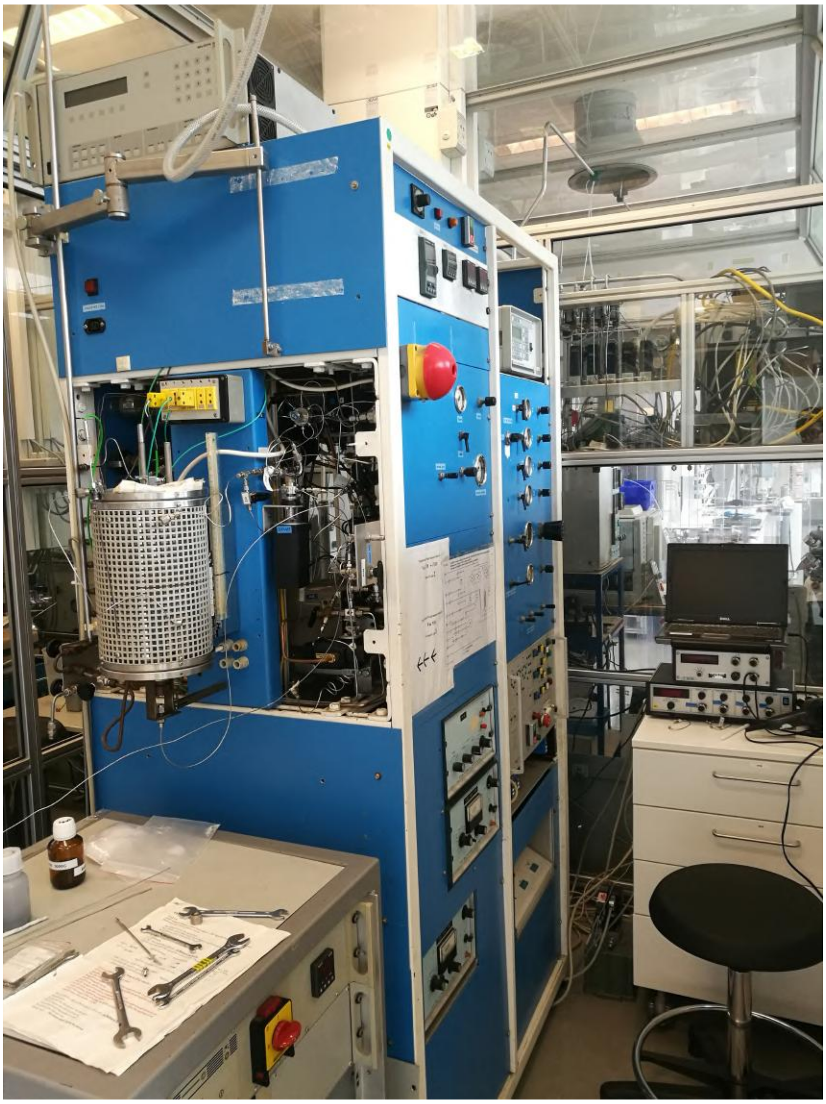

Figure 2.10: *Dedicated experimental setup for temperature programmed analysis.*

gases; nitrogen is the most common, and it is also the one used in this case. A Micromeritics TriStar II 3020 was the instrument used for this analysis. Catalyst samples were first degassed for 15 h at 150 °C and the N_2 adsorption was then performed at 77 K to obtain detectable amounts of adsorption. Known amounts of nitrogen gas are then released stepwise into the sample cell, where partial vacuum conditions are created. After the saturation pressure no more adsorption occurs regardless of any further increase in pressure. After the adsorption layers are formed, the sample is removed from the nitrogen atmosphere and heated to cause the adsorbed nitrogen to be released from the material and quantified. The data collected is displayed in the form of a BET isotherm, which plots the amount of gas adsorbed as a function of the relative pressure. The behaviour of the sample can diverge during adsorption and desorption phases, resulting in a hysteresis of the BET isotherm.

2.5.4 Transmission electron microscopy: JEOL 1400 STEM

Transmission electron microscopy was used to characterise the different catalysts. This microscopy technique is useful to capture nanometer-resolution details of the sample. A transmission electron microscope uses a beam of electrons instead of light, exploiting their wave-particle duality. It is composed by an electron emission source, electromagnetic lenses and an electron detector. The electron beam is produced, accelerated and focused by the lenses on a thin layer of the sample, located in a grid. The beam is modified by passing through the sample, and the transmitted electrons are imprinted in a detector. A digital software can then convert the signal into an image. Thanks to their lower wavelength compared to the visible photons, they allow to overcome the limits of optical microscopy and reach resolution in the order of nm (limit imposed by properties of the optic components). Recent advances in this technology have achieved resolutions below 50 pm for high-resolution TEMs. JEOL 1400 STEM was used for catalyst imaging.

2.5.5 Scanning electron microscopy - Energy dispersive X-ray spectrometry: SEM Hitachi S4800

Scanning electron microscopy was also used for catalysts characterisation. This microscopy technique is adopted to capture information about the morphology and the composition of a sample. Similarly to a transmission electron microscope, it uses a beam of electrons instead of light and it consists of an electron emission source, electromagnetic lenses and an electron detector. The electron beam is produced, accelerated and focused by the lenses on a thick layer of the sample. In turn, it emits secondary electrons, which are then detected. The surface topography of the specimen is determined from the variation of the number of the emitted electrons, and it can be magnified through a digital device. The incident electron beam can also provoke the ionisation of atoms, and the subsequent emission of X-rays. The X-ray energy depends on the elementary composition of the sample, thus it is possible to deduce the chemical nature of the material and its spatial variation by EDS. Best SEMs can achieve resolutions below 1 nm. A Scanning Tunneling Microscope (SEM, model Hitachi S4800) was used to examine the surface and the composition of the catalyst.

Chapter 3

Catalysts characterisation

In this chapter, CCR cataysts are characterised both after calcination and after reaction. The effect of the different active species and of the support materials are investigated by TPR, BET, XRD, TEM and SEM characterisations.

3.1 X-ray diffraction

Ex-situ powder X-ray diffraction patterns were acquired to verify the success of the synthesis of the different samples, with the purpose of obtaining a crystalline structure without undesired phases. XRD patterns were collected for the as-synthesised samples and after several CCR cycles, ending in the CO_2 phase, in order to verify possible modification of the catalyst. Assignment of the crystalline phases was made by search-match analysis based on PDF database.

Figure 3.1 illustrates X-ray diffractograms of the as-synthesised 11Cu-10K/Al_2O_3 IWI and of the 11Cu-10K/Al_2O_3 IWI-mod after calcination, after 6 CCR cycles and after 50 CCR reaction cycles. No evident differences arose from the XRD patterns of the two fresh batches. Main reflexes of CuO tenorite are identified around 41° and 45° for the as-synthesised sample, together with other features ascribable to such crystalline phase (PDF 45-0937). The other reflexes are assigned to the Al_2O_3 support (PDF 48-0367). Potassium is expected to be in the carbonate form due to the precursor utilised for the synthesis and the calcination in air. However, no K_2CO_3 reflexes have been detected before and after reaction. Similar results were obtained by Bansode et al.[55], which pointed out the existence of a highly dispersed K phase in the form of nanocrystallites or thin layers. The high dispersion of K was confirmed also by SEM-EDS analysis (Figure 3.7). In the XRD pattern of the sample after 6 CCR cycles, the coexistence of two different Cu oxidation states is observed, since both CuO reflexes around 41° and peaks at 51° and 59° assigned to metallic Cu are detected (PDF 85-1326). Other small reflexes at 18°, 25°, 31° and 33° are found, but the identification with the database was not successful. However, considering their low intensity and the broad signal, they reflect the presence of an highly dispersed phase. The appearance of a narrow metallic Cu reflex in the XRD, which is stable after reaction, indicates the presence of a sintering phenomenon involving Cu particles. After 50 CCR cycle reaction, besides the pattern features related to the support, peaks at 51° and 59° are detected and assigned to Cu, which is found only in its metallic state. The increase in these peak signals indicates the presence of a sintering phenomenon involving Cu particles.

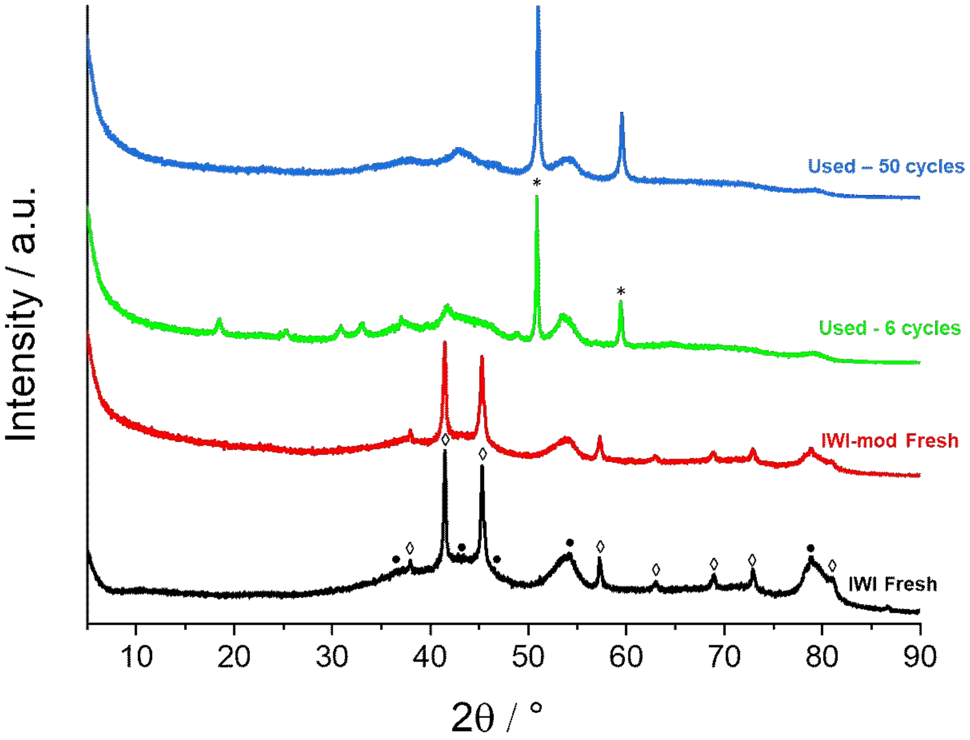

Figure 3.1: *X-ray diffractograms of 11Cu-10K/Al_2O_3 fresh (black line and red line), used after 6 CCR cycles (green line) and after 50 CCR cycles (blue line). Phase identification: γ-Al_2O_3 (●), CuO tenorite (◇), metallic Cu (*).*

Figure 3.2 shows the diffraction patterns for of 10Cu-10K/TiO_2. Reflexes of CuO tenorite (41°, 45°, PDF 45-0937) are identified for the as-synthesised sample. The low-intensity broad reflex at 13° is here assigned to a crystalline K-Ti mixed oxide phase (PDF 41-1100). Other reflexes are assigned to TiO_2 rutile phase (PDF 78-1508). After CCR reaction copper is found only in metallic state (51°, 59°, PDF 85-1326), both after the CO_2 and the H_2 phase. The reflex at 13° is still detected after reaction, indicating the stability of the phase towards reducing treatments. X-ray diffraction analysis for

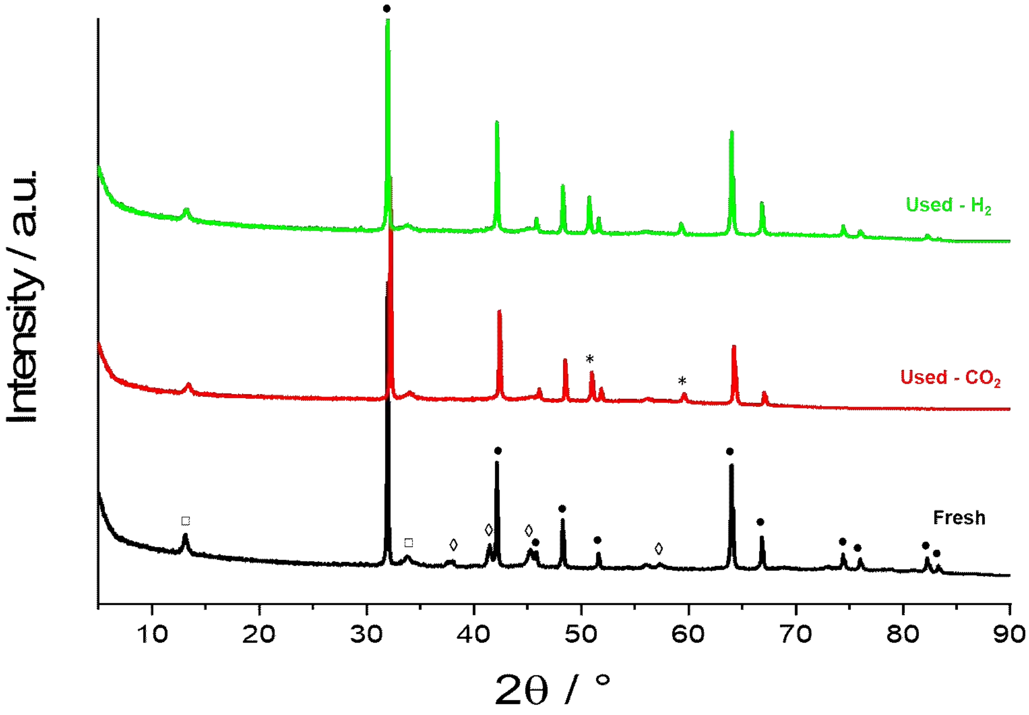

Figure 3.2: *X-ray diffractograms of 10Cu-10K/TiO_2 fresh (black line), used after 6 CCR cycles ended in CO_2 (red line) and after 6 CCR cycles ended in H_2 (green line). Phase identification: TiO_2 rutile (•), CuO tenorite (◇), metallic Cu (*), K-Ti mixed oxide (□).*

the fresh 10Cu-10K/ZrO_2 catalyst is shown in Figure 3.3. CuO reflexes are detected at 41° and 45° (PDF 45-0937). All other reflexes are attributed to the monoclinic ZrO_2 baddeleyte support (PDF 07-0343).

3.2 H_2 Temperature Programmed Reduction

H_2 temperature programmed reduction (TPR) was carried on Al_2O_3-supported samples to investigate the effect of K on the reducibility of the catalysts. Results are shown in Figure 3.4. For the unpromoted catalyst, the complete reduction of Cu(II)

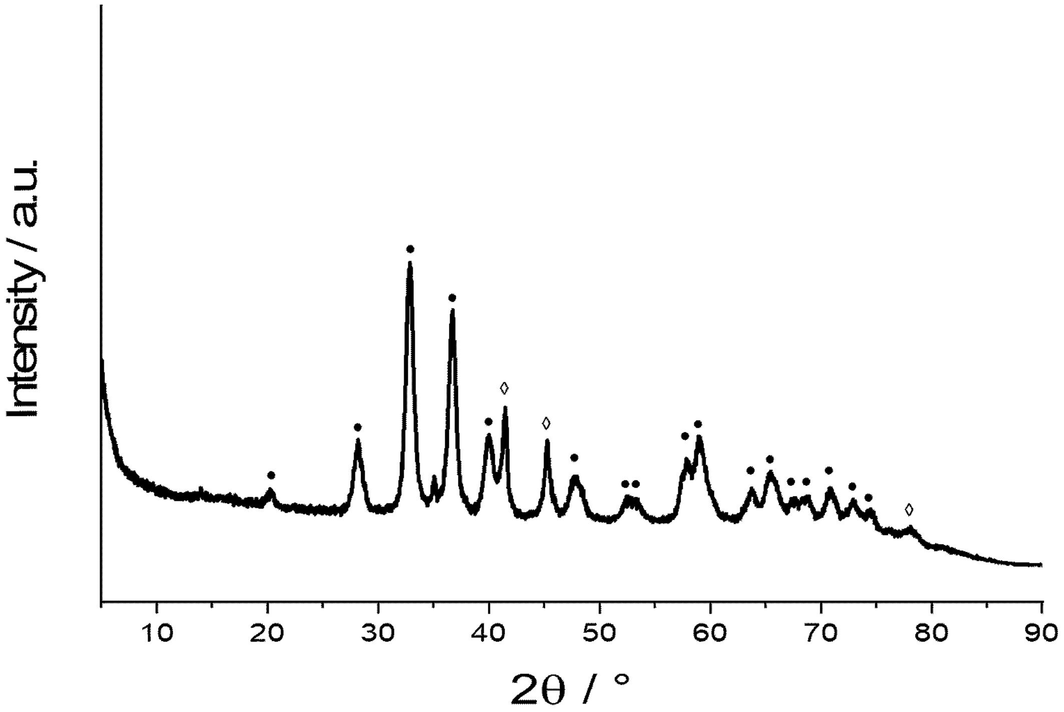

Figure 3.3: *X-ray diffractograms of the fresh 10Cu-10K/ZrO_2. Phase identification: ZrO_2 rutile (●), CuO tenorite (◇), metallic Cu (*).*

to metallic Cu(0) was achieved at 300 °C. The profile presents a main peak at 234 °C with a small shoulder centered at 269 °C. The first one can be assigned to the presence of highly dispersed CuO nanoparticles, while the shoulder can be related to bulk reduction of bigger agglomerates.[56] With the addition of 2 wt.% of K (12Cu-2K/Al_2O_3 sample), a similar reduction profile is obtained with the peak shifting towards higher temperatures (255 °C and 290 °C, respectively). This trend is confirmed and reinforced with 10 wt.% loading, together with a significant change in the reduction profile. Two distinct peaks are found at 278 °C and 332 °C. These results suggest the existence of a strong interaction between K and Cu species, and coverage of Cu surface by K can be responsible of this higher reduction temperature.[57] Moreover, looking at the profile of the 10K/Al_2O_3 catalyst in absence of the active metal, the detected hydrogen consumption starting around 450 °C and peaked at 568 °C was attributed to the decomposition of K_2CO_3 species. However, the decomposition of K_2CO_3 species was activated at much lower temperatures by the presence of Cu in the 11Cu-10K/Al_2O_3 as a continuous H_2 consumption is noticed in the range 370-700 °C, in agreement to previous findings.[28,58]

The support effect was further addressed through H_2-TPR, and reduction profiles are

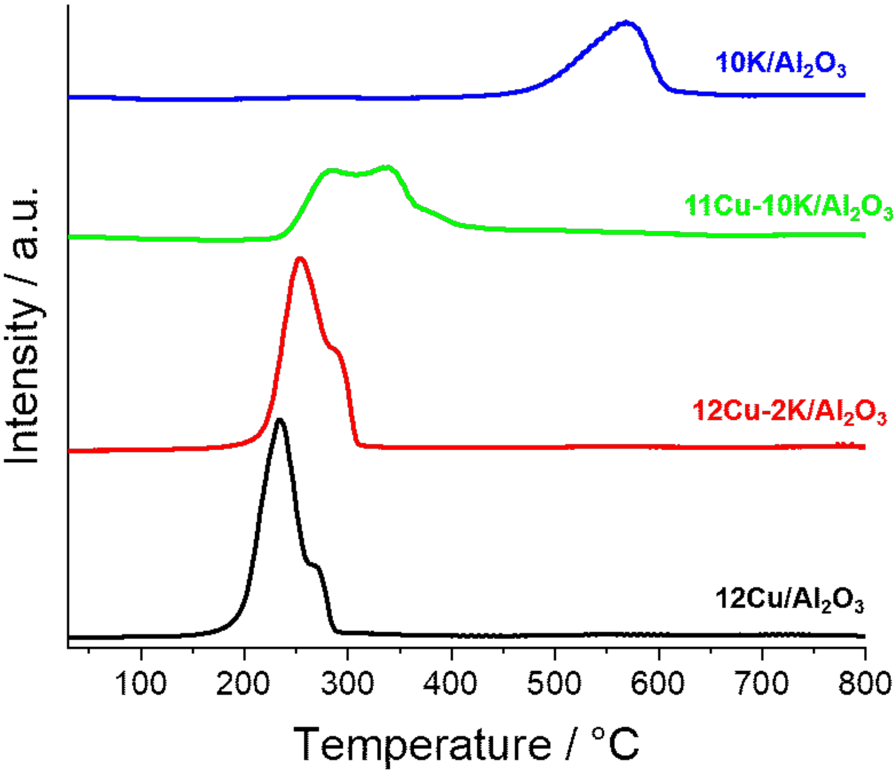

Figure 3.4: *H_2 temperature programmed reduction of Al_2O_3-supported samples with different compositions.*

illustrated in Figure 3.5. Apparently, the effect of the support slightly influences Cu reducibility, as for the ZrO_2- and TiO_2-supported catalysts the main peak is around 315 °C. The ZrO_2-supported catalyst showed also a low-intensity reduction peak at 155 °C ascribed to highly dispersed CuO, since it is more easily reduced as compared with bulk CuO, in accordance with previous studies.[59] The TiO_2-supported catalyst instead presented two additional reduction peaks at high temperature. The first one around 646 °C was attributed to the mixed oxide crystalline phase detected by the XRD analysis, while reduction features above 750 °C were assigned to the reducibility of the support itself.

Figure 3.6 illustrates the H_2-TPR profiles for the two different 11Cu-10K/Al_2O_3 catalysts. Differently from the 1^{st} batch, for the catalyst synthesised through the modified incipient wetness impregnation method a small shoulder at 261 °C is followed by the main peak centered at 324 °C. The broad reduction shoulder in the range 370-700 °C was still detected. This displacement may be an evidence of the higher dispersion of

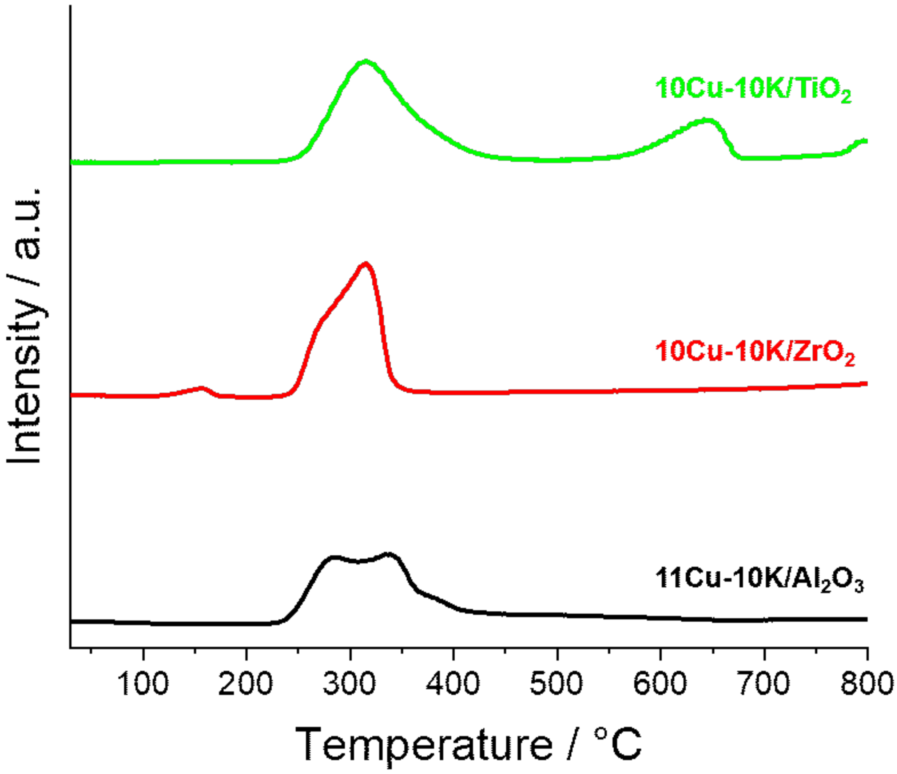

Figure 3.5: *H_2 temperature programmed reduction of 10Cu-10K samples over different supports.*

the active metal entailed with the more diluted solution used for potassium impregnation. In fact, the peak assigned to the reduction of highly dispersed CuO nanoparticles shifted to lower temperatures, as well as the peak attributed to CuO bulk agglomerates.

3.3 BET surface area

Firstly, BET surface area characterisation was carried out for fresh samples of the 12Cu/Al_2O_3 and the 11Cu-10K/Al_2O_3 catalysts to assess the effect of potassium loading. The nominal value of specific surface for γ-Al_2O_3 was 220-280 $m^2\,g^{-1}$. The results obtained for the two catalysts are reported in Table 3.1. The promotion with K strongly affects the surface area of the catalysts: the impregnation of K species is associated to a significant pore blocking of the highly porous support, resulting in a drop of the available BET surface area.[47,49]

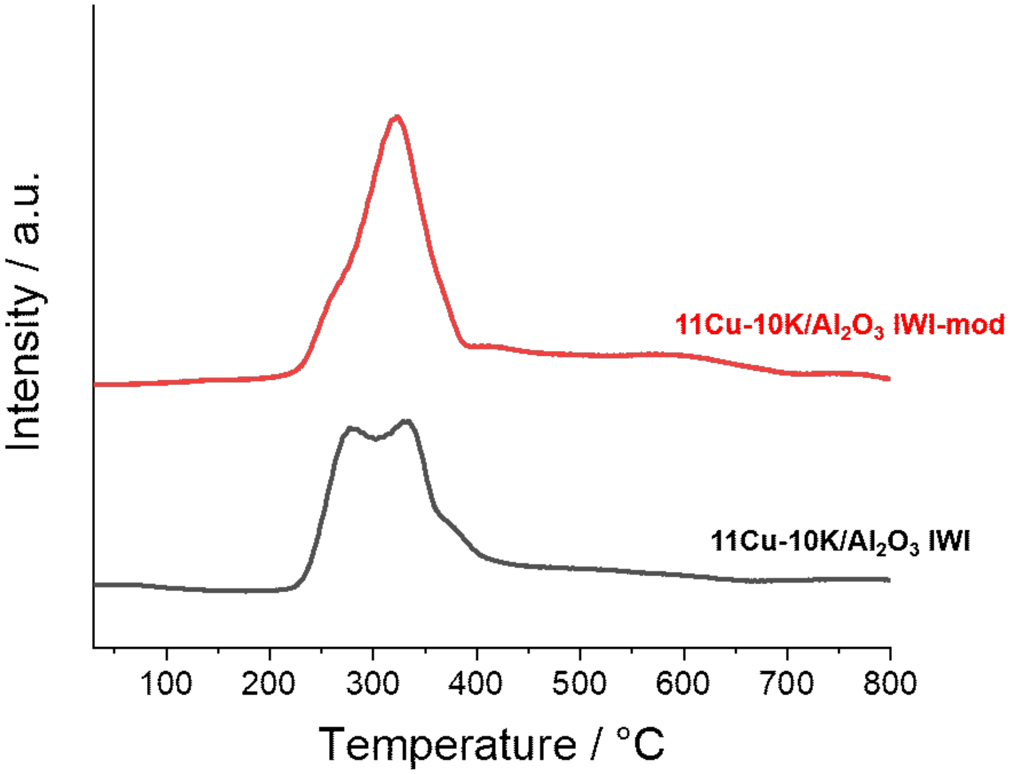

Figure 3.6: *H_2 temperature programmed reduction of the two different batches of the 11Cu-10K/Al_2O_3 catalyst.*

Table 3.1: *BET surface area for Al_2O_3-supported catalysts.*

Catalyst	**BET** ($m^2\,g^{-1}$)
12Cu/Al_2O_3	187.4
11Cu-10K/Al_2O_3	112.6

BET characterisations were performed also for catalysts with similar amount of Cu and K loaded on the different supports. Results are presented in Table 3.2, along with the nominal surface area of the support materials alone according to the supplier documentation. As for the unloaded support materials, the Al_2O_3-supported catalyst showed the highest BET surface area, the TiO_2-supported one assumed the lowest value.

BET surface area of the 11Cu-10K/Al_2O_3 IWI-mod catalyst resulted slightly lower than the one of the 1^{st} batch, being equal to $104.5\,m^2\,g^{-1}$. As a confirmation, the

Table 3.2: *BET surface area for 10Cu-10K samples over different supports.*

Catalyst	**BET support** ($m^2\,g^{-1}$)	**BET** ($m^2\,g^{-1}$)
11Cu-10K/Al_2O_3	250	112.5
10Cu-10K/ZrO_2	90	31.9
10Cu-10K/TiO_2	3.8	2.8

higher dispersion resulted in a lower surface area value, as the pore blocking attained a higher extent.

3.4 SEM-EDS

Scanning electron microscopy with EDS mapping was carried out for fresh samples of both the 11Cu-10K/Al_2O_3 catalysts. No significant difference were found, since species distribution is similar, characterised by highly dispersed K species homogeneously distributed over the support. A tendency to agglomerate is noticed for CuO particles. An example of the EDS imaging is illustrated in Figure 3.7. However, the improved quality of the synthesis reflected also in some minor morphological changes. Figure 3.8 compares the morphology of the two catalysts. Interestingly, while the one synthesised according to the incipient wetness impregnation technique presented irregular structures and agglomerates, the other was characterised by needle structures.

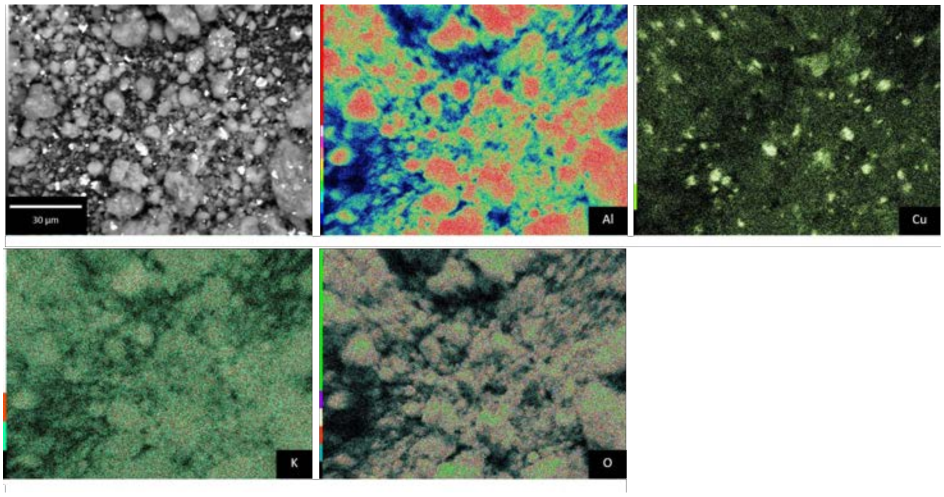

Figure 3.7: *SEM image and EDS mapping of 11Cu-10K/Al_2O_3. Colour scale intensity bar is on the left of the elemental maps.*

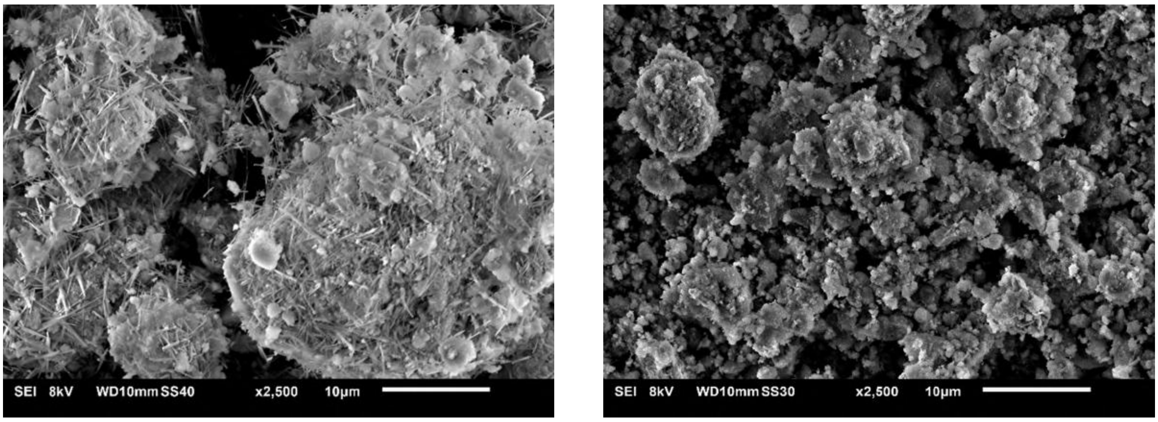

Figure 3.8: *Comparison between the morphology of the 11Cu-10K/Al_2O_3 IWI and the 11Cu-10K/Al_2O_3 IWI-mod catalysts.*

3.5 TEM

Figure 3.9 shows TEM images for the 12Cu/Al_2O_3 and the 10 wt.% K-promoted catalysts after calcination. In both cases small darker particles identified as CuO are visible, and the crystalline rod-like structure of γ-Al_2O_3 is recognisable. The main difference between these two catalysts is the presence of an amorphous-like phase, thus associated with K. Such phase completely covers the alumina support, sometimes forming elongated structures, as the one observed in Figure 3.9(d). Cu particles are small and well dispersed in this matrix, with an average diameter of 6 nm. This morphology is even more evident in the 1Cu-20K/Al_2O_3 catalyst (Figure 3.10), where K phase generates similar structures as in the 11Cu-10K/Al_2O_3, but in a higher extent. TEM images of the unpromoted catalyst after 6 CCR cycles are presented in Figure 3.11. Alumina rods are still evident, while Cu sintered into bigger agglomerates with higher diameter.

Given that TEM imaging of the 11Cu-10K/Al_2O_3 IWI-mod catalyst showed similar features to the 11Cu-10K/Al_2O_3 IWI after calcination, it was utilised for TEM characterisation after reaction. Figure 3.12 shows TEM images of the catalyst after a 6-cycle CCR at 350 °C and after 50 CCR cycles at 450 °C. Both tests were stopped after a CO_2 atmosphere phase. In Figure 3.12(a), the amorphous K-phase is clearly visible and small Cu particles are dispersed in it. Sintered Cu particles are found, in some cases covered by a thin layer (Figure 3.12(b)). TEM images collected after 50 CCR cycles at 450 °C revealed the existence of a particle size duality (Figure 3.12(c), Figure

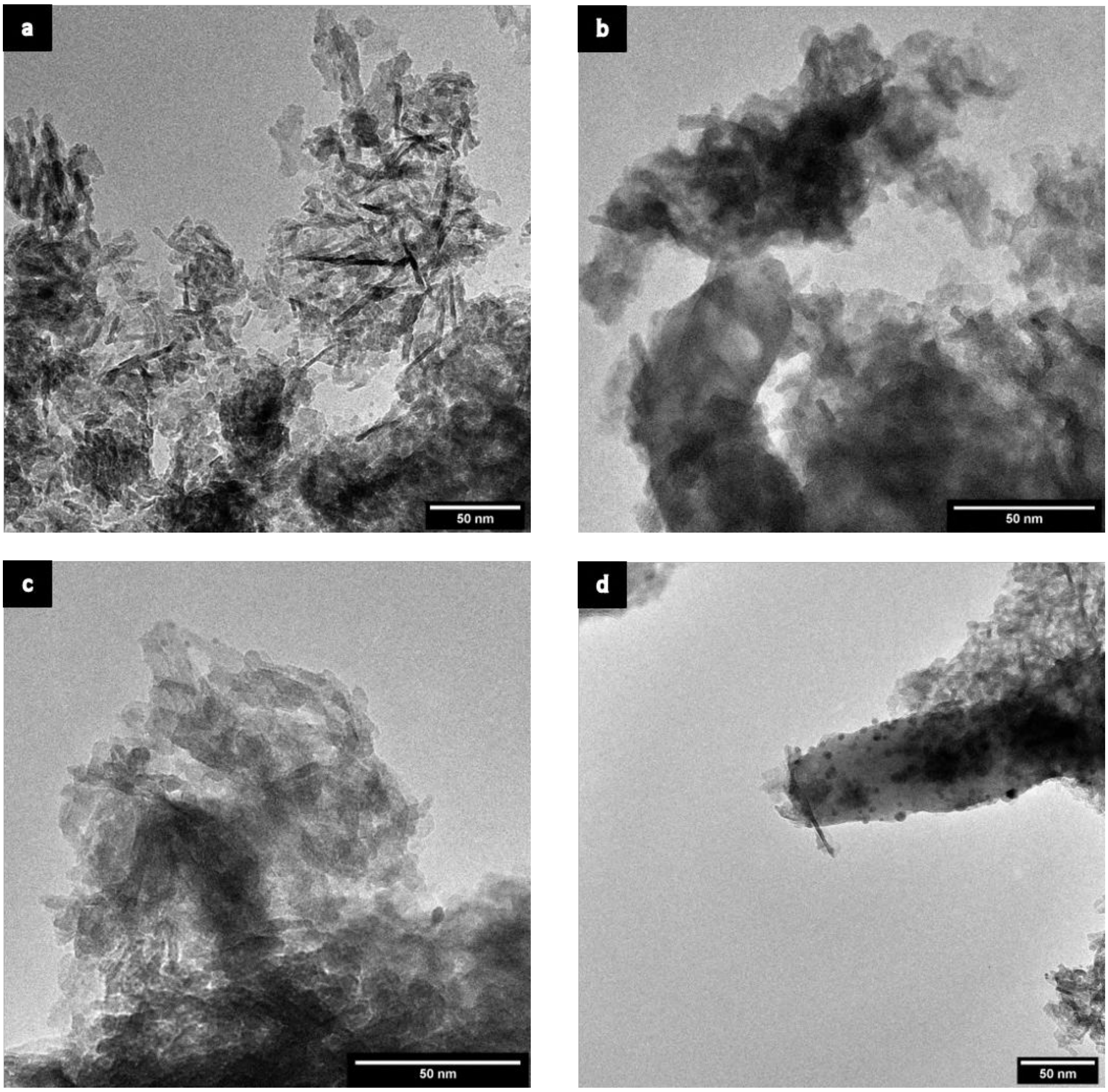

Figure 3.9: *TEM images for (a) 12Cu/Al_2O_3 and (b ,c ,d) 10 wt.% K-promoted catalysts after calcination.*

3.12(d)). On the one hand, sintered Cu particles with a broad size distribution averaged at ca. 39 nm, likely responsible for the appearance of metallic Cu reflexes on XRD pattern previously discussed. On the other hand, small Cu nanoparticles (2-3 nm) dispersed in a mobile and branched potassium phase are formed in reaction condition. Similar behaviour was reported by Luo et al.[56] on a K-promoted Pt/Al_2O_3, for which they related the formation of finely dispersed Pt species under thermal aging to the interaction with an extremely mobile, liquid-like K phase. The high dispersion and the intimate contact between those two phases may play a key role for the activity of the catalyst towards CCR.

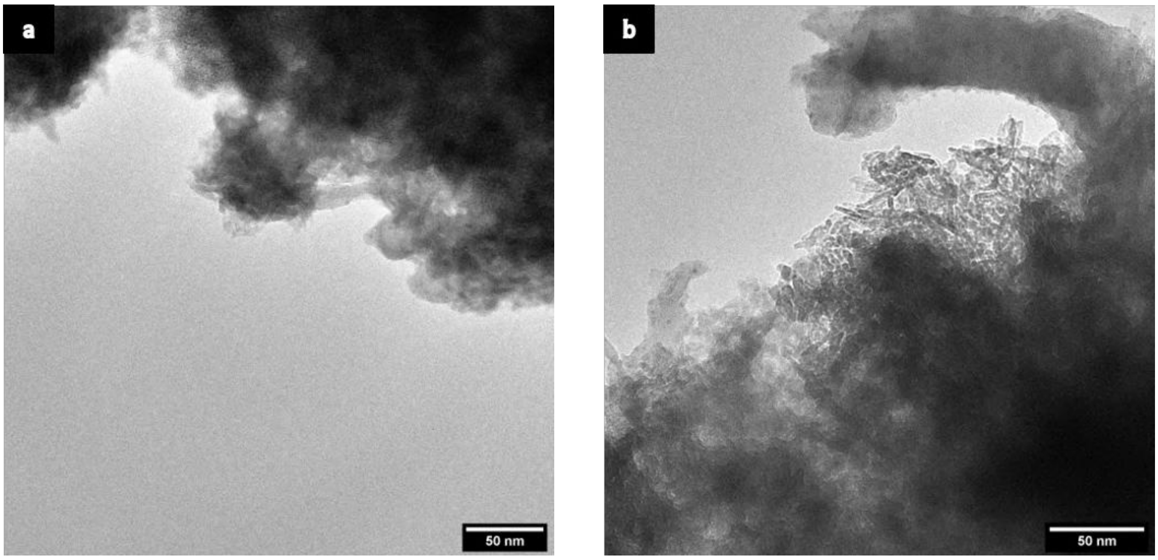

Figure 3.10: *TEM images for the pristine 1Cu-20K/*Al_2O_3.

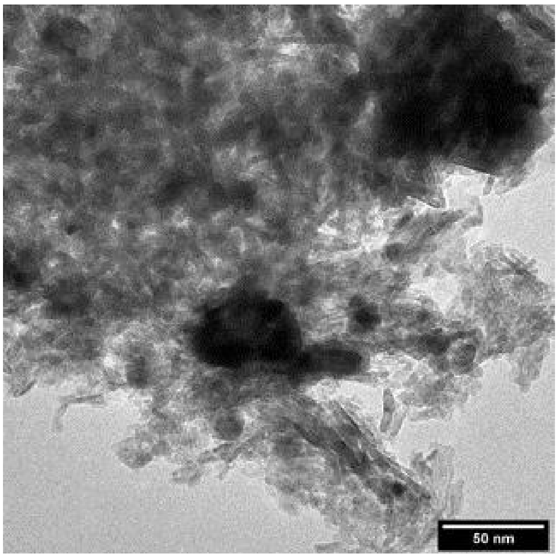

Figure 3.11: *TEM image of the used 12Cu/*Al_2O_3 *after 6 CCR cycles at* 350 °C.

TEM imaging was used also for the characterisation of the 10Cu-10K/ZrO_2 and the 10Cu-10K/TiO_2 catalysts after calcination. Similar observations to the Al_2O_3 supported catalyst can be retrieved: K species appears to cover the catalytic support, and CuO particles are preferentially dispersed in it. Focusing on the TiO_2-supported catalyst, besides the amorphous K phase, a crystalline phase was found, which was still detected after reaction. In fact, equally spaced parallel lines which can be ascribed to the interatomic planes in the crystal structure are evident, as it is illustrated in Figure 3.13. This finding is in accordance with the XRD patterns for this catalyst, where reflexes of a Ti-K mixed oxide phase was visible.

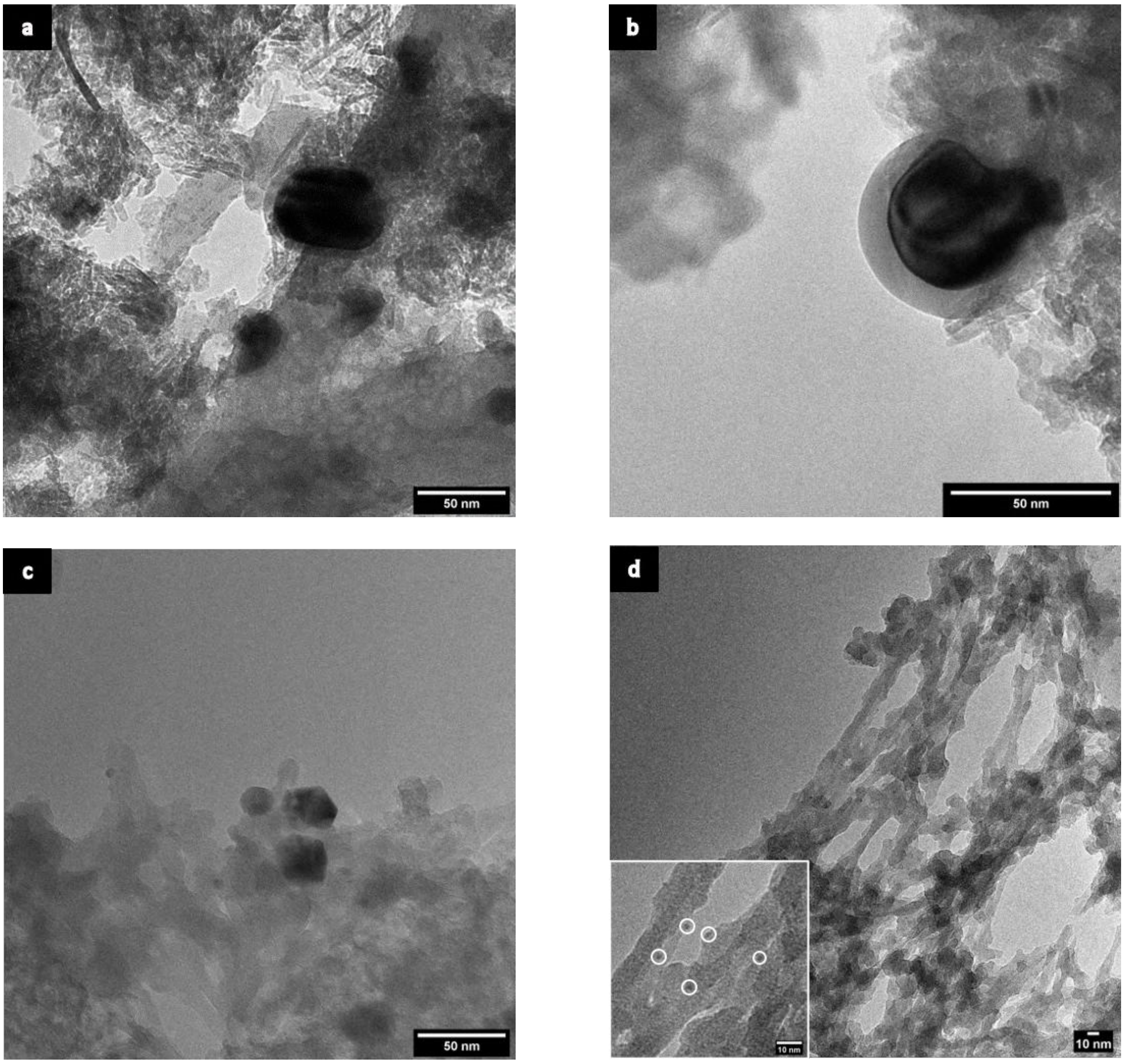

Figure 3.12: *TEM images for the used 11Cu-10K/*Al_2O_3 *(a, b) after 6 CCR cycles and (c, d) after 50 CCR cycles.*

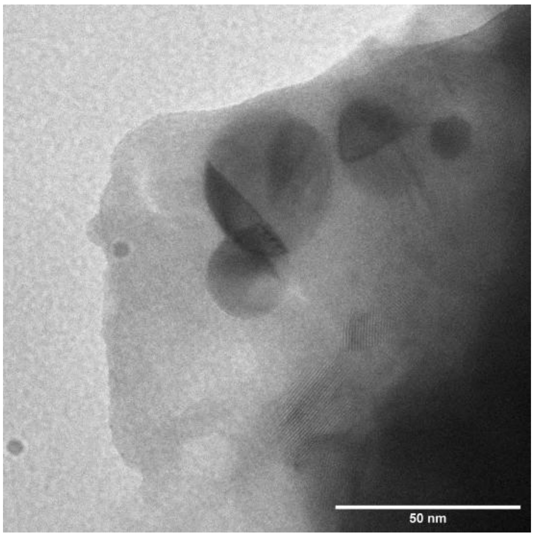

Figure 3.13: *TEM images for the used 10Cu-10K/*TiO_2*, where interatomic planes of the crystalline structure are visible.*

Chapter 4

Catalytic activity and insights in the CO_2 capture mechanism

Unsteady-state experiments have been designed with the aim of investigating the CCR catalytic activity of the catalysts under study. The instrumentation has been described previously in Chapter 2.

200 mg of catalyst were weighted and placed into the quartz tube, using quartz wool to pack it. The catalytic bed temperature was raised to 450 °C with a ramp rate of 30 $°C\,min^{-1}$ under a 25 vol.% O_2 in He atmosphere for the complete oxidation of possible impurities. It was then pre-reduced at this temperature under 50 $mL\,min^{-1}$ of pure H_2 for 1 h. The reaction temperature was then set to the desired value to get insights on the reaction behaviour. Catalytic tests were conducted at ambient pressure. A gas mixture of 9.9 vol.% CO_2 in He, referred to as capture phase, was alternated to a reduction phase consisting of a pure H_2 flow. The flow rates were controlled by MFCs, previously calibrated with a flowmeter. The calibration of the MFCs led to an uncertainty in the measurement of 0.1 $mL\,min^{-1}$. Both the CO_2 and H_2 phases lasted 7 min, even if the effective capture and reduction processes were much shorter. The choice of extended phase duration was made in order to increase the resolution on the underlying chemical processes and to better highlight the differences among the catalysts. An inert phase of pure He was flushed between oxidising and reducing phases (and vice versa). From an experimental point of view, this flushing phase was found convenient to provide sufficient stabilisation of the signal, complete separation of the

two phases, and removal of physisorbed species. Catalytic activity data were generally obtained from the averaging of 4 cycles after a reproducible composition of the effluent was achieved. Considering the CO_2 conversion, the selectivity towards CO was always greater than 99%. No C-containing side products were detected in the outlet. In particular, CH_4 signal was not distinguishable from the baseline noise, and no formation has been detected during the reactions performed.

A series of blank tests were executed applying CCR gas cycling (3 cycles) at room temperature after loading the reactor with the catalyst. They resulted in the absence of CO and CH_4 IR signals. The total amount of CO_2 fed to the reactor was determined from these tests and was used for calculations. Moreover, the time instant of CO_2 signal appearance in these tests was used as reference to evaluate the interval of initial full CO_2 capture, accounting in this way for delays on the signal detection generated by the packed bed configuration.

4.1 The 11Cu-10K/Al_2O_3 catalyst

The first catalyst synthesised and tested was the 11Cu-10K/Al_2O_3 IWI catalyst, in order to possibly reproduce and verify results obtained by Hyakutake et al.[29] Figure 4.1 shows the concentration profiles of CO_2 and CO obtained for the 11Cu-10K/Al_2O_3 catalyst when exposed to CCR conditions. In this experiment, the flow rates were $25\,\mathrm{mL\,min^{-1}}$ for the CO_2 phase and $50\,\mathrm{mL\,min^{-1}}$ for the H_2 phase. The temperature of the catalytic bed was maintained at 350 °C after the pre-treatment steps. For sake of clearness, different phases are indicated by different colors: the oxidising phase is indicated by the blue region, whereas the green region indicates the reducing phase. Between CO_2 and H_2 phase (and vice versa), the catalyst was flushed with He at $80\,\mathrm{mL\,min^{-1}}$ for 150 s. This catalyst was active for CCR reaction, as it showed the desired features. In the first 20 s, CO_2 was almost completely captured from the inlet stream. No CO signal is detected in this time interval, allowing for a CO_x-free reactor effluent. By switching to H_2, the captured species were reversibly eliminated in the form of CO, regenerating the catalyst for the following cycles. The CO_2 signal after the full capture period raised slower with respect to the signal obtained in the blank test. Here a combined contribution was expected: on the one hand, the capture of CO_2 was still taking place until complete depletion of the active sites, on the other hand part of the CO_2 was expected to be consumed by Cu oxidation. The last phenomenon was confirmed by the detection of the CO signal during the oxidising phase, as found also by Hyakutake et al.[29] at this temperature. When switching to the H_2 phase, the captured CO_2 was reduced to CO with high selectivity, with no CH_4 detection. From a process point of view, a mixture of H_2 and CO was obtained in the outlet stream. However, water and excess H_2 separation in the product mixture was required for a suitable utilisation as syngas.

By limiting the capture phase duration to the full capture interval, CCR efficiency was strongly enhanced, as almost all CO_2 could be reversibly trapped and converted. Nevertheless, as reported in a previous work, a major issue of this catalytic system is the slow reduction kinetics,[29] since the time interval required for the complete evolution of CO during the reducing phase is much longer than the full capture interval. Such behaviour is not favorable for process synchronisation.

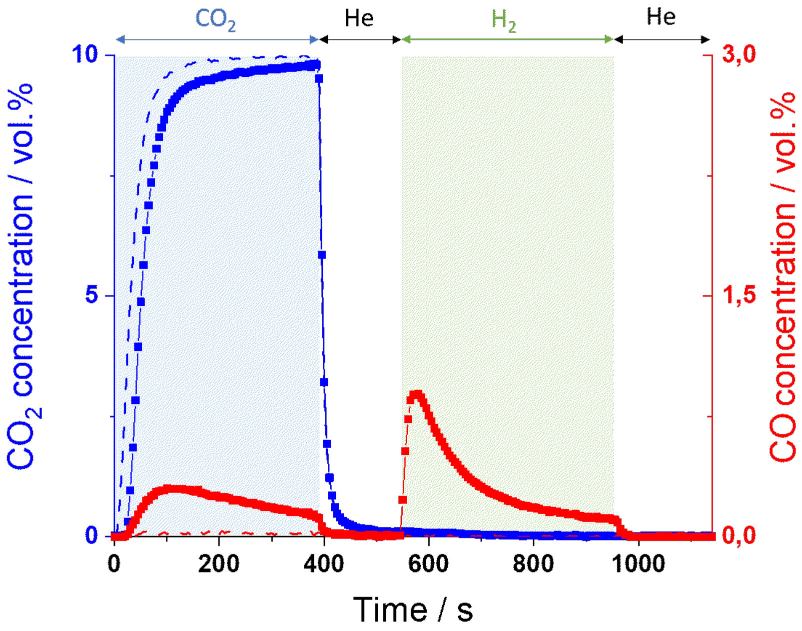

Figure 4.1: *Average concentration profiles of CO_2 and CO during CCR operation at 350 °C. Alternation of 9.9% CO_2 in He (in blue) at 25 mL min^{-1} and 100% H_2 (in green) at 50 mL min^{-1}. Blank profile (dashed line) and reaction profile (K-promoted Cu/Al_2O_3, solid line). Pure He at 80 mL min^{-1} is interposed between oxidising and reducing pulses.*

Considering the unpromoted 12Cu/Al_2O_3 catalyst, no initial full capture was observed. Concentration profiles of CO_2 and CO obtained from its catalytic testing are shown in Figure 4.2. The 12Cu/Al_2O_3 catalyst did not show any CCR activity: during the CO_2 phase, CO signal was immediately detected, indicating that, in absence of potassium, CO_2 was directly reduced to CO due to Cu oxidation. Thus, potassium is expected to play a major role in promoting CO_2 capture.

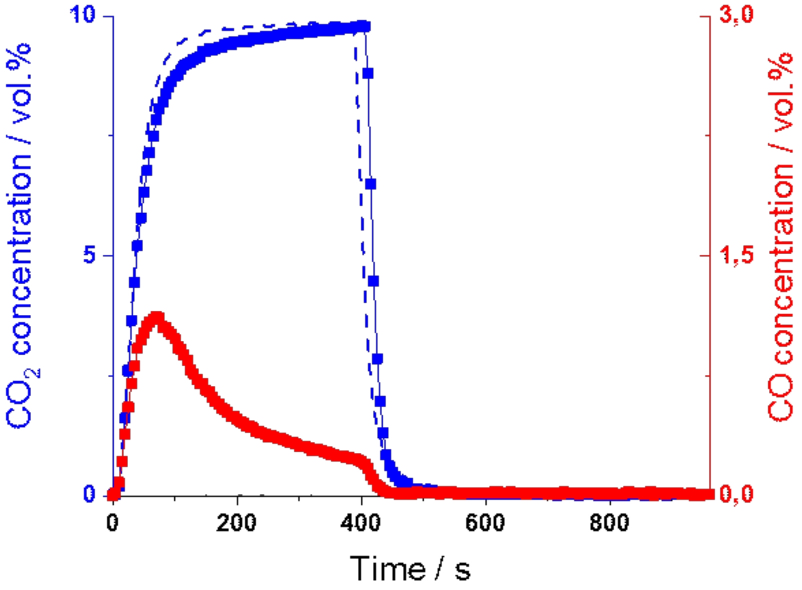

Figure 4.2: *Average concentration profiles of CO_2 and CO during CCR operation at* 350 °C. *Alternation of 9.9% CO_2 in He at* 25 mL min^{-1} *and 100% H_2 at* 50 mL min^{-1}. *Blank profile (dashed line) and reaction profile (12Cu/Al_2O_3, solid line). Pure He at* 50 mL min^{-1} *is interposed between oxidising and reducing pulses.*

4.2 Insights in the capture mechanism

As introduced before, potassium is fundamental to develop the CO_2 capture ability. In absence of K, no CO_2 capture was activated. The unpromoted 12Cu/Al_2O_3 catalysts showed dominant formation of CO during the CO_2 phase (Figure 4.2), in agreement with previous results[29] and related to Cu oxidation by CO_2. In presence of K (11Cu-10K/Al_2O_3, Figure 4.1), full capture was activated at the beginning of the CO_2 phase. Interestingly, no CO was detected in this interval. Compared to the unpromoted catalyst (Figure 4.2), the formation of CO was sensed only at the end of the full capture period, when also CO_2 signal started to rise. This delay in the evolution of CO from the sample was found for catalysts showing substantial CCR activity, but it is independent on the K loading. To explain this behaviour, the involvement of CO in the capture process has been considered. To prove this, we performed a CO adsorption test on the 11Cu-10K/Al_2O_3 catalyst, by substituting CO_2 with CO in a typical CCR experiment at 350 °C. CO concentration profiles are reported in Figure 4.3 For this test, 25 mL min^{-1} of 3.8% of CO in He were fed to the reactor. In analogy with the CCR tests, the delayed detection of the CO signal with respect to the blank indicates the strong interaction with the catalysts and the involvement of CO in the capture process. In normal CCR operation then, CO deriving from Cu oxidation is expected to be simultaneously chemisorbed until saturation of the active sites for capture. After that, both CO_2 and CO are detected at the outlet.

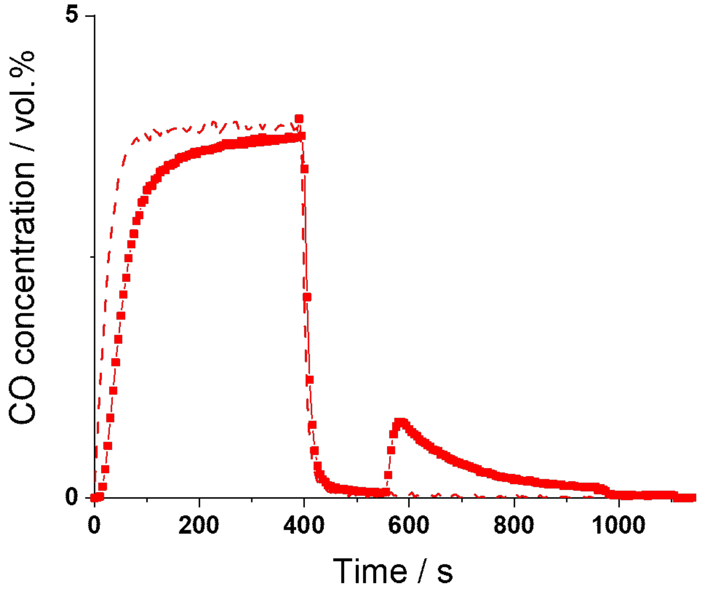

Figure 4.3: *Average concentration profile of CO during CCR operation with substitution of CO_2 flow with 3.8% CO in He at 25 mL min^{-1} on 10% K-promoted 11 wt.% Cu/Al_2O_3 at RT (dashed line) and at 350 °C (solid line). Pure He at 80 mL min^{-1} is interposed between oxidising and reducing gas atmospheres. Test performed after reduction in H_2 at 450 °C.*

4.3 Effect of the support

The type of metal oxides used as the catalyst support can drastically alter the CO_2 capture activity due to their properties. In this work, the effect of surface area, porosity and interaction with the active species for CCR are addressed. Among the other properties, also acidity[60,61] and hydrophilicity may affect catalyst activity due to the different interaction strength and modes with CO_2.[62]

To evaluate the influence of the support material, 10 wt.% K-promoted 10 wt.% Cu catalysts were prepared substituting Al_2O_3 with TiO_2 and ZrO_2 (10Cu-10K/TiO_2, 10Cu-10K/ZrO_2). The CCR results of 10Cu-10K/TiO_2 and 10Cu-10K/ZrO_2 catalysts are reported in Figure 4.4. The three catalysts showed different CCR activities. The capture efficiency followed the trend $Al_2O_3 > ZrO_2 >> TiO_2$, which is also reflected in the amount of CO evolved in the reducing phase. In the case of TiO_2 as support, no activity in CO_2 capture was noticed. Looking at the BET characterisation results illustrated in Table 3.2, Al_2O_3 provides the highest surface area. Comparing different supports for RWGS, Jurkovic et al.[42] found high dispersion of Cu on Al_2O_3 and ZrO_2 on catalysts prepared by deposition precipitation method, with Cu/Al_2O_3 exhibiting the highest catalytic activity. This is in accordance with BET results, where Al_2O_3 supported catalyst exhibited the highest surface area. The use of Al_2O_3 as support markedly enhanced the activity for CCR since its high surface area provided adequate dispersion of the Cu nanoparticles and maximised the contact between Cu and K phases, as confirmed by SEM-EDS mapping (Figure 3.7). These observations may also explain the poor activity of the TiO_2-supported catalyst. In fact, besides the very low surface area, in the XRD of the 10Cu-10K/TiO_2 sample (Figure 3.2), a low intensity broad reflex at 13° is present both in the fresh and used catalyst powders. This reflex has been assigned to a K-Ti mixed oxide phase. Being confined in a crystalline phase, K would be prevented from interacting with the Cu sites to form the active phase for reversible CO_2 capture.

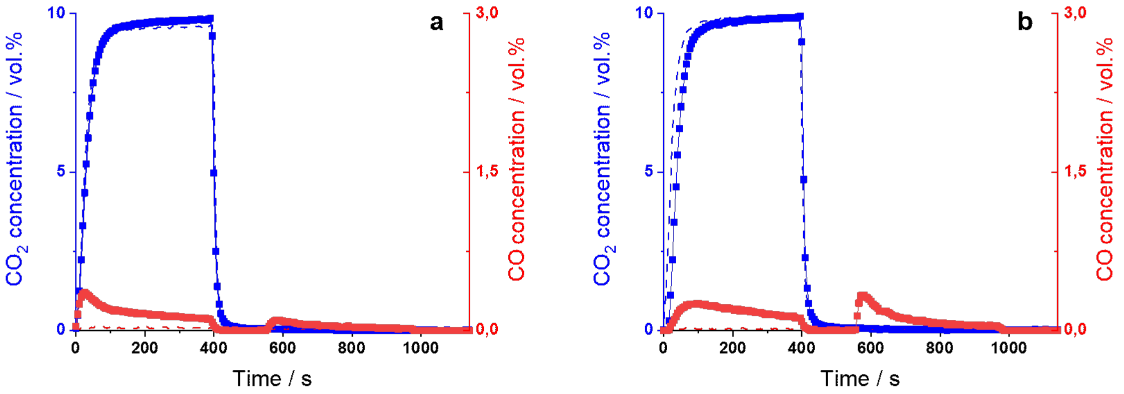

Figure 4.4: *CCR activity at* 350 °C *for a) 10Cu-10K/TiO$_2$ and b) 10Cu-10K/ZrO$_2$ catalysts.*

4.4 Effect of synthesis conditions

Given that dispersion of the active species may be crucial in determining catalyst activity, the synthesis of a new 11Cu-10K/Al$_2$O$_3$ catalyst with modified synthesis conditions was performed, as described in Section 2.4. Its characterisation is then presented in Chapter 3. Figure 4.5 illustrates the concentration profiles of CO$_2$ and CO obtained for the 11Cu-10K/Al$_2$O$_3$ IWI-mod catalyst when exposed to CCR conditions at 350 °C. For this test, slightly different conditions were utilised for the inert flush phase the oxidising and reducing pulses. For the purpose of comparing with the previous results, no relevant changes are expected in the catalytic activity. More precisely, He was flushed at 50 mL min^{-1} for 1 min. Surprisingly, CCR activity was highly improved if compared to the one obtained for the same catalytic system synthesised through the rigorous incipient wetness impregnation method (Figure 4.1). Indeed, the initial CO$_2$ full capture period was more than doubled, since in the first 45 s CO$_2$ was almost completely reversibly adsorbed on the catalyst as a surface species. As before, no CO signal was detected in this time interval allowing for a CO$_x$-free reactor effluent, and after the switching to the H$_2$ phase CO$_2$ is reduced to CO, with no other C-containing side products detected. CO evolved during the reducing phase was 1.70 mL, thus obtaining a significantly CO-richer product effluent (1.10 mL for the 11Cu-10K/Al$_2$O$_3$ IWI catalyst).

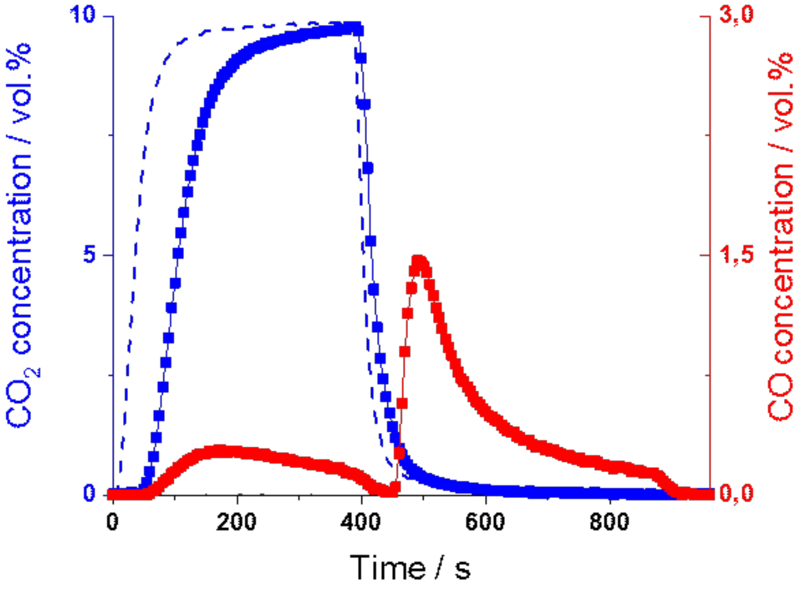

Figure 4.5: *Average concentration profiles of CO_2 and CO during CCR operation at* 350 °C *for the modified IWI 11Cu-10K/Al_2O_3 catalyst. Alternation of 9.9% CO_2 in He phase at* 25 mL min^{-1} *and 100% H_2 at* 50 mL min^{-1}*. Blank profile (dashed line) and reaction profile (K-promoted Cu/Al_2O_3, solid line). Pure He at* 50 mL min^{-1} *is interposed between oxidising and reducing pulses.*

4.5 Effect of K loading

In a previous work, Hyakutake et al.[29] pointed out the peculiar action of K promotion with respect to other alkali metals in the CCR process. They attributed the peculiar CCR activity of the 11Cu-10K/Al_2O_3 catalyst to the dynamic contact between the amorphous K phase and Cu nanoparticles highly dispersed in it. Similar findings of an extremely mobile, liquid-like K phase with highly dispersed Pt nanoparticles were reported for NO_x storage activity by Luo et al.[56]. Here, the effect of K loading on CCR activity is addressed comparing the performances of two sets of catalysts with increasing K loading. The first set is composed of three 1Cu/Al_2O_3 catalysts promoted with 1, 10 and 20 wt.% K respectively. The second set is made up of the unpromoted 12Cu/Al_2O_3 and its promoted counterparts containing 2 wt.% and 10 wt.% K. To be remarked, the first set was synthesised with the standard incipient wetness impregnation method, while the second with the modified method.

Catalytic activities of K-promoted 1Cu/Al_2O_3 catalysts are illustrated in Figure 4.6. As already pointed out, K species were found to be fundamental for promoting CCR activity. As a confirmation, an increase in the potassium loading involved a higher CO_2 capture and a subsequent higher CO evolution during the reducing phase. The 1 wt.% K-promoted catalyst did not show any CCR catalyst properties: during the CO_2 phase, CO signal was immediately detected, in analogy with the unpromoted samples where CO_2 passing through the reactor oxidised Cu and immediately produced CO at the outlet. By increasing the K loading to 10 wt.%, the CO_2 uptake increased and its subsequent conversion to CO was ensured when switching to the reducing phase. The 10 wt.% K-promoted catalyst showed 20 s full capture, and all chemically stored CO_2 was then converted to CO after the switching to the H_2 phase. However, an optimum K loading exists, as a further increase in the loading of the promoter did not enhance CO_2 capture. In fact, for the 1Cu-20K/Al_2O_3 catalyst, no full CO_2 uptake was observed. The low CO evolution after the switching to the reducing atmosphere was mainly attributed to carbonates decomposition. Looking at the catalytic activity of a 10K/Al_2O_3 catalyst, a continuous release of CO during the H_2 phase was found, as shown in Figure 4.7(b). In absence of Cu, strong K_2CO_3 species were formed, which were difficult to remove in H_2 at reaction temperature. Besides, their formation was responsible for the longer capture noticed at the first CCR cycle for all the catalysts. The presence of Cu then contributed to enhance the decomposition of K_2CO_3 species, lowering the temperature needed for the process. Similar findings were reported by Bobadilla et al.[28], who observed the drop in decomposition temperature of K_2CO_3 in the form of large bulk crystallites from 890 °C to ca. 200–300 °C, likely due to enhanced surface carbonates composition over a FeCrCu-K hydrotalcite-supported catalyst.

Looking into the CO profiles of the 1 wt.% 10 wt.% K-promoted catalysts, the CO signal intensity associated with Cu oxidation detected during CO_2 phase decreased with the K-loading increase. The loading of K controlled also the amount of CO formed during the capture phase, which was related to Cu oxidation. Interestingly, the CO signals during the CO_2 phase for these three catalysts displayed different behaviours. As shown in Figure 4.8, the volume of CO evolved in the CO_2 phase dropped at higher K-loadings. This effect was even more pronounced for the 20 wt.% promoted 1Cu/Al_2O_3. Figure 4.9 reports the volumetric amount of CO evolved during the CO_2 phase, which decreased at higher K loadings. Also, for 20 wt.% K-promoted catalyst the reduction during H_2 phase was more limited. Such two phenomena will be in agreement with the reported encapsulation and covering of Cu particles by K species.[56,46] When in large amounts, the potassium species can cover the Cu particles and reduce the availability of Cu sites which are active both for CO_2 oxidation and H_2 dissociation.

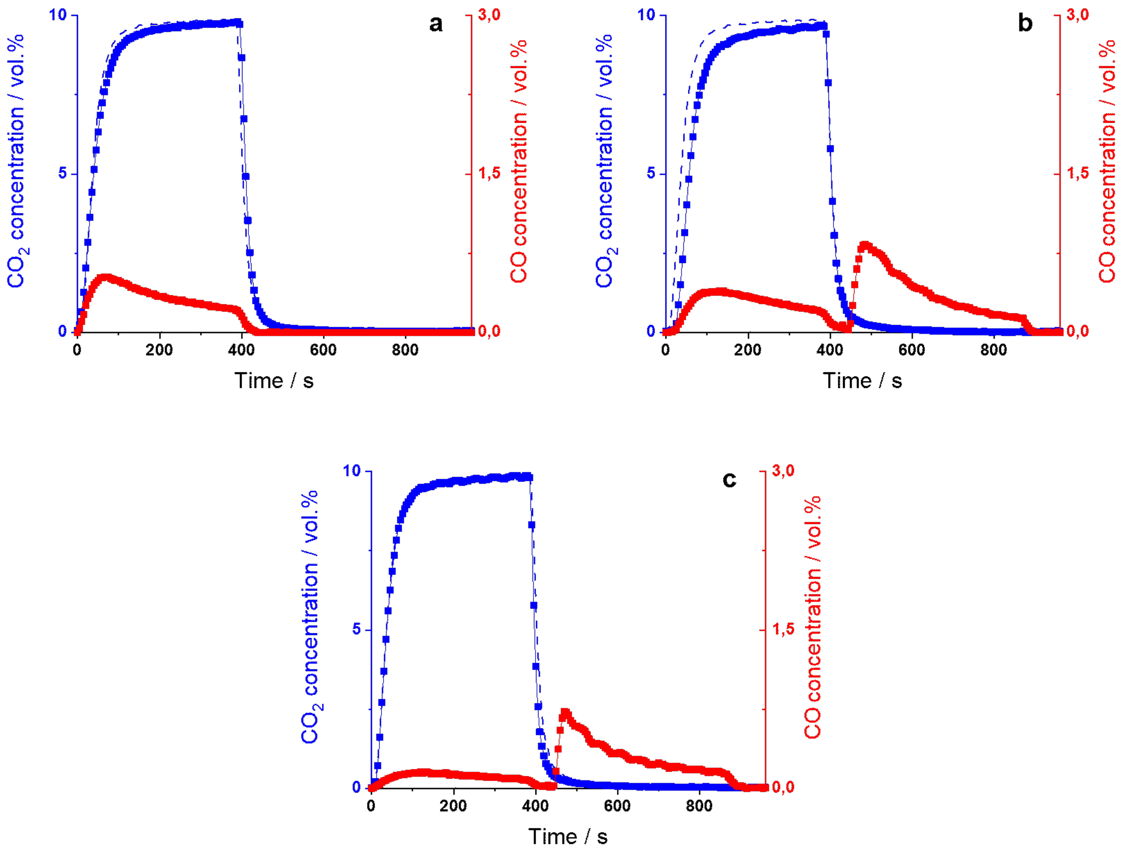

Figure 4.6: *Average concentration profiles of CO_2 and CO during CCR operation at* 350 °C *with 9.9% CO_2 in He at* $25\,\mathrm{mL\,min^{-1}}$ *vs. 100% H_2 at* $50\,\mathrm{mL\,min^{-1}}$ *at atmospheric pressure over K-promoted 1 wt.% Cu/Al_2O_3 with increasing K concentration, (a) 1%, (b) 10% and (c) 20%. Pure He at* $50\,\mathrm{mL\,min^{-1}}$ *is flushed between oxidising and reducing gas atmospheres.*

The second set of catalysts was prepared starting from a 12 wt.% Cu on Al_2O_3. From this batch, two different catalysts were prepared with increasing addition of K to obtain a final composition of 12 wt.% Cu, 2wt.% K and 11 wt.% Cu, 10wt.% K. CCR activity was then investigated using the same experimental parameters as before. Concentration profiles of CO_2 and CO are shown in Figure 4.9. As expected for the unpromoted

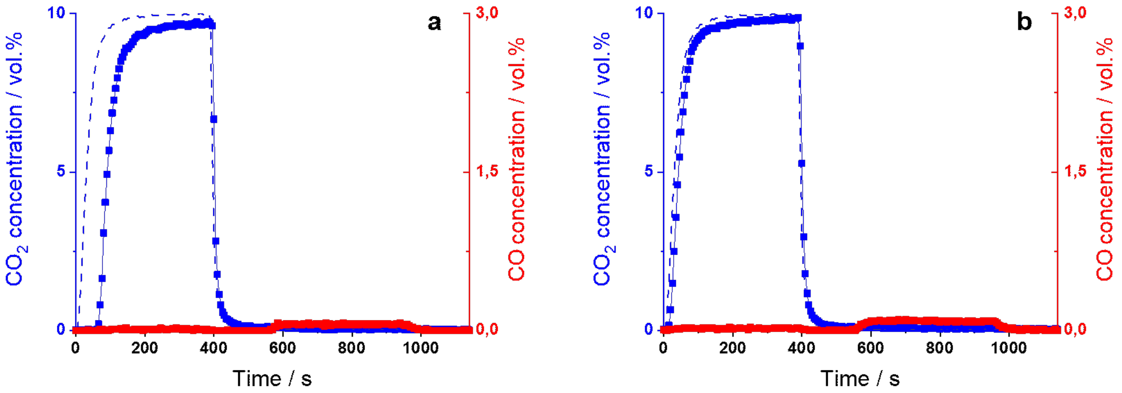

Figure 4.7: *Concentration profiles of CO_2 and CO during CCR operation at 50 °C with 9.9% CO_2 in He at 25 mL min^{-1} vs. 100% H_2 at 50 mL min^{-1} at atmospheric pressure over the 10K/Al_2O_3 during a) the 1^st cycle and b) averaged on the following ones. Pure He at 80 mL min^{-1} is flushed between oxidising and reducing gas atmospheres.*

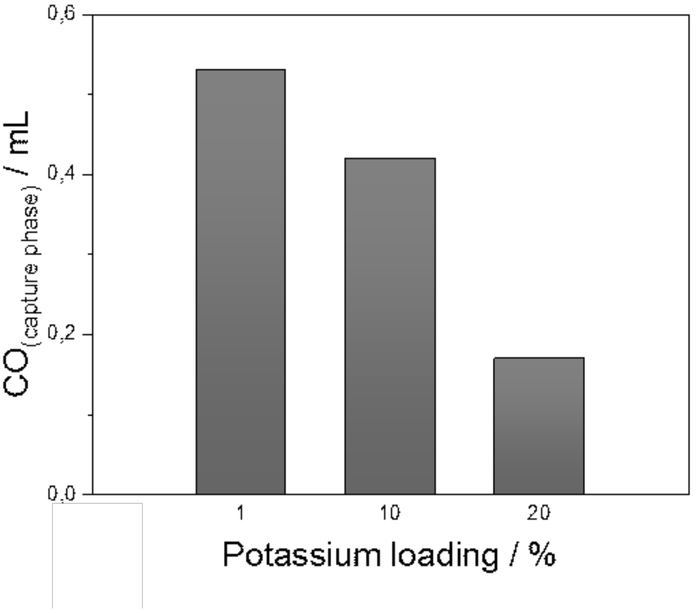

Figure 4.8: *Volume (mL) of CO evolved during the CO_2 capture phase for the series of K-promoted 1Cu/Al_2O_3 at different K loadings (wt.%).*

catalyst, 12Cu/Al_2O_3 catalyst (Figure 4.9(a)) did not show any CCR activity. For the 12Cu-2K/Al_2O_3 catalyst (Figure 4.9(b)), a similar behaviour is reported, with a reduced CO peak in the capture phase and little CO evolution after the switching to the H_2 atmosphere. Summarising these results, the importance of K for CO_2 uptake is again stated, since initial higher CO_2 capture and CO evolution during the reducing phase were reached only in presence of a high K loading. CO signals during the CO_2

phase were greatly affected by increasing amount of K, confirming the hindering effect on Cu particles, especially at high loadings. Figure 4.10 reports the volumetric amount of CO evolved during the CO_2 phase.

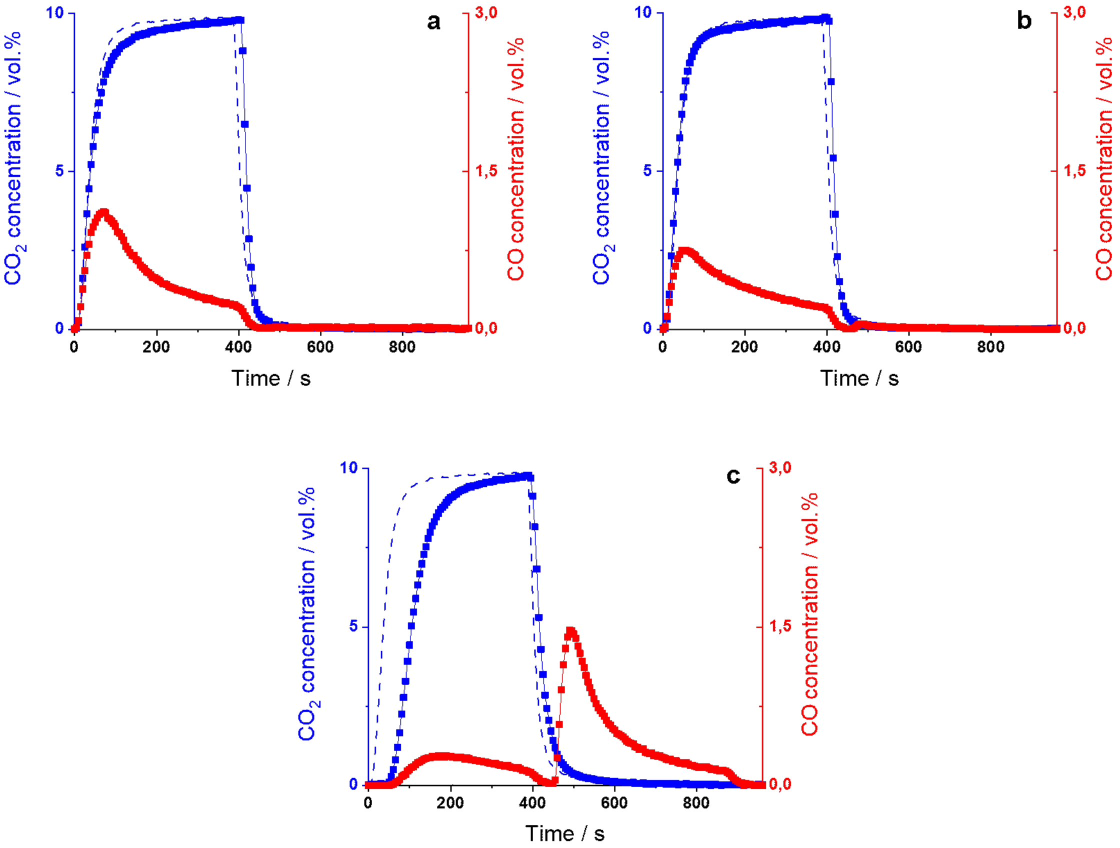

Figure 4.9: *Average concentration profiles of CO_2 and CO during CCR operation at 350 °C for a) 12Cu/Al_2O_3, b) 12Cu-2K/Al_2O_3 and c) 11Cu-2K/Al_2O_3. Alternation of 9.9% CO_2 in He phase at 25 mL min^{-1} and 100% H_2 at 50 mL min^{-1}. Blank profile (dashed line) and reaction profile (solid line). Pure He at 50 mL min^{-1} is interposed between oxidising and reducing pulses.*

4.6 Effect of Cu loading

The effect of Cu loading was investigated by comparing the catalytic activities of the 10K/Al_2O_3 (Figure 4.7), the 1Cu-10K/Al_2O_3 (Figure 4.6(b)) and the 11Cu-10K/Al_2O_3 IWI (Figure Figure 4.11) catalysts.

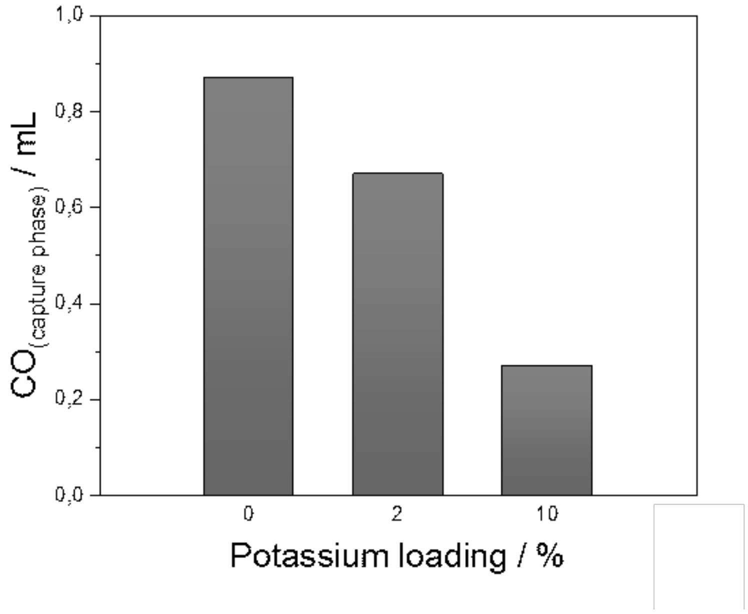

Figure 4.10: *Volume* (mL) *of CO evolved during the CO_2 capture phase for the series of catalysts made from the 12Cu/Al_2O_3 at different K loadings (wt.%).*

The absence of Cu entailed the inability of the catalyst to reduce the adsorbed CO_2. This was evident from the different behaviour of the 10K/Al_2O_3 (Figure 4.7) and the 11Cu-10K/Al_2O_3 (Figure 4.11) between the first cycle and the following ones. For the former catalyst, during the first CCR cycle CO_2 was almost fully captured for 60 s. A continuous and low CO signal was detected during the reducing phase, which was attributed to carbonates decomposition. Formation of stable K_2CO_3 species which were difficult to decompose in H_2 at reaction temperature is expected from H_2-TPR analysis reported in Figure 3.4, undermining the reversibility of the process. As a consequence, in the following cycles, no active sites were available for CO_2 uptake. In the case of the 11Cu-10K/Al_2O_3 instead, 40 s of CO_x full capture were observed during the first cycle, but the catalyst was still active for capture in the following ones. Therefore, Cu determined the restoration of the active sites, although the complete removal of carbonate species was not achieved, resulting in a shorter initial full capture interval (20 s).

Considering the catalysts loaded with 1 wt.% and 11 wt.% of copper, Figure 4.6(b) and Figure 4.11(b) respectively, less CO formation in the reduction phase was detected for the catalyst with higher Cu loading. The evolved CO was 1.10 mL for the 11Cu-10K/Al_2O_3 IWI and 1.32 mL for the 1Cu-10K/Al_2O_3. However, the CO profile in the

H_2 phase suggested a faster reduction kinetics for the former catalytic system. This is in agreement with previous studies in which Cu particles were identified as the active sites for H_2 dissociative adsorption,[63] thus higher Cu loadings increase the availability of active sites for promoting CO_2 reduction. However, a maximum loading is also reported for Cu.[43]

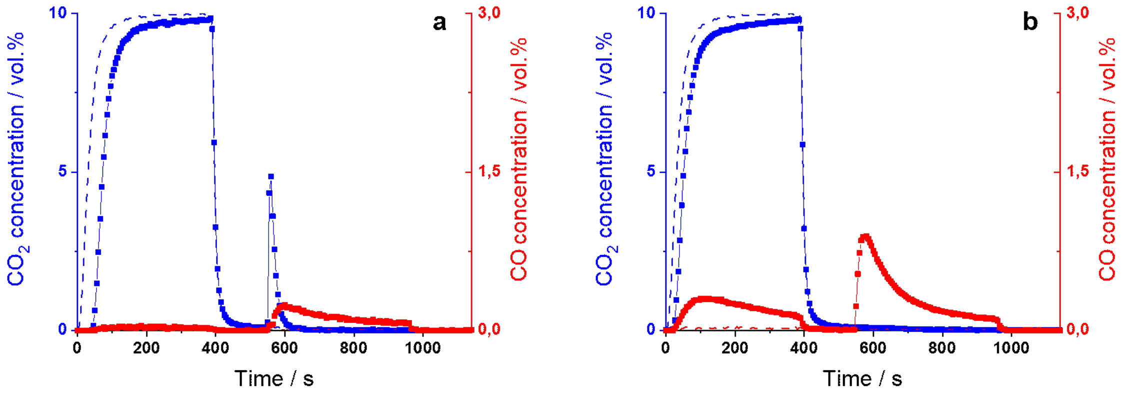

Figure 4.11: *Concentration profiles of CO_2 and CO during CCR operation at* 50 °C *with 9.9% CO_2 in He at* 25 mL min^{-1} *vs. 100% H_2 at* 50 mL min^{-1} *at atmospheric pressure over the 11Cu-10K/Al_2O_3 IWI during a) the 1st cycle and b) averaged on the following ones. Pure He at* 80 mL min^{-1} *is flushed between oxidizing and reducing gas atmospheres.*

Observing the CO_2 phase, although a similar CO_x full capture interval was obtained with the 1 wt.% and 11 wt.% Cu-loaded catalysts, a difference in the amount of evolved CO was found. Operating the reaction with the catalyst with higher Cu loading resulted in a CO formation of 0.32 mL, against the 0.42 mL of the 1 wt.% Cu. Nonetheless, a higher evolution of CO due to Cu oxidation would be expected for the catalyst containing higher amount of Cu. A possible explanation of this phenomenon is the involvement of Cu-K interfaces as active sites for carbonaceous species uptake. Indeed, a greater population of interfacial sites can be formed at higher Cu loading. As a confirmation, works from Liang et al.[48] and Chen et al.[46] investigating rWGS catalysts concluded that active sites for CO_2 adsorption were generated at the interfaces between K and the active metal (Pt and Cu, respectively). Such result is in accordance with H_2-TPR analysis (Figure 3.4), in which strong interaction between copper and potassium species was observed, since the reduction pattern was relevantly modified with the increase in the amount of K impregnated. Nevertheless, an optimum Cu loading should exist to reach the best trade-off between interfacial capture sites and Cu particle dispersion. In this sense, 11 wt.% Cu loading may be excessive, as suggested by SEM imaging (Figure 3.7), in which Cu agglomerates were found in the catalyst after calcination. This conclusion offers the possibility for further research in catalyst engineering.

As a final remark, the probability for CO_2 dissociation may be enhanced on H-adsorbed Cu surfaces. Studying the reaction mechanism of the rWGS reaction, Chen et al.[64] pointed out that H_2 may be involved also in different reaction pathways than the reduction of oxidised Cu, showing the promoting effect of H_2 towards CO_2 conversion. Similar conclusions were inferred by Campbell et al.[65], who proposed a hydrogen-assisted CO_2 dissociation for rWGS. In their work, they suggested that high hydrogen coverage may favorably influence the rate of CO_2 dissociation, perhaps via a H_2-induced surface reconstruction. All previous considerations bring to the conclusion of the direct involvement of Cu not only in the CO_2 reduction mechanism, but also in its reversible capture.

4.7 Ex situ and in situ Raman investigation

The investigation of γ-Al_2O_3 by Raman spectroscopy was made difficult by the strong fluorescent emission that covers its Raman spectra.[66] Although ZrO_2-supported catalysts showed lower CCR activity than the correspondent Al_2O_3-supported, the system was chosen for Raman investigation thanks to the better Raman activity of the support. Ex-situ analysis on the samples revealed that in presence of high loadings of Cu, the Raman signal from the support was suppressed. In fact, for the 10Cu-10K/ZrO_2 catalyst we could not detect neither the typical Raman scattering patterns deriving from the support (50-650 cm^{-1}), nor from the K_2CO_3 (1057 cm^{-1}). To overcome this limitation, a sample with 1 wt.% copper loading on ZrO_2 (1Cu-10K/ZrO_2), proved its catalytic activity (results shown in Figure 4.12) was utilised for in-situ Raman investigation. Ex-situ characterisation of the catalysts and support powders was performed loading a capillary in a system equipped with a red laser excitation source (γ_{exc} =785nm), as shown in Figure 4.13. After the loading of Cu (1Cu/ZrO_2), a significant loss in the intensity of the ZrO_2 Raman peaks was noticed, especially at high Raman shift. Thus, the 1 wt.% Cu loading was found to be the compromise between CCR activity and Raman activity of the sample. The subsequent loading of potassium resulted in the appearance of the characteristic K_2CO_3 Raman signal (peak at 1057 cm^{-1}), with the broadening of the band indicating its existence in a highly dispersed nanocrystals or amorphous-like phase.

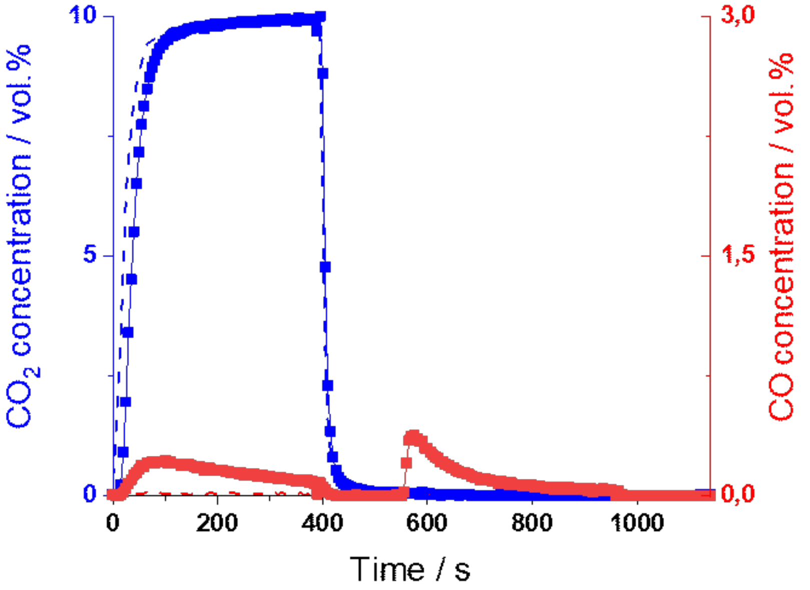

Figure 4.12: CCR activity at 350 °C for the 1Cu-10K/ZrO_2.

Figure 4.14(a) shows the in-situ Raman spectra obtained for 1Cu-10K/ZrO_2. At room temperature, the ZrO_2 Raman bands were visible in the low Raman shift region (50-650 cm^{-1}) together with the Raman band of the K_2CO_3 at 1057 cm^{-1}. However, after reduction in H_2 at 350 °C, both signals from the support and K_2CO_3 were intensively modified, with a loss of intensity of the characteristic peaks. This behaviour was not found in absence of Cu, for the 10K/ZrO_2 catalyst (Figure 4.14(b)), in which the signals were preserved at higher temperature. We addressed this behaviour to the formation of a highly dispersed state of metallic Cu nanoparticles in K phase which cover the support, resulting in the decline of Raman signals from the support. Additionally, the broad signal from 1300 to 1700 cm^{-1} may be indicative of some K phase rearrangements, since it did not fully reproduce the signal ascribed to the quartz tube.

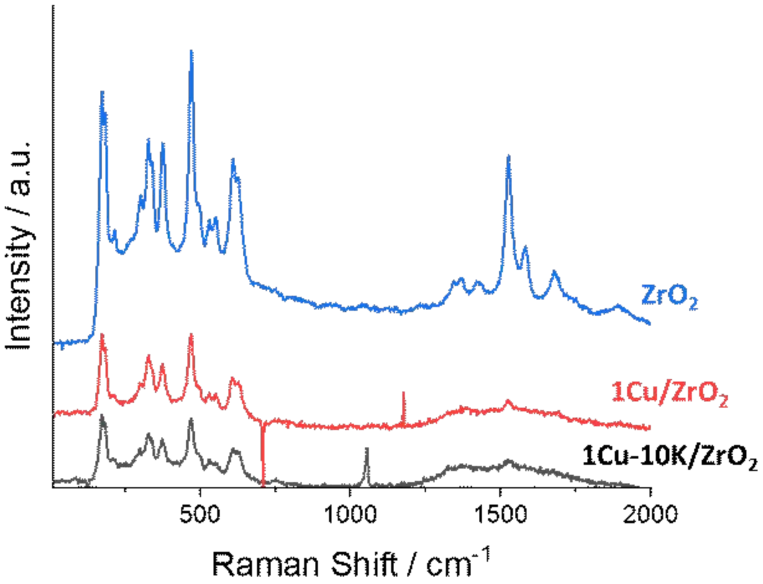

Figure 4.13: *Ex-situ Raman (γ_{exc} =785nm) characterization of ZrO$_2$-supported catalysts.*

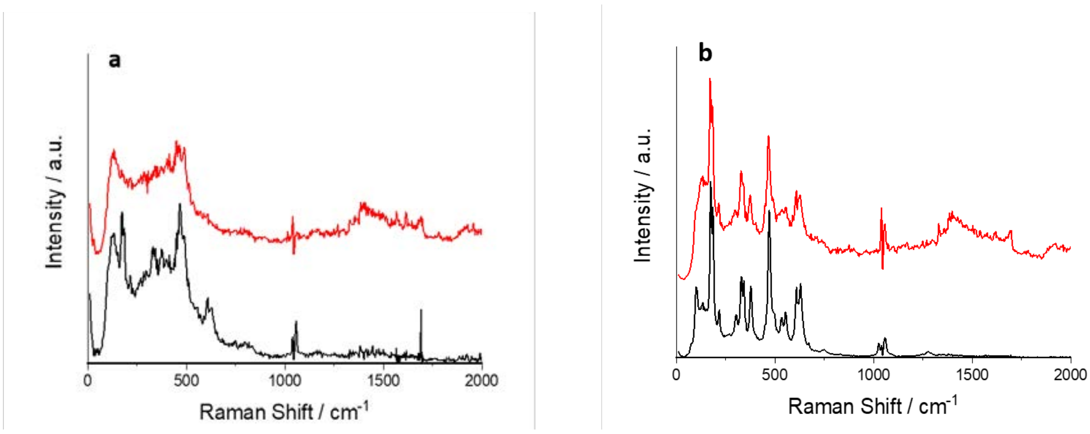

Figure 4.14: *In-situ Raman spectra of a) 1Cu-10K/ZrO$_2$ and b) 10K/ZrO$_2$ at room temperature (black profiles) and at 350 °C (red profiles) in H$_2$ flow.*

By monitoring the catalyst bed during reaction, the appearance of a gradient colour change during the first CO$_2$ cycle was detected. To investigate this behaviour, in-situ Raman spectroscopy was conducted on 1Cu-10K/ZrO$_2$. The reducing pretreatment in H$_2$ at 450 °C led to a dark-coloured catalyst with the disappearance of the Raman signal acquired at room temperature. The reduced state of copper and its high dispersion on the catalyst may significantly affect the detection of Raman radiation from the catalyst. Spatial analysis of the catalyst was performed by selecting four different probing positions along the catalytic bed to collect the Raman signal. Remarkably, during the first CCR cycle a progressive visible colour change of the catalyst was noticed under

CO_2 flow (Figure 4.15), associated with the progressive recovering of the Raman signals from the support and K_2CO_3. As mentioned earlier, during the first cycle a higher CO_2 uptake happened, related to the formation of stable K_2CO_3 species which were not easily decomposed in the following reducing treatment. It was not clear if this phenomenon can be accompanied by a bulk oxidation of the Cu species. On one hand, the visible colour change, together with the appearance of Raman signals in the region around 600 cm^{-1} would suggest the formation of copper oxides species.[67,68] On the other hand, in the first cycles of the catalytic tests, very low CO signals were detected, contrasting the hypothesis of bulk Cu oxidation. In the following cycles, the colour change was lost, suggesting that a higher dispersion of Cu was achieved. This eventually resulted in a definitive loss of the Raman features from the support and K_2CO_3.

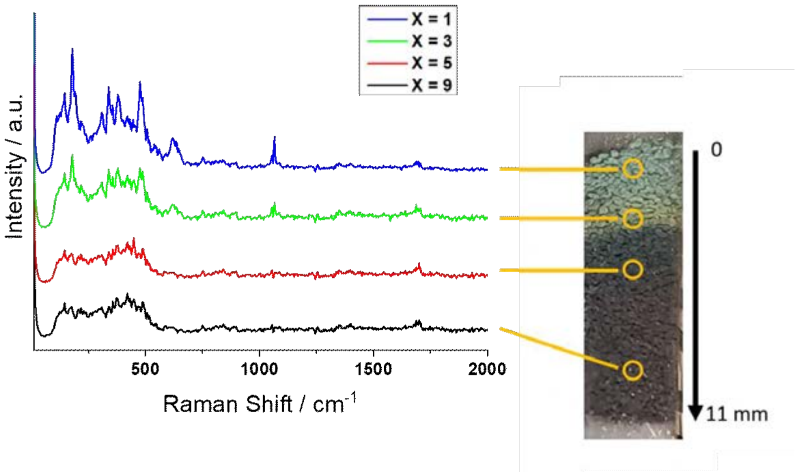

Figure 4.15: *In-situ Raman of 1Cu-10K/ZrO_2 at different position along the catalyst bed at 350 °C after first H_2-CO_2 cycle.*

4.8 First CCR cycle behaviour and formation of the CCR active phase

Another possibility is that redox cycles play a role in the formation of the active phase, with the activation of H_2 on reduced copper participating to the reaction mechanism. As mentioned in the description of the catalytic testing setup in Section 2.1, a USB camera was mounted over the quartz tube reactor to monitor possible visible rearrangements of the catalyst bed, particularly in relation to colour changes. Remarkably, we noticed progressive colour change of the catalyst bed between the oxidising and reducing phases in the first redox cycle only. In addition, a relevant colour change was detected only in presence of K-promoted catalysts. This fact projected in a deviated catalytic activity during the first cycle, which was valuable to focus on since it should rather be linked to the activation process of the catalyst towards CCR ability.

From the videoclips recorded with USB camera, during the first redox cycle the catalytic bed assumed two different colours, depending on the gas atmosphere under which it was subjected: during the CO_2 phase, the catalyst was partially denoted by a fair colour, whereas in the H_2 phase it became almost black. Both the colour changes between phases were continuously progressive, but while the darkening related to catalyst reduction was fast and total, the colour change associated with the oxidising phase was slower. For some catalysts, the colour change was detected also in following cycles, even if in a poorer and poorer extent, until it was no more recognisable. Moreover, from the diversity between the colour assumed by the same catalyst exposed to CO_2 and O_2, we could conclude that the colour change during CCR was not related to a complete oxidation of the pre-reduced Cu particles to CuO.

Figure 4.16 shows the image of the catalytic bed during the CO_2 phase for different catalysts during the first cycle, along with the concentrations of CO_2 and CO in the reactor effluent in the first cycle and the evolution in time of the H_2O IR signal absorbance. Surprisingly, no significant colour change was visible for the unpromoted $12Cu/Al_2O_3$ catalyst, combined with a very low CO evolution during the oxidising phase. For this catalyst, water was hardly detected in the first cycle. In presence of K, a colour change was noticed during the first CO_2 phase. This colour change was not associated to the capture mechanism since it was continuously progressing during all the CO_2 phase, while CO_2 consumption/capture stopped earlier in the pulse. Rather, Cu can be mildly oxidised by CO_2 during the first CO_2 pulse. However, according to IR analysis this process did not result in CO evolution. For this reason, a dynamic transfer of oxidising species along the bed may be involved.

Given that the colour change was limited to the first redox cycle and it was related to a peculiar reaction mechanism, we inferred that a phase change may be induced. The first alternation of CO_2 and H_2 gives birth to the CCR active phase: Cu particles are heavily dispersed in the K phase, and this process may be promoted with a H_2-induced surface reconstruction, associated with the released of the previously captured CO_2 and high formation of H_2O. In this condition, high dispersed Cu active sites promotes the activation of H_2 and conversion of the stored CO_2 to CO observed in the following cycles, namely during the quasi-steady state operation. Such phenomenon would be in accordance, for instance, with TEM images of the used 11Cu-10K/Al_2O_3 catalyst (Figure 3.12(c) and Figure 3.12(d)), where Cu nanoparticles smaller than those found in the as-synthesised catalyst were identified, dispersed in branched K structures. Therefore, the active phase for CCR can be formed in the first redox pulse, resulting in the loss of colour change.

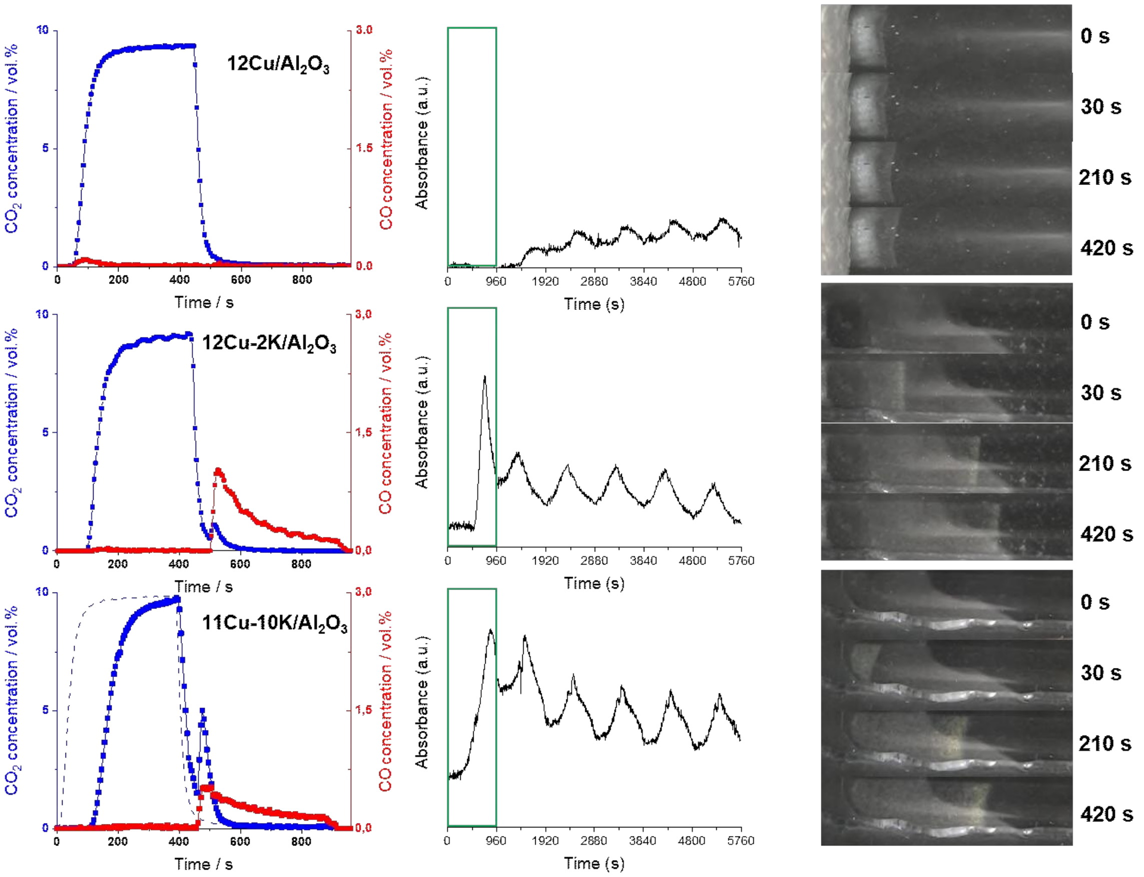

Figure 4.16: *CO_2 and CO concentration profiles during the 1st CCR cycle at 350 °C for the 12Cu/Al_2O_3 catalysts with different K-loading (left column), IR H_2O signal evolution during CCR reaction, in which the 1st cycle behaviour is highlighted in green (central column), and images of the colour change of the catalysts at different time instants during the CO_2 of the 1st CCR cycle.*

Chapter 5

Process parameters optimisation

The last part of the experimental project was focused on the optimisation of process parameters. In view of a future application, the ideal CCR process would provide an extended full CO_2 uptake and a fast reduction to CO. It is also important that capture and reduction processes can efficiently take place in equal time intervals, so that the alternation of the gas phases can be implemented in a continuous process. The 11Cu-10K/Al_2O_3 catalyst was selected as the reference catalyst since it showed appreciable CCR performance. Blank signals were retrieved exposing the catalyst to CO_2-H_2 cycles at room temperature.

In order to evalute process performance at different conditions, the definition of suitable quantities was required. Considering the CO_2 phase only, due to the simultaneous CO_2 capture and CO_2 conversion to CO by Cu oxidation, CO_2 full capture efficiency was defined as:

$$\mathrm{CO_2}\ \textit{full capture efficiency} = 100 \times \frac{\mathrm{CO}_{2(ads,fc)}}{\mathrm{CO}_{2removed}} \tag{5.1}$$

where $\mathrm{CO}_{2(ads,fc)}$ is the amount of CO_2 adsorbed during the initial full capture period, and $\mathrm{CO}_{2removed}$ the difference between the CO_2 signals of the blank and the one obtained at reaction conditions. They are calculated as:

$$\mathrm{CO}_{2(ads,fc)} = \int_0^{t_{fc}} c_{\mathrm{CO_2},0}\,dt - \int_0^{t_{fc}} c_{\mathrm{CO_2}}\,dt \tag{5.2}$$

$$CO_{2removed} = \int_0^{t_{capture}} c_{CO_2,0} dt - \int_0^{t_{capture}} c_{CO_2} dt \tag{5.3}$$

where t_{fc} and $t_{capture}$ are the time instants at which the initial CO_x and the CO_2 phase end, respectively, whereas $c_{CO_2,0}$ and c_{CO_2} are CO_2 concentration for the blank and catalytic tests, respectively. CO_2 full capture efficiency is then defined as the percentage of CO_2 captured during the initial full capture interval with respect to the total CO_2 removed from the inlet flow. This is a measure of how efficiently the catalyst can provide full capture.

Considering the reduction phase, CO_2 reduction efficiency was defined as:

$$CO_2 \ \textit{reduction efficiency} = 100 \times \frac{CO_{(ev,fc)}}{CO_{produced}} \tag{5.4}$$

where $CO_{(ev,fc)}$ is the amount of CO evolved after the switching to the H_2 phase during a time interval equal to the full capture period, and $CO_{produced}$ is the total amount of CO produced in the whole H_2 pulse. They are calculated as:

$$CO_{2(ev,fc)} = \int_0^{t^*_{fc}} c_{CO} dt \tag{5.5}$$

$$CO_{2produced} = \int_0^{t_{reduction}} c_{CO} dt \tag{5.6}$$

t^*_{fc} and $t_{reduction}$ indicate the time instant in the reducing phase equal to t_{fc} and the time instant in which the reducing phase ends. CO_2 reduction efficiency indicates the ability of the catalyst to provide fast reduction of the captured CO_2. The time interval for the integrals defining $CO_{2(ads,fc)}$ and $CO_{(ev,fc)}$ was selected equal to the CO_2 full capture period during the CO_2 phase to express the potential towards the synchronisation of the two phases in a real process.

Reaction temperature, GHSV during the CO_2 phase and GHSV during the H_2 phase were considered for CCR optimisation, GHSV being calculated as:

$$GHSV = \frac{\dot{F}}{W} \tag{5.7}$$

where $\dot{F}$ is the volumetric flow rate of the targeted gas species in $m^3\,s^{-1}$ and W is the amount of catalyst loaded in the reactor in kg. Due to the limited volume of the reactor, variation in GHSV will be tested only by modifying gas flow rates. In principle, a similar approach could be developed varying the catalyst loading. Furthermore, the effect of different synthesis conditions on the process performances was investigated. Catalysts prepared using different water amounts in the impregnation step of the potassium precursor were tested. All tests were performed at ambient pressure. Calculated H_2/CO ratios in the effluent are estimated values, since they were calculated as if a rWGS was occurring; in addition, water was partially condensed before entering the IR detector, precluding the determination of the consumed H_2.

5.1 Effect of temperature

Figure 5.1 illustrates concentration profiles of CO_2 and CO obtained at four different reaction temperatures, namely 300, 350, 400 and 450 °C. The choice of the temperature range relies on the activation of reduction processes in H_2, as shown in temperature programmed analysis (Figure 3.4), which are fundamental to develop the active metallic Cu phase. Due to the calcination temperature of 500 °C, higher temperatures are not investigated. Since temperature affects both the CO_2 uptake process and its reduction, Figure 5.2 describes how CO_2 full capture efficiency and CO_2 reduction efficiency are influenced. At 300 °C, no full capture was noticed, while increasing temperatures led to contrasting effects. The integration interval for full capture was set to 20 s. On the one hand, higher temperature promoted the oxidation of Cu by CO_2. This resulted in a reduced full capture efficiency, since a larger portion of the CO_2 eliminated from the flow was consumed in the undesirable pathway of Cu oxidation. However, this drop in full capture efficiency was limited, passing from 6% at 350 °C to 4% at 450 °C. On the other hand, higher temperature remarkably enhanced the kinetics of reduction of the stored CO_2 under the H_2 flow, as the CO signal peak narrowed. As a consequence, CO was produced in a higher amount during the same time interval. In this sense, similarity with the rWGS would explain this endothermic reduction. CO_2 reduction efficiency raised from 7% at 350 °C to 22% at 450 °C. Thus, higher temperatures looks desirable for enhancing fast and efficient reduction of the captured CO_2.

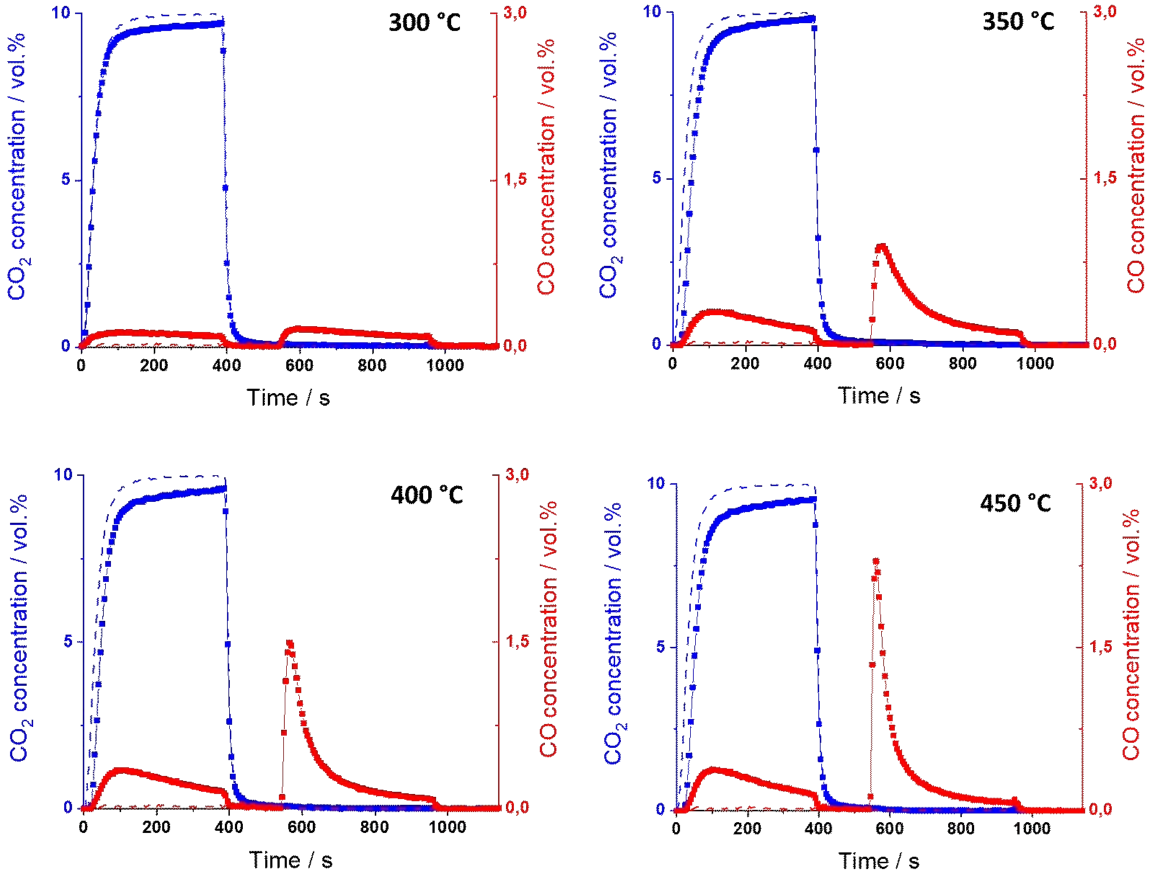

Figure 5.1: *Average concentration profiles of CO_2 and CO during CCR operation at different temperatures for the 11Cu-10K/Al_2O_3 IWI catalyst. Alternation of 9.9% CO_2 in He phase at* 25 mL min^{-1} *and 100% H_2 at* 50 mL min^{-1}. *Pure He at* 80 mL min^{-1} *is interposed between reactant pulses.*

The catalyst stability was alo tested at 450 °C. Due to catalyst availability, the 11Cu-10K/Al_2O_3 IWI-mod was used in the experiment. 50 CCR cycles were carried out, corresponding to almost 16 h operation. CO_2 and H_2 flowrate were kept the same of the previous tests. The catalytic system showed good stability during all cycles, as can be observed in Figure 5.3. This result confirmed the regenerability of the active phase for CO_2 uptake during the reducing phase.

5.2 Effect of GHSV during the CO_2 phase

GHSV during the CO_2 phase was varied by modifying the CO_2 flow rate while keeping constant the catalyst amount in the reactor, that was 200 mg. Three different tests were

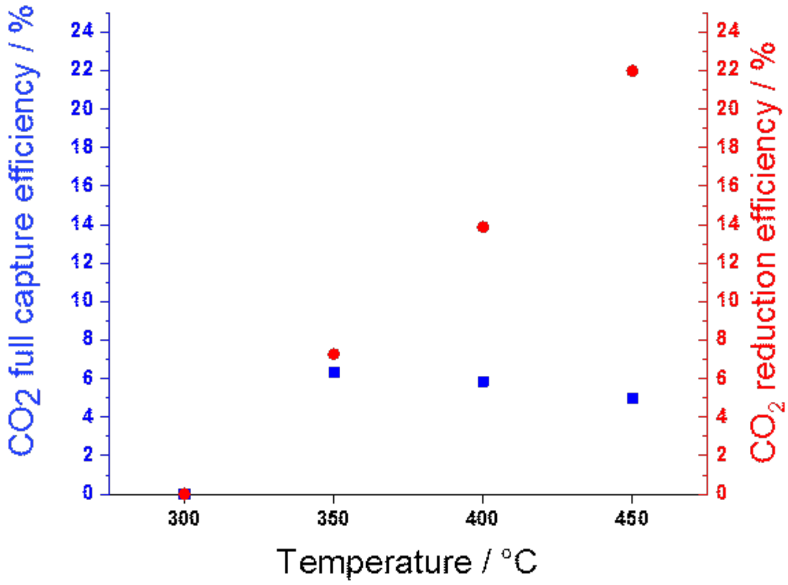

Figure 5.2: *CO_2 full capture efficiency (blue) and CO_2 reduction efficiency (red) from CCR activity of 11Cu-10K/Al_2O_3 IWI at different reaction temperatures.*

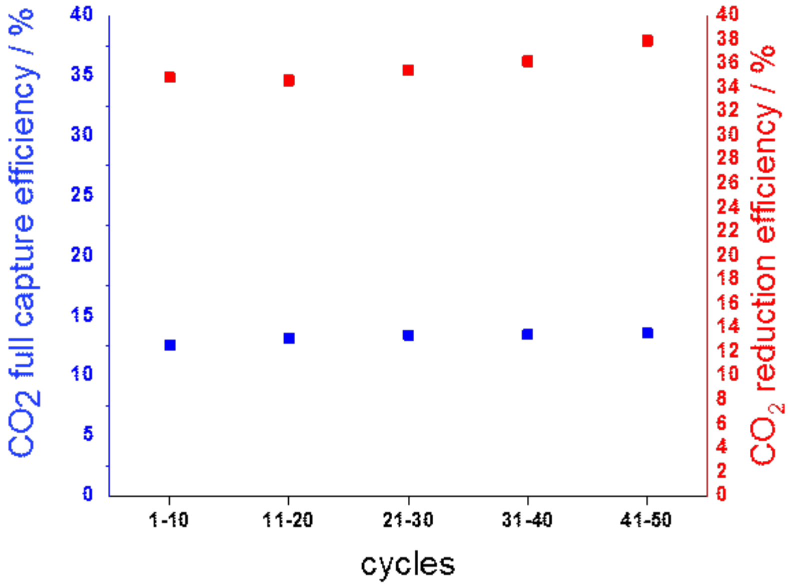

Figure 5.3: *CO_2 full capture efficiency (blue) and CO_2 reduction efficiency (red) from CCR activity of 11Cu-10K/Al_2O_3 IWI-mod during 50-cycle CCR.*

carried out, flowing 50, 25 and 10 mL min^{-1} of 9.9 vol.% CO_2 over the catalytic bed, corresponding to a GHSV of 0.0825 m^3 kg^{-1} s^{-1}, 0.0413 m^3 kg^{-1} s^{-1} and 0.0165 m^3 kg^{-1} s^{-1} respectively. H_2 flow rate in the reducing phase was maintained equal to 50 mL min^{-1}, and reactions were carried out at 350 °C. CO_2 and CO concentration profiles are shown in Figure 5.4, while Figure 5.5 shows the effect on the CO_2 reduction efficiency. Due to the different amount of CO_2 involved in the capture process, CO_2 full capture efficiencies for the three tests were not comparable. As predictable, the initial full capture interval during the CO_2 phase increased with the decrease in the CO_2 flow rate, namely at lower GHSV, passing from 5 s at 50 mL min^{-1} to 30 s at 10 mL min^{-1}: longer contact time favored CO_x uptake. From the point of view of the process, having a longer capture phase would be beneficial in terms of reduction, since a higher amount of CO during H_2 phase could evolve. CO_2 reduction efficiency was almost doubled decreasing the CO_2 flow rate form 25 mL min^{-1} to 10 mL min^{-1}. Therefore, as a consequence of the longer initial full capture period, the latter CO_2 flow rate is selected for the following tests. In principle, same results could be obtained fixing the CO_2 flow rate and increasing the amount of available active sites by loading higher quantity of catalyst in the reactor.

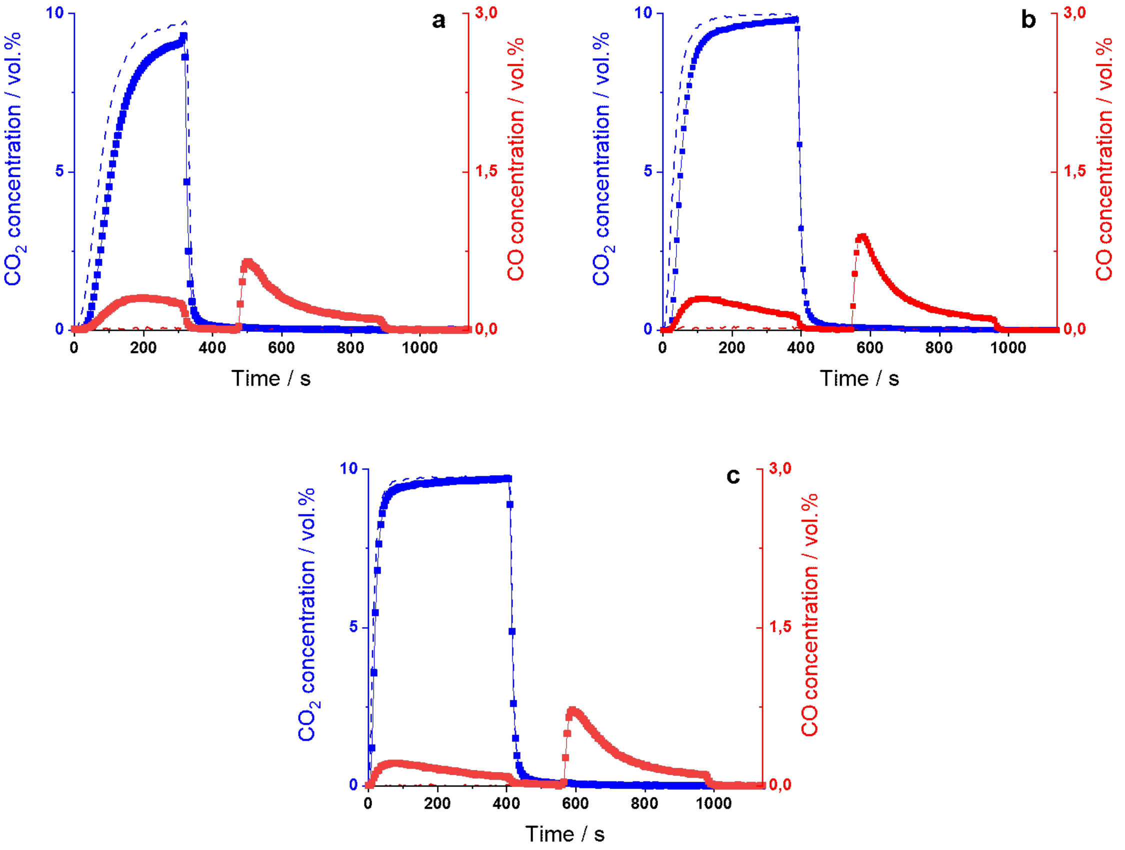

Figure 5.4: *Average concentration profiles of* CO_2 *and CO during CCR operation at* 350 °C *for the 11Cu-10K/*Al_2O_3 *catalyst. Alternation of 9.9%* CO_2 *in He phase at a)*10 mL min^{-1}*, b)* 25 mL min^{-1} *and c)* 50 mL min^{-1} *and 100%* H_2 *at* 50 mL min^{-1}*. Pure He at* 80 mL min^{-1} *is interposed between reactant pulses.*

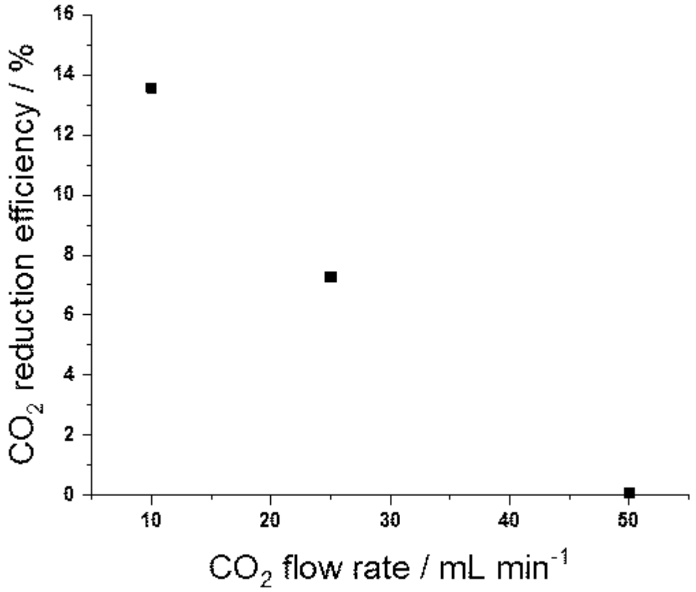

Figure 5.5: *CO_2 reduction efficiency from CCR activity of 11Cu-10K/Al_2O_3 at different CO_2 flow rates during the oxidising phase.*

5.3 Effect of GHSV during the H_2 phase

Similar tests on the effect of GHSV during the reducing phase were performed by modifying the H_2 flow rate. H_2 concentration was kept constant at 100 vol.%. The target of these experiments was the possibility to decrease the H_2/CO ratio in the product effluent, so as to obtain a syngas already suitable as feedstock for the Fisher-Tropsh process. Three catalytic tests were carried out using 50, 20 and 10 mL min^{-1} of pure H_2, corresponding to GHSVs of 0.833 m^3 kg^{-1} s^{-1}, 0.333 m^3 kg^{-1} s^{-1} and 0.167 m^3 kg^{-1} s^{-1} respectively. Reactions were carried out at 350 °C. Figure 5.6 presents CO_2 and CO concentration profiles obtained. Clearly, CO_2 full capture efficiency remained unchanged, while the effect on the CO_2 reduction efficiency is reported in Figure 5.7.As expected, according to CCR process purpose, variations H_2 flow rate led to two contrasting effects. On the one hand, reduction kinetics was strongly improved at higher H_2 flow rate, due to the increased H_2 partial pressure. CO2 reduction efficiency raised from 1% to 14% passing from 10 to 50 mL min^{-1} of pure H_2 flow rate. On the other hand, the increase in H_2 flow rate involved a drop in the H_2/CO ratio of the syngas product. Nonetheless, excess H_2 separation from the product stream and its recycle was still needed at lower H_2 flow rates, so we selected 50 mL min^{-1} of pure H_2 as the best choice for an effective conversion of the chemically adsorbed CO_2 to CO. In this way, a large amount of excess H_2 needs to be removed and recycled in order to obtain a suitable syngas.

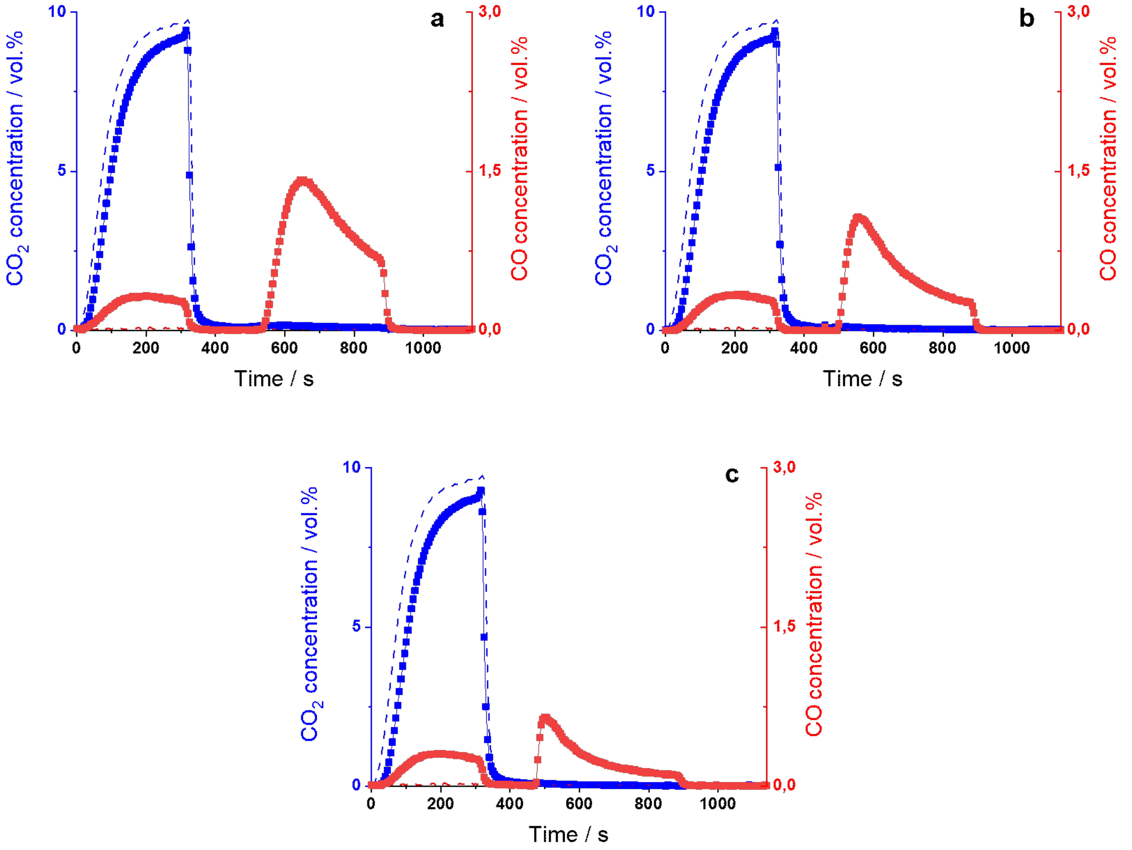

Figure 5.6: *Average concentration profiles of CO_2 and CO during CCR operation at* 350 °C *for the 11Cu-10K/Al_2O_3 catalyst. Alternation of 9.9% CO_2 in He phase at* 10 mL min^{-1} *and 100% H_2 at a)* 10 mL min^{-1}*, b)* 20 mL min^{-1} *and c)* 50 mL min^{-1}*. Pure He at* 80 mL min^{-1} *is interposed between reactant pulses.*

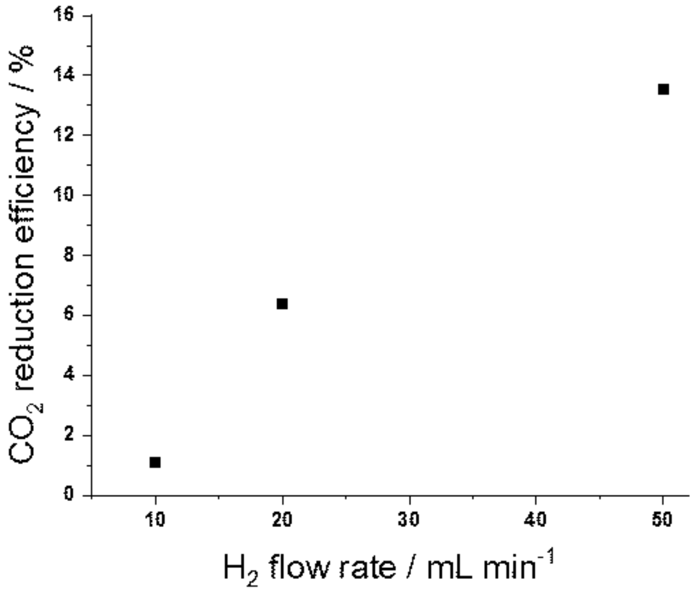

Figure 5.7: *CO_2 reduction efficiency from CCR activity of 11Cu-10K/Al_2O_3 at different H_2 flow rates during the reducing phase.*

5.4 Effect of the water amount in the potassium impregnation step

The last parameter investigated for catalyst optimisation was the amount of water used for K_2CO_3 dissolution before the impregnation on the 12Cu/Al_2O_3 catalyst. This factor may play a significant role in the catalyst synthesis and activity, as concluded from the comparison of the two 11Cu-10K/Al_2O_3 different batches illustrated previously. Three different 11Cu-10K/Al_2O_3 catalysts were prepared. In the first synthesis, the recommended amount of water for the K impregnation step was used. According to the incipient wetness impregnation method, the amount of water is equal to the nominal pore volume of the catalytic support. In the other two synthesis, the amount of water used was twice and three times the nominal quantity. Figure 5.8 shows the CO_2 and CO concentration profiles for the catalytic tests carried out on these catalysts at 350 °C. The observed full capture period shifted from 30 s to 45 s and to 65 s increasing the water amount in the K impregnation step. These findings suggested that important properties as Cu and K species dispersion, which is essential for CO_2 uptake, can be significantly influenced by the synthesis conditions. To better visualise the effect on the process performance, CO_2 full capture efficiency and CO_2 reduction efficiency are reported in Figure 5.9. Both raised significantly with the increased amount of water utilised for the synthesis. For the catalyst synthesised using the higher amount of water, CO_2 full capture efficiency attained 11% and CO_2 reduction efficiency reached 31%. The improved dispersion of active species on the catalytic support can be the reason of the enhanced activity of the catalyst. Given these preliminary results, synthesis procedure should be investigated more in detail by means of additional characterisations, with a particular focus on K detection techniques. Moreover, different synthesis methods can be explored to optimise the catalytic system properties.

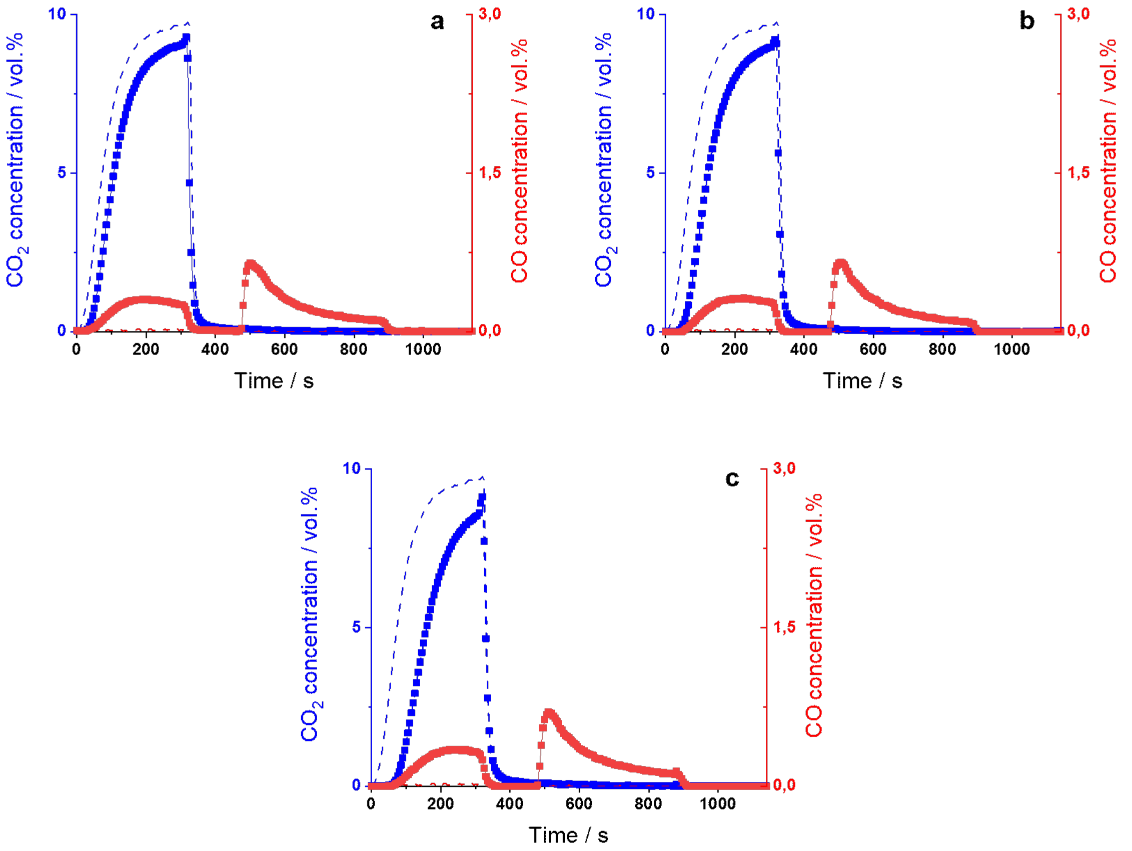

Figure 5.8: *Average concentration profiles of CO_2 and CO during CCR operation at* 350 °C *for the 11Cu-10K/Al_2O_3 catalyst synthesised with a) the recommended amount of water for K precursor impregnation, b) twice and c) three times this amount. Alternation of 9.9% CO_2 in He phase at* $50\,\mathrm{mL\,min^{-1}}$. *Pure He at* $80\,\mathrm{mL\,min^{-1}}$ *is interposed between reactant pulses.*

Combining the previous results, we were able to point out the optimal operating conditions and process parameters for an effective CCR process. The 11Cu-10K/Al_2O_3 catalyst, synthesised with three times the nominal amount of water in the impregnation step of K_2CO_3, was selected as it showed the best CO_2 uptake ability. In a complete

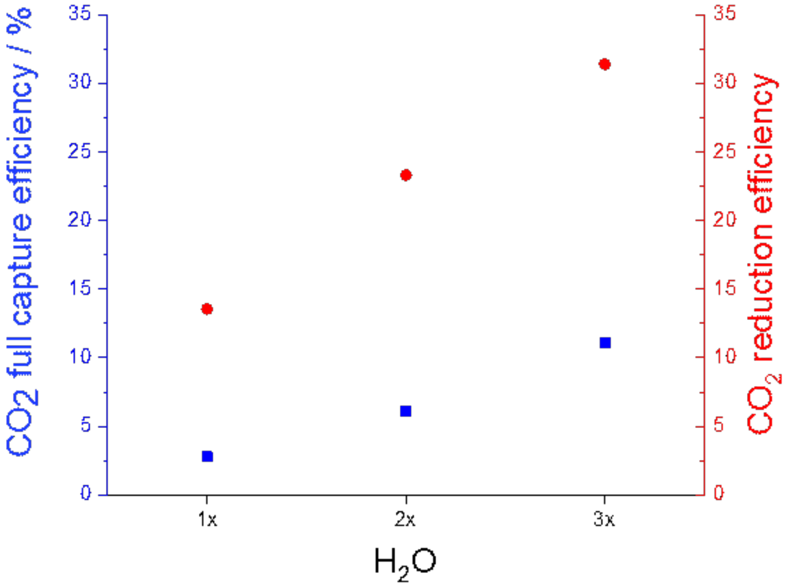

Figure 5.9: *CO_2 full capture efficiency and CO_2 reduction efficiency from CCR activity of 11Cu-10K/Al_2O_3 synthesised with different amounts of water.*

CCR cycle, the catalyst was exposed to 10 mL min^{-1} of 9.9 vol.% CO_2 in the oxidising phase alternated to 50 mL min^{-1} of pure H_2 in the reducing phase. As mentioned earlier, the low GSHV during the capture phase allows for a longer contact time between the gas and the adsorption sites, resulting in a longer full capture interval, while a greater partial pressure of H_2 in the reducing phase favors the CO_2 reduction. CO production after the switching to the H_2 atmosphere was furtherly improved operating at 450 °C, to speed up the CO_2 reduction kinetics. CO_2 and CO concentration profiles are reported in Figure 5.10. Under these reaction conditions, approximately 100 s of CO_2 full capture were achieved, resulting in a CO_2 full capture efficiency around 33%. Considering a 100 s time interval for the calculation, the obtained CO_2 reduction efficiency is around 65%. By limiting the duration of both phases to 100 s is then possible to reversibly store and convert efficiently CO_2. In this way, such catalytic system can utilise CO_2 from a feed in which it is present in a concentration similar to the one retrievable in a flue gas coming from a fossil power plant. Considering the low amount of CO_2 involved in the flow, the CCR process may be flexibly implemented in future systems for direct air capture, in which CO_2 is found in concentration around 400 ppm. The development of the application towards this direction is attractive, since it would become a negative carbon technology that has the potential to address CO_2 emissions from distributed point sources. The product stream obtained was a syngas characterised by an estimated H_2/CO ratio around 50:1, so excess H_2 separation or mixing with syngas with lower H_2/CO is required to meet the requirements (H_2/CO≈2) of downstream processes as the Fischer-Tropsch synthesis of hydrocarbons.

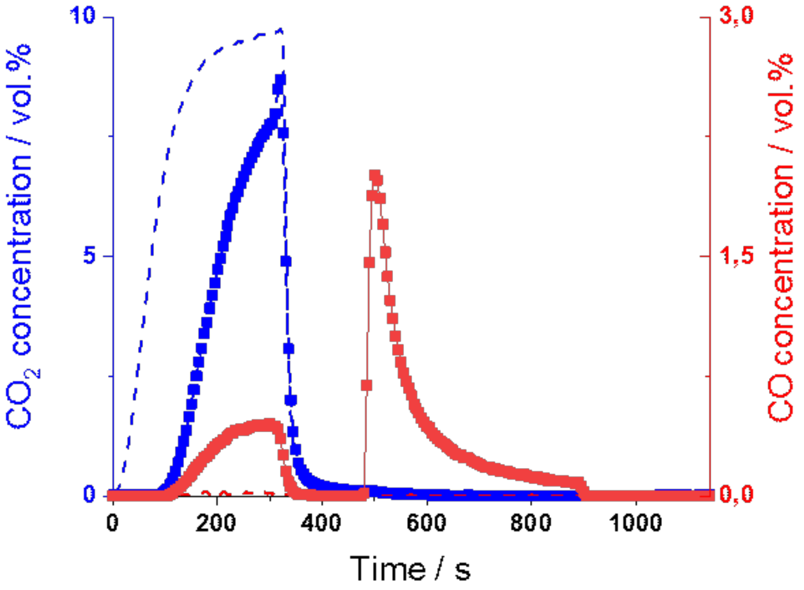

Figure 5.10: *Average concentration profiles of CO_2 and CO during CCR operation at* 450 °C *for the 11Cu-10K/Al_2O_3 catalyst synthesised using three times the recommended amount of water during the K precursor impregnation. Alternation of 9.9% CO_2 in He phase at* 50 mL min^{-1}. *Pure He at* 80 mL min^{-1} *is interposed between reactant pulses.*

Conclusions and perspectives

In this work several remarkable results regarding the catalytic behaviour towards CO_2 Capture and Reduction of K-promoted supported Cu catalysts have been presented. Such novel process targets the reversible sequestration of CO_2 contained in industrial post-combustion flue gases, focusing on a 9.9 vol.% CO_2 stream, and its reduction to CO by means of H_2. Such unsteady-state reaction system is realised by a continuous gas cycling over the catalytic bed, alternating CO_2 and H_2 streams.

In the first part of the experimental work, catalysts synthesised according to the incipient wetness impregnation were tested. Potassium was found to be fundamental for the capture of CO_2 molecules, while the presence of Cu, even at low loadings, was critical for the reduction of the surface species containing the adsorbed CO_2, thus determining the reversibility of the operation and the regeneration of the catalyst. By carrying out a CCR test substituting CO to CO_2, the involvement in the capture process of CO deriving from a mild oxidation of Cu particles was observed, simultaneously with CO_2 adsorption. Al_2O_3-supported catalysts were characterised by a higher BET surface area, along with a longer initial CO_x full capture interval with respect to their ZrO_2- and TiO_2-supported counterparts, pointing out the positive role of active species dispersion to provide active sites for CO_2 adsorption.

Catalysts synthesised through a modified incipient wetness impregnation method showed better performance than the respective catalysts synthesised according to the rigorous method. Addition of water during the impregnation step of the promoter precursor led to a higher dispersion of the active metal, also entailing an increase in the population of the CO_2 active sites. The strong interaction between Cu and K species was in accordance with H_2-TPR analysis.

Al_2O_3-supported catalysts with different amounts of K and Cu were tested to investigate the effect of their loadings. The capture ability of the catalyst increased with the increase of potassium, until a maximum was reached. Similarly, we inferred that Cu should have an optimum loading, given from the trade-off between the formation of interfacial sites for CO_2 adsorption and the homogeneous dispersion. In fact, a too high loading brought to the formation of Cu agglomerates. Moreover, H_2 coverage of the Cu surface could favorably influence CO_2 dissociation through an induced surface reconstruction. Carbonates and formates on the catalyst surface can be generated only when Cu and K species coexist.

In this work, the formation of the active phase for CCR attracted significant attention. In situ Raman spectroscopy was combined with video recording to detect variations of the K-promoted catalyst surface subjected to CO_2 and H_2 atmospheres. The H_2 treatment involved the loss of the Raman signals associated with the support and K_2CO_3, due to the dispersion of Cu nanoparticles in the K phase covering the support. A progressive colour change of the catalytic bed observed only during the first oxidising phase was associated with a higher CO_2 uptake and to Cu nanoparticles that are not evenly dispersed, resulting in a partial recovering of the Raman signals. Such phenomenon suggested the dynamic features of the process, characterised by the high mobility of potassium and the Cu nanoparticles distribution, confirmed by TEM imaging, where Cu particles smaller than in the catalyst after calcination were dispersed in branched K structures. A further indication to this conclusion was the poor activity of the TiO_2-supported catalyst, where a K-containing crystalline phase were detected both by XRD and TEM, which immobilised potassium.

Eventually, optimisation of the process parameters to maximise CCR efficiency was performed. The influence of temperature, GHSVs (flow rates) in both oxidising and reducing phases and amount of water used for potassium impregnation were targeted using the 11Cu-10K-Al_2O_3 catalyst. Since the separation of the excess H_2 was always required for a syngas product suitable for downstream operation, such as the Fisher-Tropsh process, the best result was obtained using the highest temperature and

H_2 flow rates, in order to improve reduction kinetics. CO_2 capture instead benefited of long contact time. Addition of water enhanced the dispersion of the active metal and the generation of CO_2 capture sites. The bast CCR activity was obtained operating the reaction at 450 °C at ambient pressure with the catalyst synthesised using three times the amount of water recommended in the incipient wetness impregnation method. Reactant streams were constituted by $10\,\mathrm{mL\,min^{-1}}$ of 9.9 vol.% CO_2 in He and $50\,\mathrm{mL\,min^{-1}}$ of pure H_2. 100 s of initial CO_x full capture were achieved, with a selectivity towards CO in the reduction phase above 99% and no methane production.

As a future perspective, further research on the effect of the synthesis method on the dispersion of the active species should be carried out. Moreover, the optimal combination of copper and potassium loading should be investigated. Because of the elusiveness of the catalyst towards common analysis techniques, certain conclusions of the effective reaction mechanism were difficult to obtain. Since in situ and operando studies showed a potentiality, UV-Vis spectroscopic analysis is recommended to possibly complete results obtained with FT-IR and Raman spectroscopies.

Set up limitation did not allow for GHSV modification by varying the catalyst loading in the reactor. In principle, no significant difference should exist. From this point of view, the scale up of a chemical looping system as the one proposed in Chapter 1 seems to be feasible. As a final remark, CCR process could reveal itself suitable as a direct air capture technology, thus becoming a negative carbon emissions solution. In fact, as decreasing the CO_2 flow rate resulted in a longer full capture period, an equivalent result could be obtained decreasing CO_2 concentration.

Bibliography

[1] Jessica Merzdorf. New studies increase confidence in NASA's measure of earth's temperature. Technical report, NASA's Goddard Space Flight Center, 2019. URL `https://www.nasa.gov/feature/goddard/2019/gistemp-warming-trends-greater-than-data-uncertain`. Page Last Updated: May 28, 2019.

[2] U.S. EPA. Inventory of u.s. greenhouse gas emissions and sinks: 1990-2018. Technical report, U.S. Environmental Protection Agency, 2020. URL `https://www.epa.gov/ghgemissions/inventory-us-greenhouse-gas-emissions-and-sinks`. available online.

[3] Dudley B. BP statistical review of world energy. Technical report, BP plc, 2019.

[4] IEA. Data and statistics. Technical report, IEA, 2019. URL `https://www.iea.org/data-and-statistics?country=WORLD&fuel=CO2%20emissions&indicator=CO2%20emissions%20by%20sector`. available online.

[5] IEA. World energy balances: Overview. Technical report, IEA, 2019. URL `https://www.iea.org/reports/world-energy-balances-overview`. available online.

[6] IEA. Global energy review 2019. Technical report, IEA, 2019. URL `https://www.iea.org/reports/global-energy-review-2019`. available online.

[7] Mai Bui, Claire S Adjiman, André Bardow, Edward J Anthony, Andy Boston, Solomon Brown, Paul S Fennell, Sabine Fuss, Amparo Galindo, Leigh A Hackett, et al. Carbon capture and storage (CCS): the way forward. *Energy & Environmental Science*, 11(5):1062–1176, 2018.

[8] S.B. Martynov, N.K. Daud, H. Mahgerefteh, S. Brown, and R.T.J. Porter. Impact of stream impurities on compressor power requirements for CO_2 pipeline transportation. *International Journal of Greenhouse Gas Control*, 54:652–661, 2016.

[9] Stefan Bachu. Review of CO_2 storage efficiency in deep saline aquifers. *International Journal of Greenhouse Gas Control*, 40:188–202, 2015.

[10] Vijay Maddali, Gurudeo Anand Tularam, and Patrick Glynn. Economic and time-sensitive issues surrounding CCS: A policy analysis. *Environmental science & technology*, 49(15):8959–8968, 2015.

[11] Paul Upham and Thomas Roberts. Public perceptions of CCS: emergent themes in pan-european focus groups and implications for communications. *International Journal of Greenhouse Gas Control*, 5(5):1359–1367, 2011.

[12] Claudio Ampelli, Siglinda Perathoner, and Gabriele Centi. CO_2 utilization: an enabling element to move to a resource-and energy-efficient chemical and fuel production. *Philosophical Transactions of the Royal Society A: Mathematical, Physical and Engineering Sciences*, 373(2037):20140177, 2015.

[13] Niklas von der Assen and André Bardow. Life cycle assessment of polyols for polyurethane production using CO_2 as feedstock: insights from an industrial case study. *Green Chemistry*, 16(6):3272–3280, 2014.

[14] Omar Y. Abdelaziz, Wafaa M. Hosny, Mamdouh A. Gadalla, Fatma H. Ashour, Ibrahim A. Ashour, and Christian P. Hulteberg. Novel process technologies for conversion of carbon dioxide from industrial flue gas streams into methanol. *Journal of CO_2 utilization*, 21:52–63, 2017.

[15] Séverine Moret, Paul J Dyson, and Gábor Laurenczy. Direct synthesis of formic acid from carbon dioxide by hydrogenation in acidic media. *Nature communications*, 5:4017, 2014.

[16] Michele Aresta, Angela Dibenedetto, and Eugenio Quaranta. State of the art and perspectives in catalytic processes for CO_2 conversion into chemicals and fuels: The distinctive contribution of chemical catalysis and biotechnology. *Journal of Catalysis*, 343:2–45, 2016.

[17] Yolanda A. Daza and John N. Kuhn. CO_2 conversion by reverse water gas shift catalysis: comparison of catalysts, mechanisms and their consequences for CO_2 conversion to liquid fuels. *RSC advances*, 6(55):49675–49691, 2016.

[18] Arne Kätelhön, Raoul Meys, Sarah Deutz, Sangwon Suh, and André Bardow. Climate change mitigation potential of carbon capture and utilization in the chemical industry. *Proceedings of the National Academy of Sciences*, 116(23):11187–11194, 2019.

[19] Marcello De Falco, Gaetano Iaquaniello, and Gabriele Centi. *CO_2: A valuable source of carbon.* Springer, 2013.

[20] Rakesh Agrawal, Navneet R. Singh, Fabio H. Ribeiro, and W. Nicholas Delgass. Sustainable fuel for the transportation sector. *Proceedings of the National Academy of Sciences*, 104(12):4828–4833, 2007.

[21] André Sternberg, Christian M. Jens, and André Bardow. Life cycle assessment of CO_2-based c1-chemicals. *Green Chemistry*, 19(9):2244–2259, 2017.

[22] Deanna M. D'Alessandro, Berend Smit, and Jeffrey R. Long. Carbon dioxide capture: prospects for new materials. *Angewandte Chemie International Edition*, 49(35):6058–6082, 2010.

[23] IPCC. IPCC special report on carbon dioxide capture and storage. Technical report, IPCC, 2005. URL `https://www.ipcc.ch/site/assets/uploads/2018/03/srccs_wholereport-1.pdf`. available online.

[24] Liang-Shih Fan, Liang Zeng, William Wang, and Siwei Luo. Chemical looping processes for CO_2 capture and carbonaceous fuel conversion–prospect and opportunity. *Energy & Environmental Science*, 5(6):7254–7280, 2012.

[25] Junya Wang, Liang Huang, Ruoyan Yang, Zhang Zhang, Jingwen Wu, Yanshan Gao, Qiang Wang, Dermot O'Hare, and Ziyi Zhong. Recent advances in solid sorbents for CO_2 capture and new development trends. *Energy & Environmental Science*, 7(11):3478–3518, 2014.

[26] Sunho Choi, Jeffrey H. Drese, and Christopher W. Jones. Adsorbent materials for carbon dioxide capture from large anthropogenic point sources. *ChemSusChem*, 2 (9):796–854, 2009.

[27] Lingjun Hu and Atsushi Urakawa. Continuous CO_2 capture and reduction in one process: CO_2 methanation over unpromoted and promoted Ni/ZrO_2. *Journal of CO_2 Utilization*, 25:323–329, 2018.

[28] Luis F. Bobadilla, José M. Riesco-García, Germán Penelás-Pérez, and Atsushi Urakawa. Enabling continuous capture and catalytic conversion of flue gas CO_2 to syngas in one process. *Journal of CO_2 Utilization*, 14:106–111, 2016.

[29] Tsuyoshi Hyakutake, Wouter van Beek, and Atsushi Urakawa. Unravelling the nature, evolution and spatial gradients of active species and active sites in the catalyst bed of unpromoted and K/Ba-promoted Cu/Al_2O_3 during CO_2 capture-reduction. *Journal of Materials Chemistry A*, 4(18):6878–6885, 2016.

[30] Oh-Shim Joo, Kwang-Deog Jung, Il Moon, Alexander Ya Rozovskii, Galina I Lin, Sung-Hwan Han, and Sung-Jin Uhm. Carbon dioxide hydrogenation to form methanol via a reverse-water-gas-shift reaction (the CAMERE process). *Industrial & engineering chemistry research*, 38(5):1808–1812, 1999.

[31] André Sternberg and André Bardow. Life cycle assessment of power-to-gas: syngas vs methane. *ACS Sustainable Chemistry & Engineering*, 4(8):4156–4165, 2016.

[32] Philipp Kaiser, Rajabhau Bajirao Unde, Christoph Kern, and Andreas Jess. Production of liquid hydrocarbons with CO_2 as carbon source based on reverse water-gas shift and fischer-tropsch synthesis. *Chemie Ingenieur Technik*, 85(4):489–499, 2013.

[33] Marcello De Falco, Gaetano Iaquaniello, and Gabriele Centi. *CO_2: A valuable source of carbon.* Springer, 2013.

[34] Yurii S.H. Matros, Grigorii A. Bunimovich, and Vadim O. Strots. Reaction kinetics as a basis for optimal transient operation of catalytic reactors. In *Studies in Surface Science and Catalysis*, volume 109, pages 141–155. Elsevier, 1997.

[35] Tobias Pröll, Philipp Kolbitsch, Johannes Bolhàr-Nordenkampf, and Hermann Hofbauer. A novel dual circulating fluidized bed system for chemical looping processes. *AIChE Journal*, 55(12):3255–3266, 2009.

[36] Robin W. Hughes, Dennis Y. Lu, Edward J. Anthony, and Arturo Macchi. Design, process simulation and construction of an atmospheric dual fluidized bed combustion system for in situ CO_2 capture using high-temperature sorbents. *Fuel Processing Technology*, 86(14-15):1523–1531, 2005.

[37] Yolanda A. Daza, Ryan A. Kent, Matthew M. Yung, and John N. Kuhn. Carbon dioxide conversion by reverse water-gas shift chemical looping on perovskite-type oxides. *Industrial & Engineering Chemistry Research*, 53(14):5828–5837, 2014.

[38] Yolanda A. Daza, Debtanu Maiti, Ryan A. Kent, Venkat R. Bhethanabotla, and John N. Kuhn. Isothermal reverse water gas shift chemical looping on $La_{0.75}Sr_{0.25}Co_{(1-Y)}Fe_YO_3$ perovskite-type oxides. *Catalysis Today*, 258:691–698, 2015.

[39] Xiaodong Li, Shumin Wang, Li Li, Yongfu Sun, and Yi Xie. Progress and perspective for in situ studies of CO_2 reduction. *Journal of the American Chemical Society*, 2020.

[40] Shin-Ichiro Fujita, Masahito Usui, and Nobutsune Takezawa. Mechanism of the reverse water gas shift reaction over Cu/ZnO catalyst. *Journal of Catalysis*, 134 (1):220–225, 1992.

[41] José A Rodriguez, Jaime Evans, Leticia Feria, Alba B. Vidal, Ping Liu, Kenichi Nakamura, and Francesc Illas. CO_2 hydrogenation on Au/Tic, Cu/tic, and Ni/Tic catalysts: Production of CO, methanol, and methane. *Journal of catalysis*, 307: 162–169, 2013.

[42] Damjan Lašič Jurković, Andrej Pohar, Venkata D.B.C. Dasireddy, and Blaž Likozar. Effect of copper-based catalyst support on reverse water-gas shift reaction (RWGS) activity for CO_2 reduction. *Chemical Engineering & Technology*, 40(5):973–980, 2017.

[43] Lingzhi Zhang, Jean-Marc M. Millet, and Umit S. Ozkan. Effect of Cu loading on the catalytic performance of Fe–Al–Cu for water-gas shift reaction. *Applied Catalysis A: General*, 357(1):66–72, 2009.

[44] Clare Anderson, Trent Harkin, Minh Ho, Kathryn Mumford, Abdul Qader, Geoff Stevens, and Barry Hooper. Developments in the CO2CRC UNO MK 3 process: A multi-component solvent process for large scale CO_2 capture. *Energy Procedia*, 37:225–232, 2013.

[45] Janna V. Veselovskaya, Vladimir S. Derevschikov, Tatyana Yu Kardash, Olga A. Stonkus, Tatiana A. Trubitsina, and Aleksey G. Okunev. Direct CO_2 capture from ambient air using K_2CO_3/Al_2O_3 composite sorbent. *International Journal of Greenhouse Gas Control*, 17:332–340, 2013.

[46] Ching-Shiun Chen, Wu-Hsun Cheng, and Shou-Shiun Lin. Study of reverse water gas shift reaction by TPD, TPR and CO_2 hydrogenation over potassium-promoted Cu/SiO_2 catalyst. *Applied Catalysis A: General*, 238(1):55–67, 2003.

[47] Jung Moo Lee, Yoon Jae Min, Ki Bong Lee, Sang Goo Jeon, Jeong Geol Na, and Ho Jung Ryu. Enhancement of CO_2 sorption uptake on hydrotalcite by impregnation with K_2CO_3. *Langmuir*, 26(24):18788–18797, 2010.

[48] Binglian Liang, Hongmin Duan, Xiong Su, Xiaodong Chen, Yanqiang Huang, Xiaowei Chen, Juan José Delgado, and Tao Zhang. Promoting role of potassium in the reverse water gas shift reaction on Pt/mullite catalyst. *Catalysis Today*, 281:319–326, 2017.

[49] Xiaoli Yang et al. Promotion effects of potassium on the activity and selectivity of Pt/zeolite catalysts for reverse water gas shift reaction. *Applied Catalysis B: Environmental*, 216:95–105, 2017.

[50] J.A. Loiland et al. $Fe/\gamma-Al_2O_3$ and $Fe–K/\gamma\text{-}Al_2O_3$ as reverse water-gas shift catalysts. *Catalysis Science & Technology*, 6:5267–5279, 2016.

[51] Francesco Pinna. Supported metal catalysts preparation. *Catalysis Today*, 41 (1-3):129–137, 1998.

[52] Peter Munnik, Petra E. de Jongh, and Krijn P. de Jong. Recent developments in the synthesis of supported catalysts. *Chemical reviews*, 115(14):6687–6718, 2015.

[53] Chang Hsin-Fu, Saleque Mohammed Abu, Hsu Wen-Su, and Lin Wen-Hsiung. Effect of acidity and copper surface area of the Cu/Al_2O_3 catalyst prepared by electroless plating procedure on dehydrogenation reactions. *Journal of molecular catalysis*, 94(2):233–242, 1994.

[54] M. Kurtz, H. Wilmer, T. Genger, O. Hinrichsen, and M. Muhler. Deactivation of supported copper catalysts for methanol synthesis. *catalysis Letters*, 86(1-3): 77–80, 2003.

[55] Atul Bansode, Bruno Tidona, Philipp Rudolf von Rohr, and Atsushi Urakawa. Impact of K and Ba promoters on CO_2 hydrogenation over Cu/Al_2O_3 catalysts at high pressure. *Catalysis Science & Technology*, 3(3):767–778, 2013.

[56] Jinyong Luo, Feng Gao, Do Heui Kim, and Charles H.F. Peden. Effects of potassium loading and thermal aging on K/Pt/Al_2O_3 high-temperature lean NO_x trap catalysts. *Catalysis Today*, 231:164–172, 2014.

[57] J.C. Slaa, G.J.M. Weierink, J.G. Van Ommen, and J.R.H. Ross. TPR and infrared measurements with Cu/ZnO/Al_2O_3 based catalysts for the synthesis of methanol and higher alcohols from CO + H_2. *Catalysis today*, 12(4):481–490, 1992.

[58] D. Courcot, C. Pruvost, E.A. Zhilinskaya, and A. Aboukaïs. Potential of supported copper and potassium oxide catalysts in the combustion of carbonaceous particles. *Kinetics and catalysis*, 45(4):580–588, 2004.

[59] Komandur V.R. Chary, Kottapalli Kalyana Seela, Dhachapally Naresh, and Pagadala Ramakanth. Characterization and reductive amination of cyclohexanol and cyclohexanone over Cu/ZrO_2 catalysts. *Catalysis Communications*, 9(1):75–81, 2008.

[60] Harold H Kung. *Transition metal oxides: surface chemistry and catalysis*. Elsevier, 1989.

[61] Erwin Lam, Juan José Corral-Pérez, Kim Larmier, Gina Noh, Patrick Wolf, Aleix Comas-Vives, Atsushi Urakawa, and Christophe Copéret. CO_2 hydrogenation on

Cu/Al_2O_3: Role of the metal/support interface in driving activity and selectivity of a bifunctional catalyst. *Angewandte Chemie*, 131(39):14127–14134, 2019.

[62] Andrea Álvarez, Marta Borges, Juan José Corral-Pérez, Joan Giner Olcina, Lingjun Hu, Damien Cornu, Rui Huang, Dragos Stoian, and Atsushi Urakawa. CO_2 activation over catalytic surfaces. *ChemPhysChem*, 18(22):3135–3141, 2017.

[63] J. Nakamura, I. Nakamura, T. Uchijima, Y. Kanai, T. Watanabe, M. Saito, and T. Fujitani. Methanol synthesis over a Zn-deposited copper model catalyst. *Catalysis letters*, 31(4):325–331, 1995.

[64] Ching-Shiun Chen and Wu-Hsun Cheng. Study on the mechanism of co formation in reverse water gas shift reaction over Cu/SiO_2 catalyst by pulse reaction, TPD and TPR. *Catalysis letters*, 83(3-4):121–126, 2002.

[65] Charles T. Campbell and Karl-Heinz Ernst. Forward and reverse water-gas shift reactions on model copper catalysts: Kinetics and elementary steps. ACS Publications, 1992.

[66] M. Kadleıková, J. Breza, and M. Veselỳ. Raman spectra of synthetic sapphire. *Microelectronics Journal*, 32(12):955–958, 2001.

[67] J.F. Xu, W. Ji, Z.X. Shen, W.S. Li, S.H. Tang, X.R. Ye, D.Z. Jia, and X.Q. Xin. Raman spectra of cuo nanocrystals. *Journal of Raman spectroscopy*, 30(5): 413–415, 1999.

[68] Lung-Chieh Chen, Cheng-Chiang Chen, Kai-Chieh Liang, Sheng Hsiung Chang, Zhong-Liang Tseng, Shih-Chieh Yeh, Chin-Ti Chen, Wen-Ti Wu, and Chun-Guey Wu. Nano-structured CuO-Cu_2O complex thin film for application in $CH_3NH_3PbI_3$ perovskite solar cells. *Nanoscale research letters*, 11(1):402, 2016.